

**AREA OF REVIEW AND CORRECTIVE ACTION PLAN
40 CFR 146.84(b)**

Pelican Sequestration Project

1.0 Facility Information.....	2
2.0 Computational Modeling Approach.....	2
2.1 Model background	2
2.2 Site geology and hydrology	4
2.3 Model domain	28
2.4 Porosity and permeability	40
2.5 Constitutive relationships and other rock properties.....	51
2.6 Boundary conditions	52
2.7 Initial conditions	53
2.8 Operational information.....	55
2.9 Fracture pressure and fracture gradient.....	56
3.0 Computational Modeling Results	63
3.1 Predictions of system behavior	63
3.2 Model calibration and validation	65
4.0 Area of Review (AOR).....	72
4.1 Critical pressure calculations	72
4.2 AOR delineation	73
4.3 Fault leakage assessment	76
5.0 Corrective Action	77
5.1 Tabulation of wells within the AOR	77
5.2 Plan for site access	79
5.3 Corrective action evaluation	79
5.4 Corrective action procedure	81
6.0 Re-Evaluation Schedule and Criteria	83
6.1 AOR re-evaluation cycle.....	83
6.2 Triggers for AOR re-evaluations prior to the next scheduled re-evaluation.....	84
7.0 References.....	85
Appendix A: Near Wells Near the Project Area	90
Appendix B: Table of Wells	92
Appendix C: Site-Specific Data and Procedures.....	94
C.1 Sidewall core sampling and analysis.....	94
C.2 Formation fluid sampling and analysis.....	94
C.3 Well testing and analysis.....	95
Appendix D: Risk-Based AOR	99
D1. Introduction.....	99
D2. Simulation results.....	100
D3. References	108
Appendix E: Historical Seismicity Data.....	110

1.0 Facility Information

Facility name: Pelican Sequestration Project
Pelican CCS 1 Well

Facility contact: [REDACTED], Project Manager
5 Greenway Plaza Houston, TX 77046
[REDACTED]

Well location: Holden, Livingston Parish, Louisiana
[REDACTED] (NAD 1927, BLM Zone 15N)

2.0 Computational Modeling Approach

This plan discusses Area of Review (AOR) delineation and provides corrective actions needed in the wells that penetrate the upper confining zone within the AOR. Delineation of the AOR is one of the key elements in the Class VI Rule to ensure underground sources of drinking water (USDWs) in the region surrounding the geologic sequestration project are not endangered by the injection activity.

The AOR is determined using a multiphase CO₂-brine transport model, which is constructed from a sophisticated geologic model that accounts for site-specific hydrogeology. The methods and approaches for developing this complex multiphase simulation model and delineating the AOR are defined below.

Control of the pore space into which the free-phase CO₂ plume is predicted to migrate, is a requirement for a Class VI permit. In Louisiana, the pore space is owned by the surface owner of the land. An agreement has been made with the landowners regarding pore space ownership in the Pelican Sequestration Project.

2.1 Model background

2.1.1 Model name and authors/institution

The model is the GEM (v2021.10) reservoir simulator with the Greenhouse Gas (GHG) module from Computer Modeling Group Ltd.

2.1.2 Description of model

GEM is a commercially available, compositional, and finite-difference simulator that is commonly used to model hydrocarbon production, enhanced oil recovery, and other thermodynamic and fluid flow reservoir processes. GEM has also been used to model several carbon capture and storage projects. The Greenhouse Gas (GHG) module accounts for the thermodynamic interactions between three phases: a H₂O-rich phase (liquid), CO₂-rich phase (gas), and a solid phase, which may include several minerals. Physical properties (e.g., density, viscosity, and enthalpy) of the H₂O and CO₂ phases and CO₂ solubility in H₂O are calculated from a correlation suitable for a wide range of typical storage reservoir conditions, including temperature ranges between 12°C and

150°C and pressures up to 110 MPa. Details of this method can be found in Collins et al. (1992), Thomas and Thurnau (1983), and Nghiem and Li (1989).

Additional assumptions governing the phase interactions throughout the simulations are as follows:

- The CO₂-rich phase (gas) density is obtained using the Peng-Robinson equation of state. The model was accurately tuned and modified as described below (Peng and Robinson, 1976).
- The CO₂ dissolution in brine is calculated from Henry's Law Constant Correlation using Harvey's method (Harvey, 1996).
- The brine density is specified at a reference pressure of [REDACTED] psi and corrected for local pressure variations using a specified water compressibility. It is then corrected for the dissolved CO₂ and ionic components using their partial molar volumes. The brine viscosity is calculated using the Kestin (1981) correlation.
- Chemical equilibria among [REDACTED] provided in the CMG GHG module. The solid phase includes [REDACTED] minerals. Reactions among these minerals and ions are modeled using the chemical reactions and reaction coefficients from a Lawrence Livermore National Laboratory database (Thibeau, 2007), which were also used in a simulation study by Nghiem et al. (2004).
- The CO₂ gas viscosity is calculated per the methods described by Pedersen et al. (1984).
- The gas density is obtained by using a cubic equation of state developed by Peng and Robinson (1976) described by Equation 1:

$$P = \frac{RT}{(v - b_{mix})} - \frac{a_{mix}}{(v^2 + 2vb_{mix} - b_{mix}^2)} \dots\dots\dots \text{(Equation 1)}$$

Where:

v is the molar volume;

P is the pressure;

T is the temperature in Kelvin;

R is the universal gas constant;

a_{mix} and b_{mix} are mixture-specific functions of temperature and composition, calculated from the critical properties and acentric factors of the components.

The CMG WinProp software has a built-in library for the properties of CO₂ and CH₄, based on Reid et al. (1977). No changes were made to the library components.

The transition between liquid and gaseous CO₂ can lead to rapid density changes in the gas phase. The simulator uses a [REDACTED] between the liquid and gaseous density to represent the two-phase CO₂ region.

The CO₂ delivery temperature to the injection well is estimated to be between 60°F and 120°F. Therefore, the temperature of the injectant will be comparable to the reservoir formation temperature at the injection interval. [REDACTED]

With respect to the time step selection, the software algorithm optimizes the time step duration based on the specific convergence criteria designed to minimize numerical artifacts. For these simulations, the time step size ranged from [REDACTED] days. In all cases, the maximum solution change over a time step is monitored and compared with the specified target. Convergence is achieved once the model reaches the maximum tolerance where small changes of the temperature and pressure calculation results occur on successive iterations. New time steps are chosen so that the predicted solution change is less than a specified target.

Chemical equilibria of ionic species in brine and reactions of minerals with ions were simulated in only limited cases due to their long computing times. Results suggested negligible net carbon capture by minerals during the CO₂ injection period. After CO₂ injection has ceased, however, continued precipitation of calcite, dolomite, and other minerals over an extended period (100+ years) may indeed play a key role in retaining a large fraction of carbon atoms permanently in the reservoir.

2.2 Site geology and hydrology

The Pelican CO₂ Sequestration Hub (the Pelican Hub) encompasses [REDACTED] acres of deep saline aquifers for CO₂ storage in Livingston and St. Helena Parishes, LA (Figure AOR-1). The Pelican Hub is 20 miles east of Baton Rouge, LA, and is optimally located near many potential CO₂ source facilities along the Mississippi River Industrial Corridor.

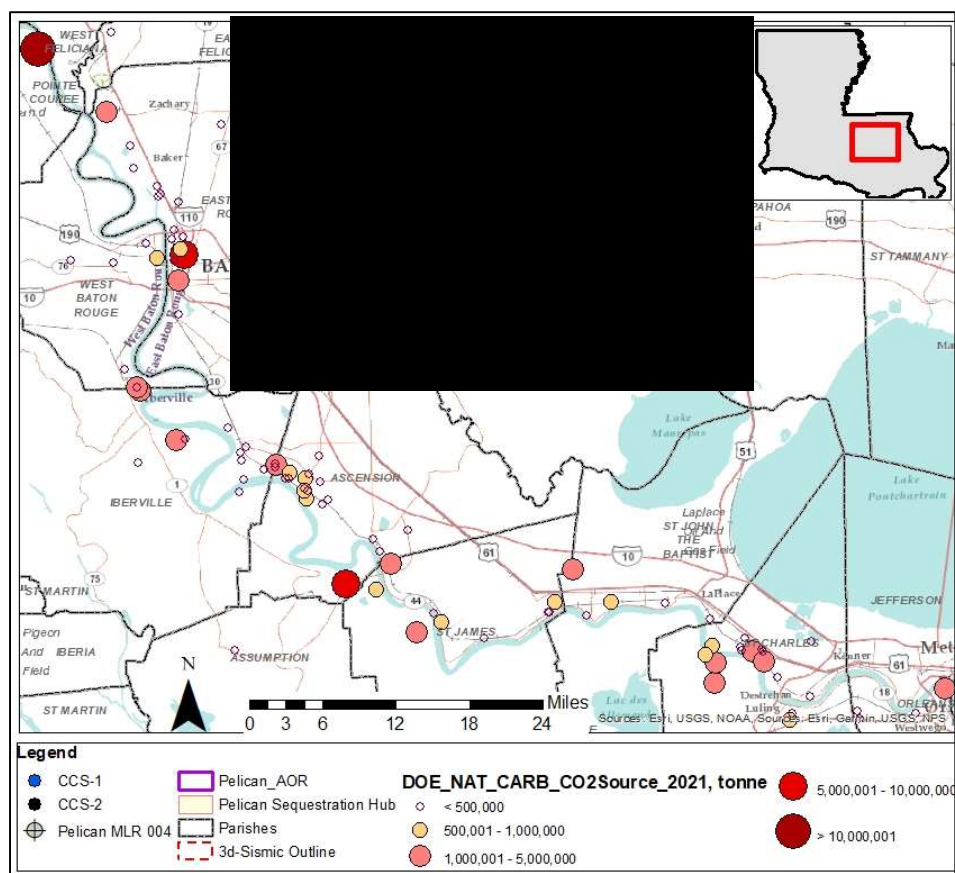


Figure AOR-1—Pelican Sequestration Hub location with respect to DOE-identified carbon emitters (<https://netl.doe.gov/carbon-management/carbon-storage/atlas-data>) along the Mississippi River Chemical Corridor

2.2.1 Physical geography

The Pelican Sequestration Hub lies mostly within Livingston Parish, Louisiana. The area of investigation (AOI) straddles the parish line between Livingston and St. Helena Parishes. The surface geology is of Quaternary-aged alluvium and terrace deposits, and The Hub lies within forested acreage (Figure AOR-2). The AOI lies in the Tickfaw River sub-basin (Figure AOR-3). The main drainage systems are the Tickfaw River and tributaries of the Hog Branch. Surface elevation in the area is between 150 and 40 ft above sea level, with a gentle dip of 0.09° toward the Gulf of Mexico. Along the southern boundary of the AOI is the Denham Springs-Scotland Ville Fault.

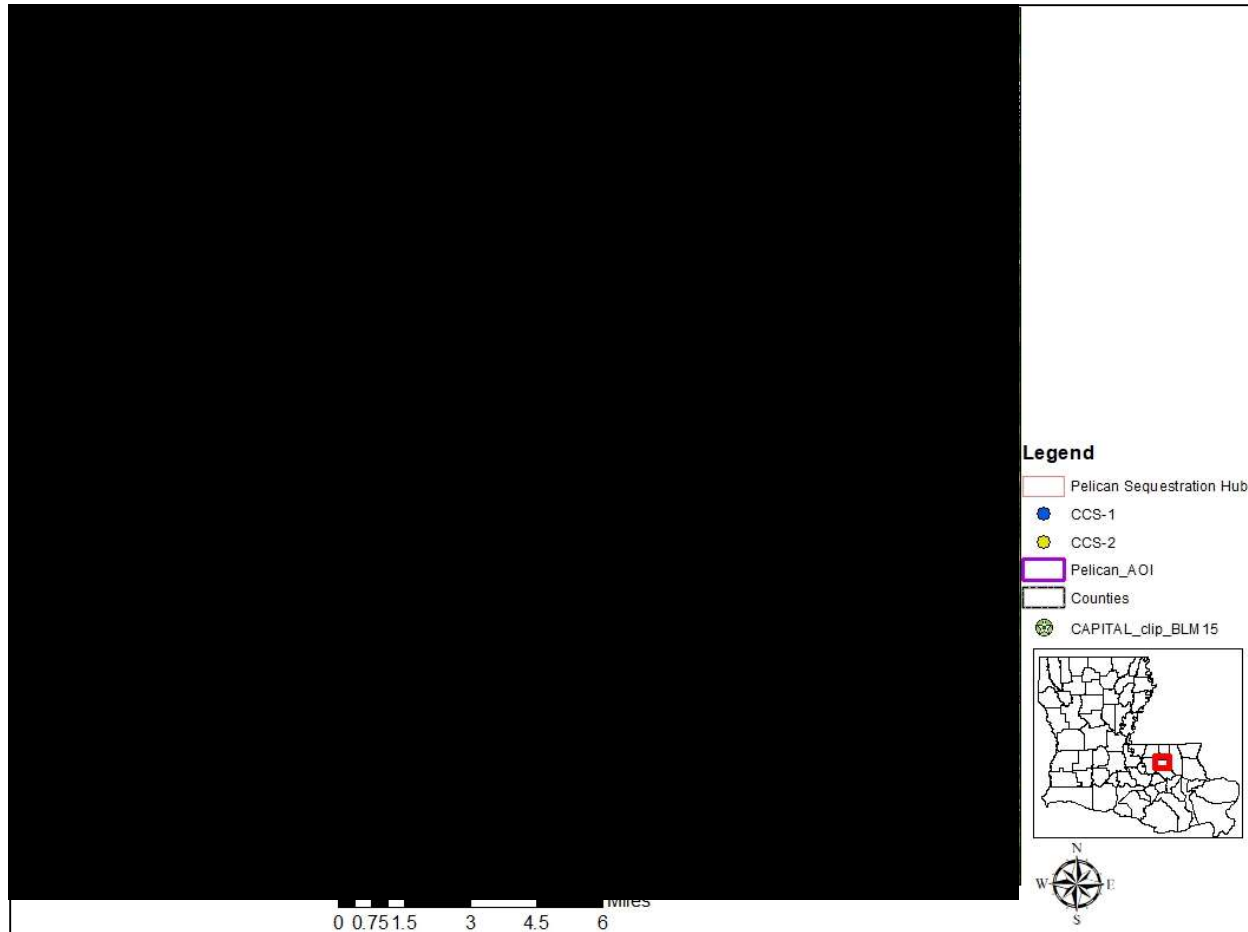


Figure AOR-2—Satellite imagery highlighting the project area. The Pelican Sequestration Hub lies within forested acreage (green patchwork). Populated areas near the AOI include Denham Springs (west and southwest), Livingston and Holden (south), and Hammond (southeast and east). Imagery from ESRI.



Figure AOR-3—LIDAR imagery highlighting surface topography, main river drainage, and surface-penetrating faults. Imagery from <https://maps.ga.lsu.edu/lidar2000>.

2.2.2 Regional geology

The storage complex for the Pelican Hub targets approximately [REDACTED] strata (Figure AOR-4) in the Northern Gulf of Mexico basin. The Pelican Hub project plans to use the [REDACTED] formation as the storage complex for sequestration wells CCS 1 and CCS 2. The upper confining units have been identified as the shale and carbonate beds of the upper [REDACTED]. Below the confining units are the identified injection zones, which are coastal plain and delta sands in the lower part of the [REDACTED] formation. The basal seal is the thick shale of the [REDACTED].

Above the [REDACTED] upper confining unit [REDACTED] present strata. [REDACTED]
[REDACTED]
[REDACTED] The deepest freshwater aquifers identified in the area are Jasper-equivalent aquifers (White, 2016). These aquifers are separated from saline aquifers by an unnamed confining clay unit.

Series	Clastic Input	Stage	Aquifer System or Confining Unit	Project Storage Definitions
Pleistocene			Chicot equivalent aquifer system	
Pliocene		L	Evangeline equivalent aquifer system	
		E	Unnamed Confining Unit	
Miocene		L	Jasper equivalent aquifer sands	
		M	Unnamed Confining Unit	
		E	Fleming Formation Regional Start of Saline Aquifer	
Oligocene		L	Anahuac Formation	
		E	Frio Formation	
			Vicksburg Formation	

Figure AOR-4—Geological stratigraphic chart showing the project’s storage complex.

Structural history in the AOI during the [REDACTED] to present is dominated by passive margin growth faults accommodating large amounts of prograding sediments. These fault systems are located south and downdip of the Pelican Hub. The two phases of growth faulting identified in the area are [REDACTED] and [REDACTED] to present in age. The [REDACTED] Fault Zone was active during early [REDACTED] (McCulloh et al., 2012) and it penetrates the [REDACTED] sand, but not the [REDACTED] seal (Figure AOR-5).



Figure AOR-5—Structural cross section generated from Oxy-licensed 3D seismic data shows that faulting south of the acreage has little interaction with the Pelican Hub acreage. Reference Figure AOR-1 for cross section A–A’ location.

2.2.3 Stratigraphy

Paleozoic and Mesozoic

Understanding the pre-Triassic basement rim around the Gulf of Mexico provides provenance understanding for lithologic distribution in the Pelican Hub [REDACTED] storage complex. These rocks outcrop in the Appalachian and Ouachita Mountain belts northeast and north of the Northern Gulf of Mexico basin. Predominant rock types in the Appalachian province are igneous (granite), metamorphic (marble and schist), and clastic rock (Devonian carbonates, Mississippi limestone, and Pennsylvanian coal). Rock types in the Ouachita Mountain belt are predominantly dark carbonates, black shales, cherts, and “flysch” (thinly bedded sandstone and shale) (Salvador, 1991).

The Northern Gulf of Mexico basin has over 30,000 ft of sediment between the surface and basement (Adams, 1997). The oldest sediments are Triassic-aged sandstone and conglomerates that exist locally in rift basins. The Jurassic Louann salt sits unconformably over this unit, where it exists, or over Paleozoic basement (Figure AOR-6). The Louann salt resulted from the evaporation of very large, shallow, and hypersaline water bodies that periodically received water from nearby marine sources. The thickness and geographic extent of the deposit suggest long, gradual subsidence of the Gulf basin. Understanding the presence of the Louann salt and the resulting structures is key to understanding the geology of the Gulf of Mexico basin. For example, it is the Louann salt that creates salt structures and related faults, acts as the deepest slip surface for passive growth faults and keeps basin temperatures suppressed.

During the rest of the Jurassic period, the Gulf experienced a long marine transgression as subsidence continued. In the northern Gulf of Mexico, nonmarine nearshore and eolian sands of the Norphlet formation were conformably deposited over the Louann salt. Above this, the marine Smackover carbonate shale was deposited in restricted basins with equivalent updip oolitic sands. The marine environment continued at the end of the Jurassic with the deposition of the Haynesville shale in a shallower marine setting. The close of the Jurassic was marked by the dark marine, fossiliferous Bossier shale, which grades north into the coarse sands of the Cotton Valley formation.

The Early Cretaceous in the Northern Gulf of Mexico basin consists predominantly of carbonates with times of coarse-grained terrigenous clastics being shed from the continental interior Appalachian and Ouachita Mountains. These sediments were being deposited as subsidence in the basin continued. The Hosston unconformably overlies the Cotton Valley formation; it is a fine-to-coarse sandstone that interfingers and is overlain downdip by the argillaceous and fossiliferous limestones of the Sligo formation, which becomes a more massive, shallow-water, shelfal limestone. Overlying the Sligo are shales and thin limes of the Pearsall formation, which grades into terrigenous clastics updip. This unit again is overlain by a series of shelf carbonates (Glen Rose, Fredericksburg, Washita, and Edwards-Stuart City formations) that grade basinward into deep marine calcareous shales (Atascocita formation). A prominent carbonate shelf margin was established at the end of the Early Cretaceous.

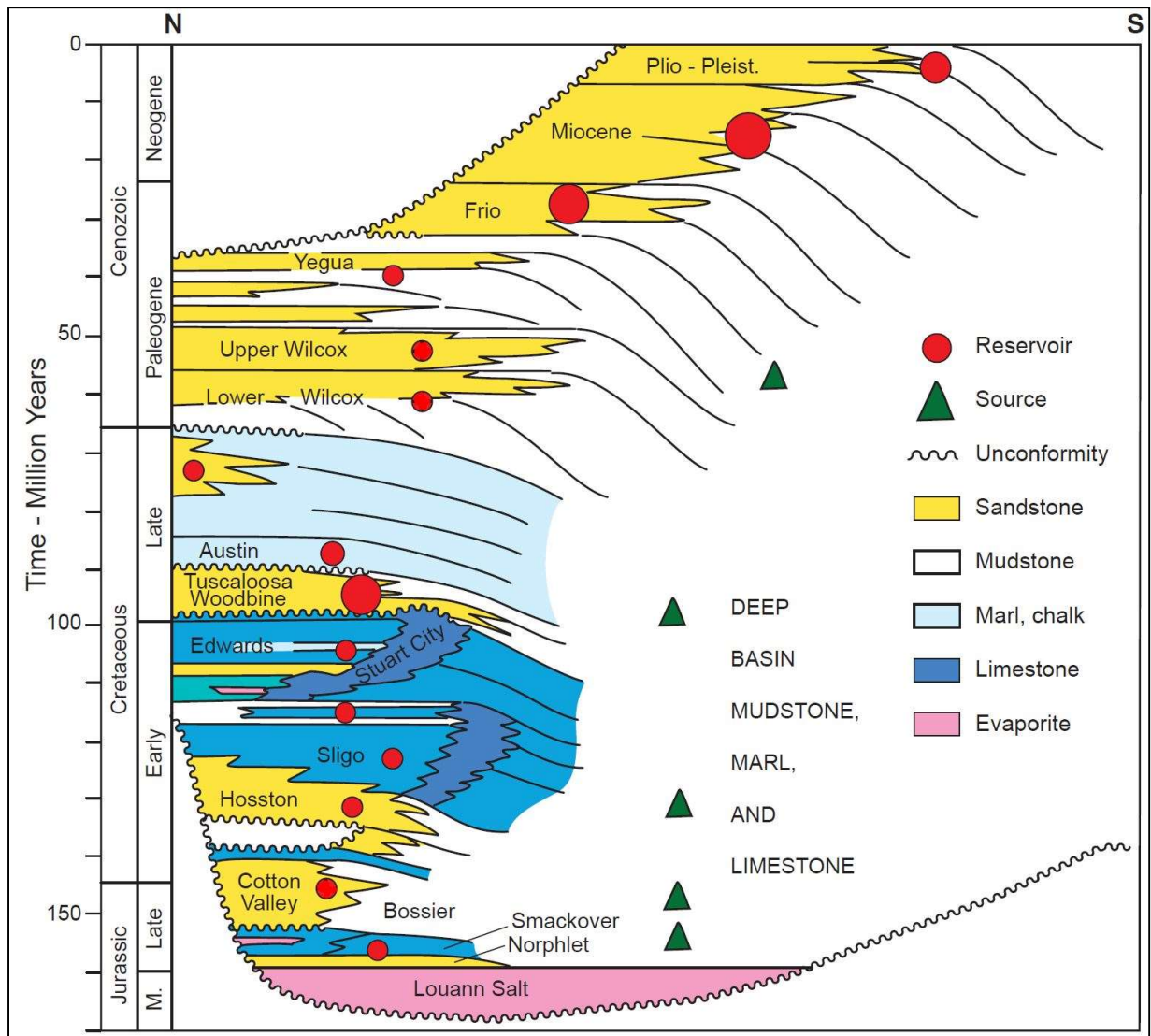


Figure AOR-6—Schematic stratigraphic succession of the Northern Gulf of Mexico (from Galloway, 2009)

The Late Cretaceous was a time of oceanic highstand. Before the onset of the highstand, the terrigenous Tuscaloosa formation prograded basinward. It is divided into three intervals: the Lower Tuscaloosa, Middle Tuscaloosa Shale, and the Upper Tuscaloosa. The Lower Tuscaloosa progrades to the shelf margin as sands were deposited in the basin through submarine channels. The Middle Tuscaloosa is a fossiliferous shale with interbedded calcareous sand that flooded the shelf and thickened downdip on the Early Cretaceous shelf margin. The Upper Tuscaloosa is medium to coarse grained and exists as an expanded section downdip of the Early Cretaceous shelf margin. The Tuscaloosa is the deepest formation penetrated (approximately 20,000 ft) in the area being investigated. After the deposition of the Tuscaloosa, ocean waters flooded the continental USA depositing a series of carbonate mud and chalk layers in the Northern Gulf of Mexico (Austin Chalk, Taylor, and Navarro Groups). The position of the Cretaceous shelf and platform greatly influenced the shape, size, rock type, and amount of Cenozoic sediments deposited in the Gulf basin.

Cenozoic to Present

Cenozoic sedimentation was dominated by prograding terrigenous clastics shed from the Laramide orogeny in the western USA. The Midway formation is the first Paleocene rock to be deposited. It is a transgressive marine shale deposited before the major clastic progradation began. Overlying the Midway is the prograding wedge of the Paleocene to Eocene Wilcox formation. This formation is composed of coarse clastics that entered the basin through feeder systems in northeastern Louisiana and western Mississippi. The Middle and Upper Eocene is defined by a series of transgressive and regressive prograding events resulting in four thick prograding sand-rich wedges, each overlain by thin transgressive shaly marine deposits. The collection of this cyclicity is called the Claiborne Group, which conformably overlies the Wilcox formation. The final formation deposited before the Oligocene Storage Complex is the Jackson formation, which is a deepwater shale in the area of investigation.

[REDACTED]. The outer shelf Vicksburg shale was conformably deposited on the Jackson formation and is the basal seal. Above this are the clastics of the [REDACTED]. In this location, the environment of deposition (EOD) of the storage units are sands deposited and reworked in a retrogradational shore zone to carbonate shelf environment (Figure AOR-7 Galloway, 2000). The sediments deposited during this time are the Frio sands and shales with minimal carbonate input and carbonate-dominated sediments with reworked sands and shales during the Anahuac maximum flooding event. The sands of the Frio formation represent coastal plain and delta sediments deposited as the Central Mississippi River prograded over the muddy Vicksburg shelf (Figure AOR-7a). The Frio depositional system was transgressed upon by the Anahuac Heterostegina Limestone (HET Lime) carbonate platform, resulting in the shrinkage of the Central Mississippi River delta and longshore reworking of platform delta sands by a wave-dominated shore-zone system (Figure AOR-7b). The end of the Oligocene time is marked by a regional maximum flooding event, which resulted in the deposition of the Anahuac shale. [REDACTED]

[REDACTED]

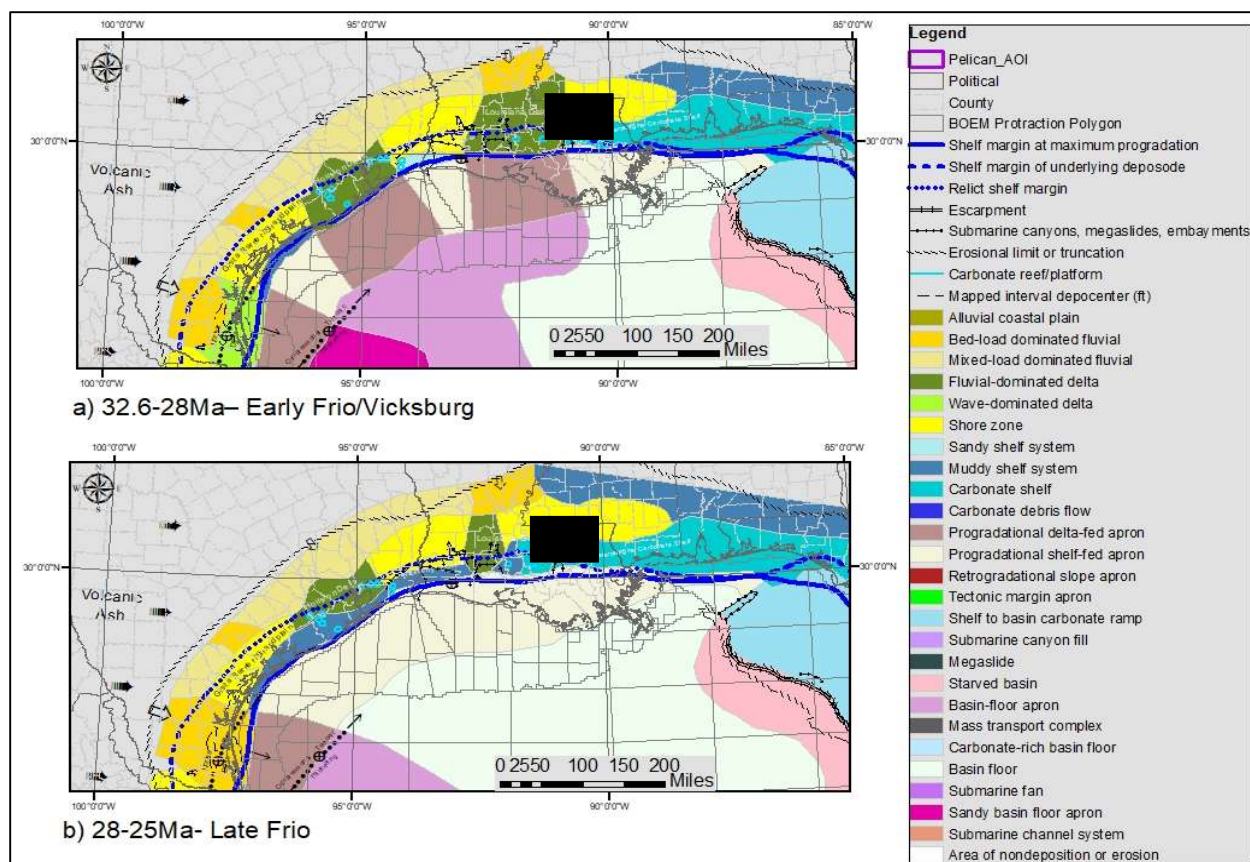


Figure AOR-7—Paleogeography of the Oligocene Frio: a) Early Oligocene, b) Late Oligocene. Maps showing depositional system, sediment dispersal axes, generalized depocenters, and selected depositional and erosional features (Galloway, 2000). AOI is identified by the purple polygon.

During that time, sedimentation into the Gulf basin shifted from the western Gulf of Mexico (Rio Grande Valley) to the northern Gulf of Mexico along the Calcasieu and Central Mississippi River delta systems (Figure AOR-8a, Galloway, 2000). Clastics in these delta systems were fed by rivers draining the Appalachian and basin and range provenances of the USA. Adjacent to and between these delta systems were wave-dominated shore-zone systems, where large volumes of sand and shales were deposited.

Sedimentation during the Middle and Upper Miocene was dominated by sands and shales of a mixed-load fluvial system of the Central Mississippi River (Figure AOR-8b, Galloway, 2002). The extreme amount of sedimentation delivered by this fluvial system was accompanied by a delta-front “collapse margin,” resulting in slump scars, growth faults, and submarine canyons. The end of the Miocene is marked by a second maximum flooding event, which deposited a regionally extensive, clay-rich mudstone that acts as the lower confining unit of the USDW aquifers system.

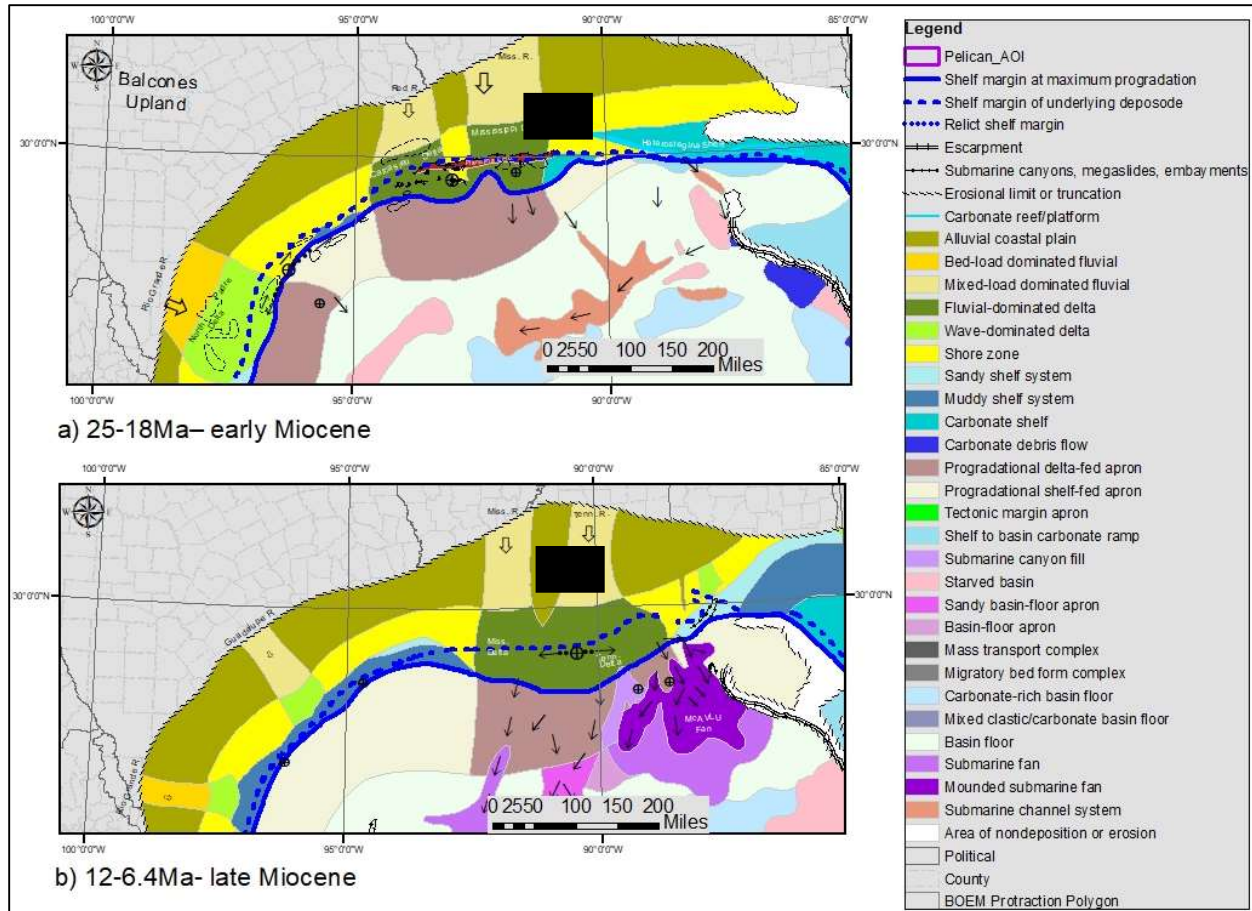


Figure AOR-8—Paleogeography of the Miocene: a) Early Miocene, b) Late Miocene. Maps show depositional system, sediment dispersal axes, generalized depocenters, and selected depositional and erosional features (modified from Galloway, 2000). Miocene sediments are dominated by shore-zone and mixed-load dominated fluvial sediments. AOI is identified by a purple polygon.

Overlying the Upper Miocene confining clay unit are Mississippi River fluvial sediments of the Baton Rouge aquifer systems. These sands have complex geometries representing channel fill, floodplain, levee, and crevasse splay facies (Chamberlain, 2012). The USGS identifies these sands as an amalgamated zone of sand bodies with a high degree of connectivity, causing them to behave like one hydraulic unit.

2.2.5 Basin history and structure

Paleozoic and Mesozoic

The Gulf of Mexico (GOM) is an ocean basin that exists between the southern coast of the USA and the Yucatan Peninsula, Mexico. During the Mesozoic, the Gulf basin underwent three phases of rift tectonics (pre-rift, syn-rift, and post-rift), followed by local rearrangement of basement features.

The pre-rift phase began after the continental plate collision that uplifted the Ouachita Mountains (360-310 mya). During pre-rifting, mantle plumes caused doming of the crust and basin carbonates

were deposited (Paleozoic, 310-250 mya). The continued doming stretched the crust and initiated the syn-rift phase in the late Triassic (225-200 mya).

Syn-rift tectonics are recorded in the Mississippi and North Louisiana Salt Basins and along the southern flanks of the Ouachita Mountains (Figure AOR-9). Rocks deposited during this phase are the redbeds of the Eagle Mills formation. Crustal attenuation continued in the Middle Jurassic (180-160 mya). At this time, the Louann Salt began to be deposited with the evaporation of seawater incurring into the region from the Pacific basin.

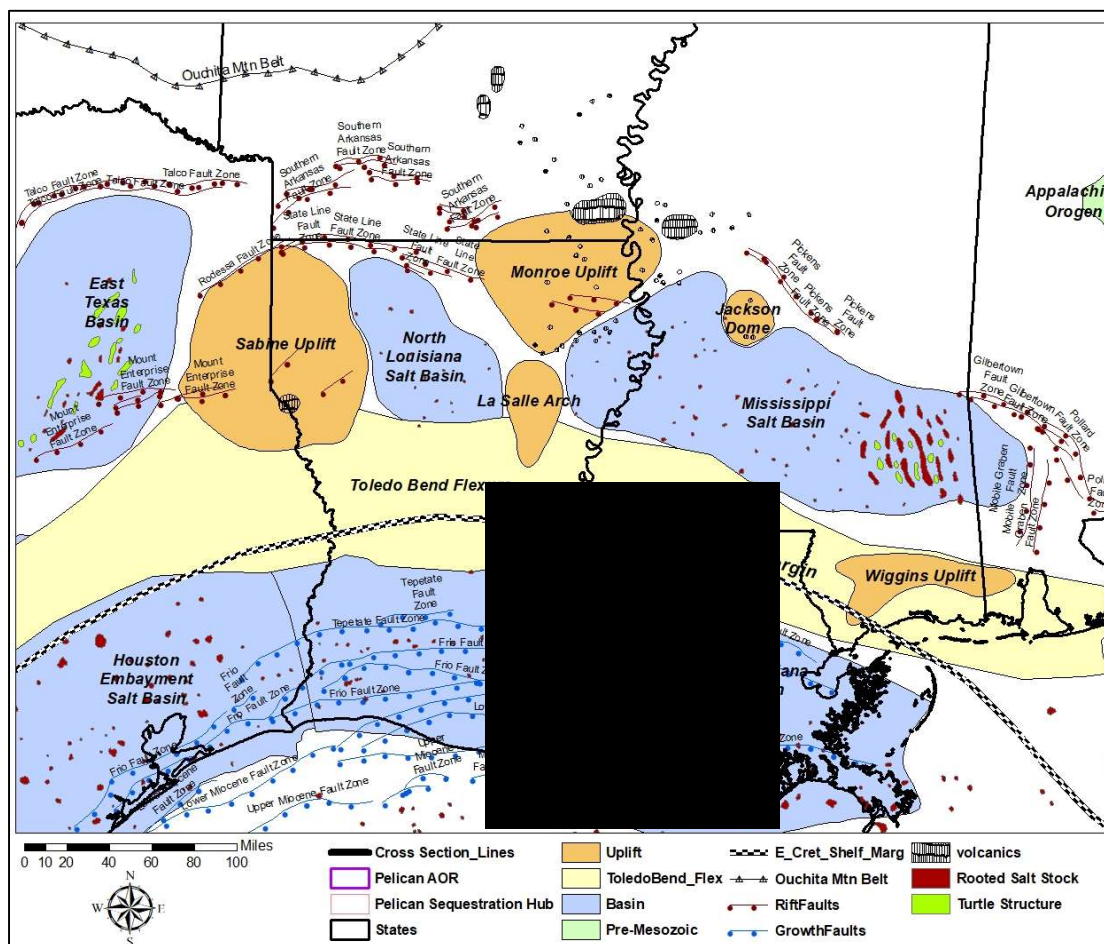


Figure AOR-9—Structural element map showing key structural features that developed during the Mesozoic and Cenozoic periods in the Gulf of Mexico (Pitman, 2010).

Post-rift, passive margin sedimentation began in the northern GOM with the onset of seafloor spreading in the central Gulf of Mexico in the Late Jurassic (155-130 mya). During that time, the basin filled with a series of progradational (Norphlet and Cotton Valley) and retrogradational (Smackover, Haynesville) sequences. Central GOM seafloor spreading ceased during the Early Cretaceous (130-110 mya). This initiated basin subsidence and a stable shelf with a dip toward the south-southeast. The Early Cretaceous sediment sequence is of a prograding continental sediment wedge (Hosston formation) that became flooded by a carbonate platform, which set up a prominent and long-lived shelf margin (Figure AOR-9; Sligo, Glen Rose, and Edward formations).

The Middle Cretaceous (about 100 mya) marked the onset of igneous activity, corresponding to the Cordilleran thrust event, and a time of global sea-level fall. In the northern Gulf, basement highs were uplifted (Figure AOR-9, Sabine and Monroe Uplifts, Jackson Dome, and Wiggins Arch), small salt basins became isolated (N. Louisiana, Mississippi, and S. Louisiana Salt Basins), and the Cretaceous platform margin was exposed, creating a basinwide angular unconformity. The second major flooding event happened through the Late Cretaceous (96-86 mya), when the Tuscaloosa formation prograded over the Early Cretaceous shelf margin. At that time, the first series of down-to-the-basin normal faults developed to accommodate high sedimentation (Tuscaloosa Fault Zone, Figure AOR-9). As the sea level rose, the northern Gulf became flooded by another carbonate shelf (Austin Chalk, Taylor, and Navarro Groups). The end of the Cretaceous and start of the Cenozoic is defined by an unconformity that is associated with the Chicxulub meteor impact (Snedden and Galloway, 2019). The impact zone is about [REDACTED] miles south of the Pelican Sequestration Hub along the northern coast of the Yucatan Peninsula. It is believed to have caused seismic waves and initiated tsunami-sized ocean waves, resulting in slump deposits that likely initiated widespread salt motions within the Gulf basin.

Cenozoic to Present

The structural history of the northern Gulf of Mexico during the Cenozoic is dominated by salt and gravitational tectonics to help accommodate large amounts of prograding siliciclastic sediments. Growth faulting is the main type of structuration seen at the Pelican Sequestration Hub, which is just north of the South Louisiana Salt Basin along the flank of the Toledo Bend Arch (Figure AOR-9). Ewing (1991) defines growth faults as:

Major strike-elongate zones of normal faulting, occurring entirely within the sedimentary column.... These fault zones are intimately related in location and age to the prograding clastic shelf margin.... The faults can cause tremendous expansion of the upper-slope and shelf-margin marine clastic deposits....

There are three phases of growth faulting identified in the area: [REDACTED]

[REDACTED] is downdip of The Hub acreage, and does not penetrate the identified confining or injection targets.

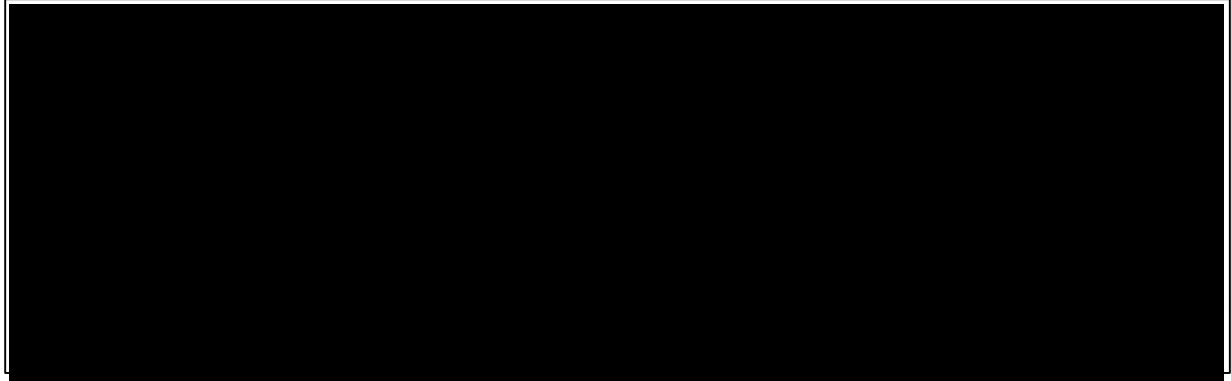


Figure AOR-10—Regional structural cross section highlighting the location of the Pelican Sequestration Hub. Cross section locations defined on Figure AOR-9. (Created from Adams, 1997, and Snedden and Galloway, 2019).

2.2.6 Historical seismic activity

Regional earthquakes and locations were determined using the USGS online database and published data by the Louisiana Geological survey (Figure AOR-11). There were five earthquakes within 50 miles of the site. Three of these earthquakes have known magnitudes. Two occurred within 30 miles with a magnitude of 3.0 and the third was a magnitude 4.2 occurring more than 40 miles away. The USGS Long-Term Seismic Hazard Map (Figure AOR-12) indicates that this area is at relatively low risk of earthquake activity. The map is based on models looking at the fault-slip rates and frequency of earthquakes and represents the peak ground accelerations having a 2% probability of being exceeded in 50 years (USGS, 2018).

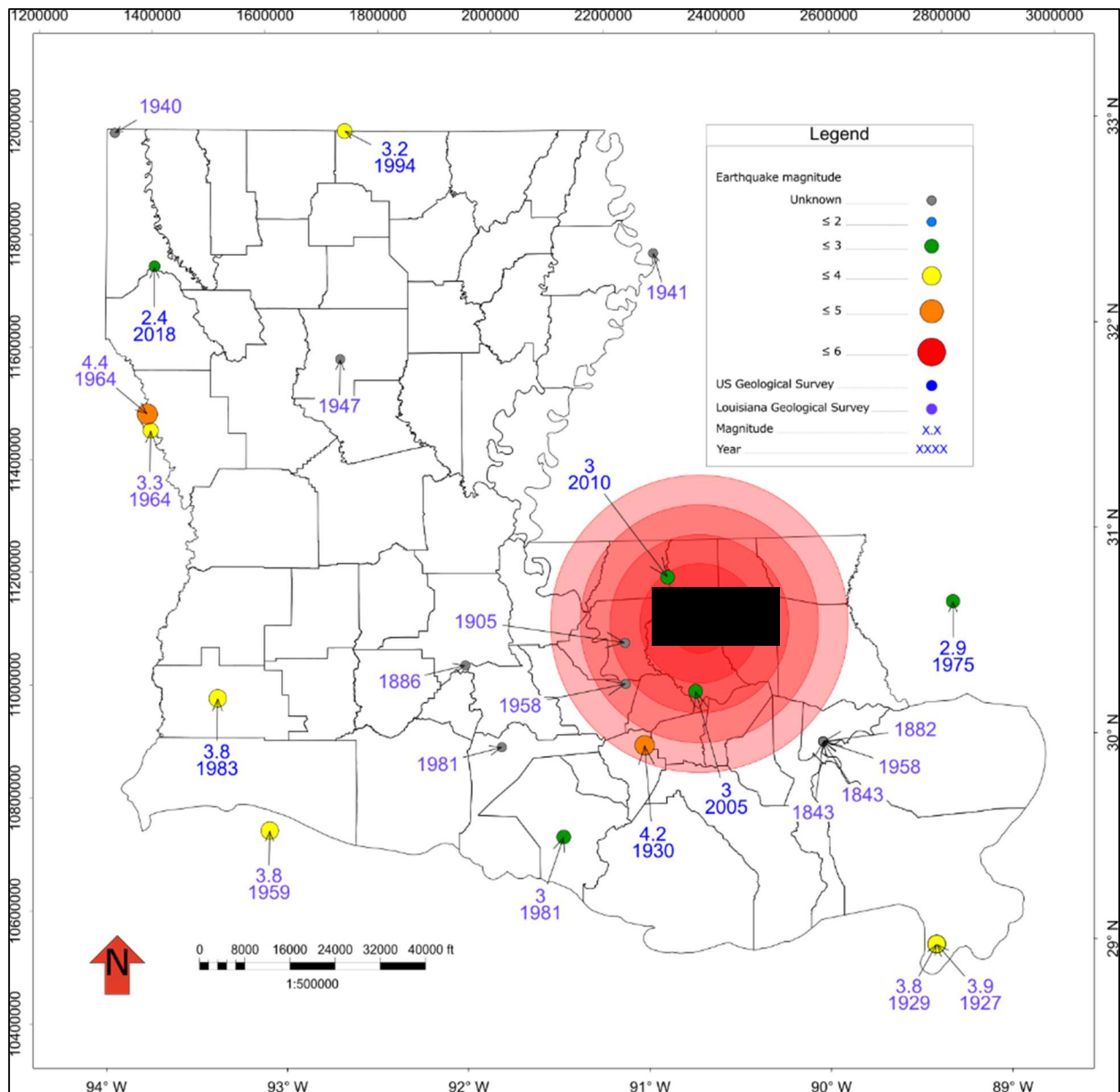


Figure AOR-11—Seismic activity recorded by the USGS (2023). Appendix E: Historical Seismicity Data tabulates the recorded seismicity data and their locations. The concentric red circles have radii of 10, 20, 30, 40, and 50 miles centered on the injection locations.

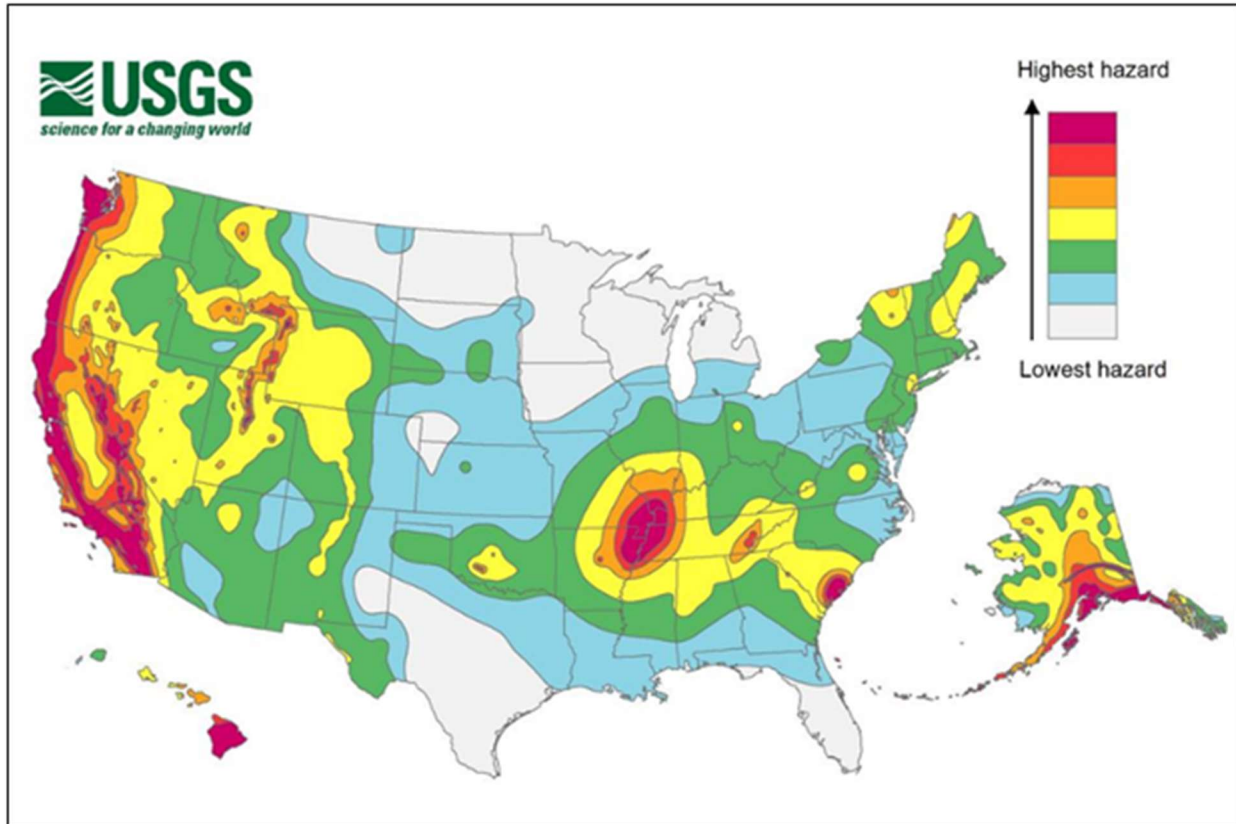


Figure AOR-12—Seismic hazard map showing that peak ground accelerations have a 2% probability of being exceeded in 50 years from USGS 2018 Long-Term National Seismic Hazard Map (USGS, 2018). Seismic hazard potential in the study area is one of the lowest in the USA.

2.2.7 Geopressure

A typical saline formation in the Gulf of Mexico basin has approximately 100,000 ppm dissolved solids and a hydrostatic pressure gradient of 0.465 psi/ft (Schlumberger, 2012). With depth, this transitions to overpressure at 0.7 psi/ft, and the onset of overpressure starts at about 0.6 psi/ft (Figure AOR-13). The onset of overpressure in the AOI is between [REDACTED] ft and [REDACTED] ft based on the USGS study published by Burke (2013, Figure AOR-14).

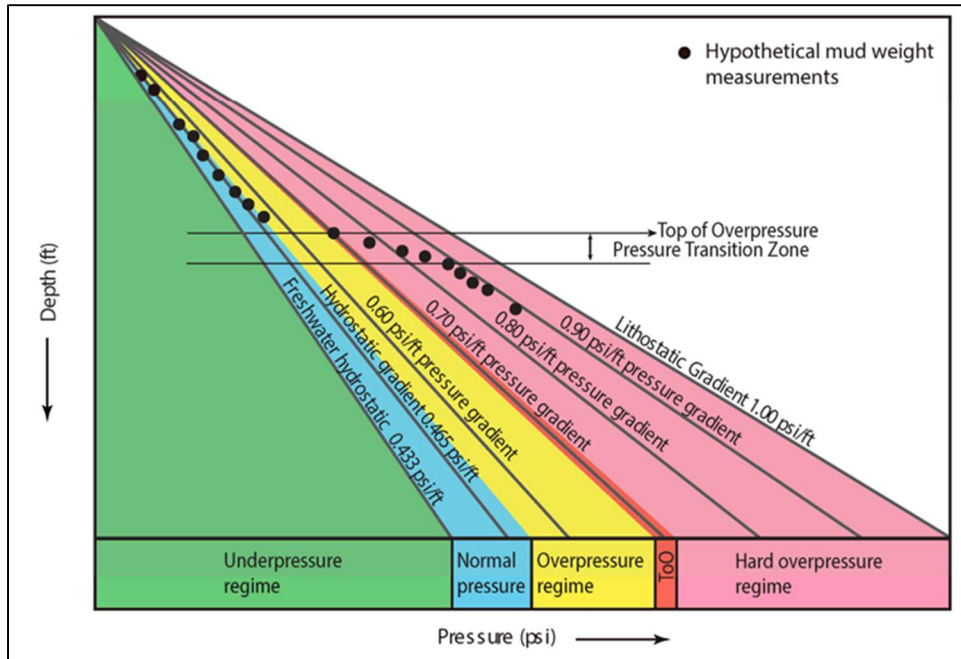


Figure AOR-13—Schematic diagram of generalized pressure gradients and their associated pressure regime (Schlumberger, 2012).

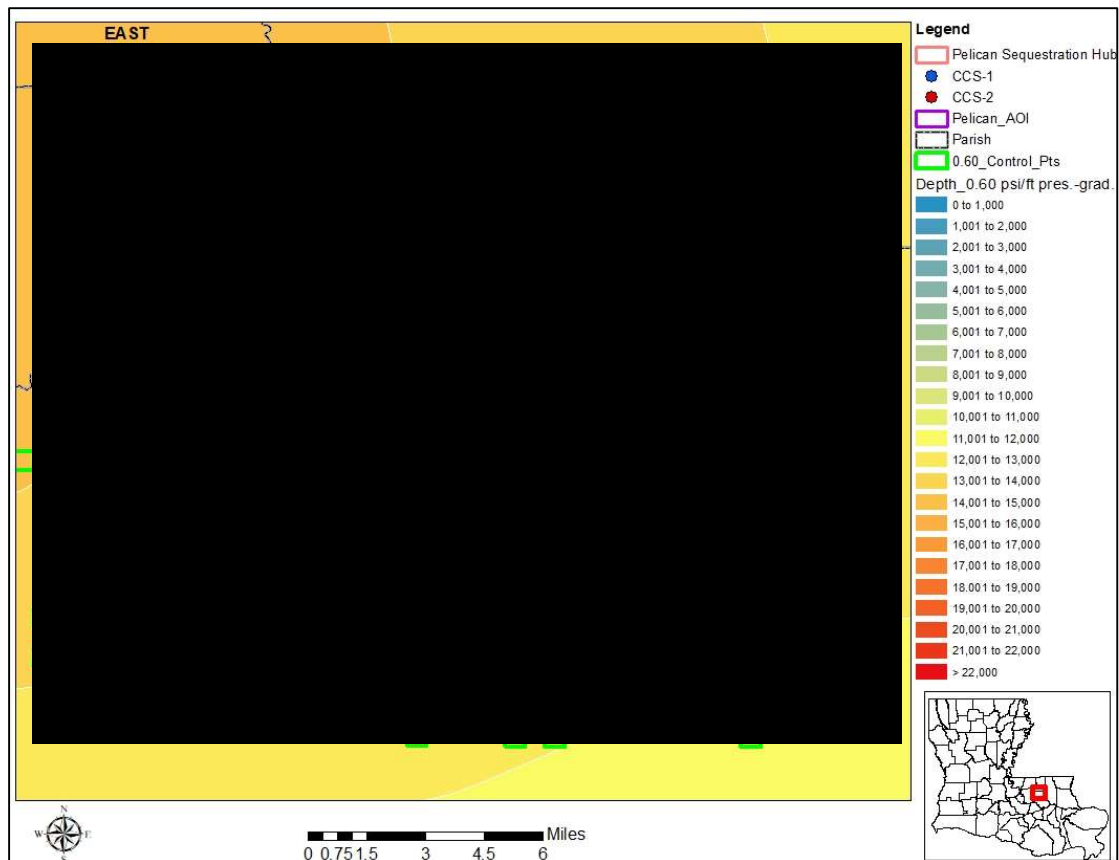
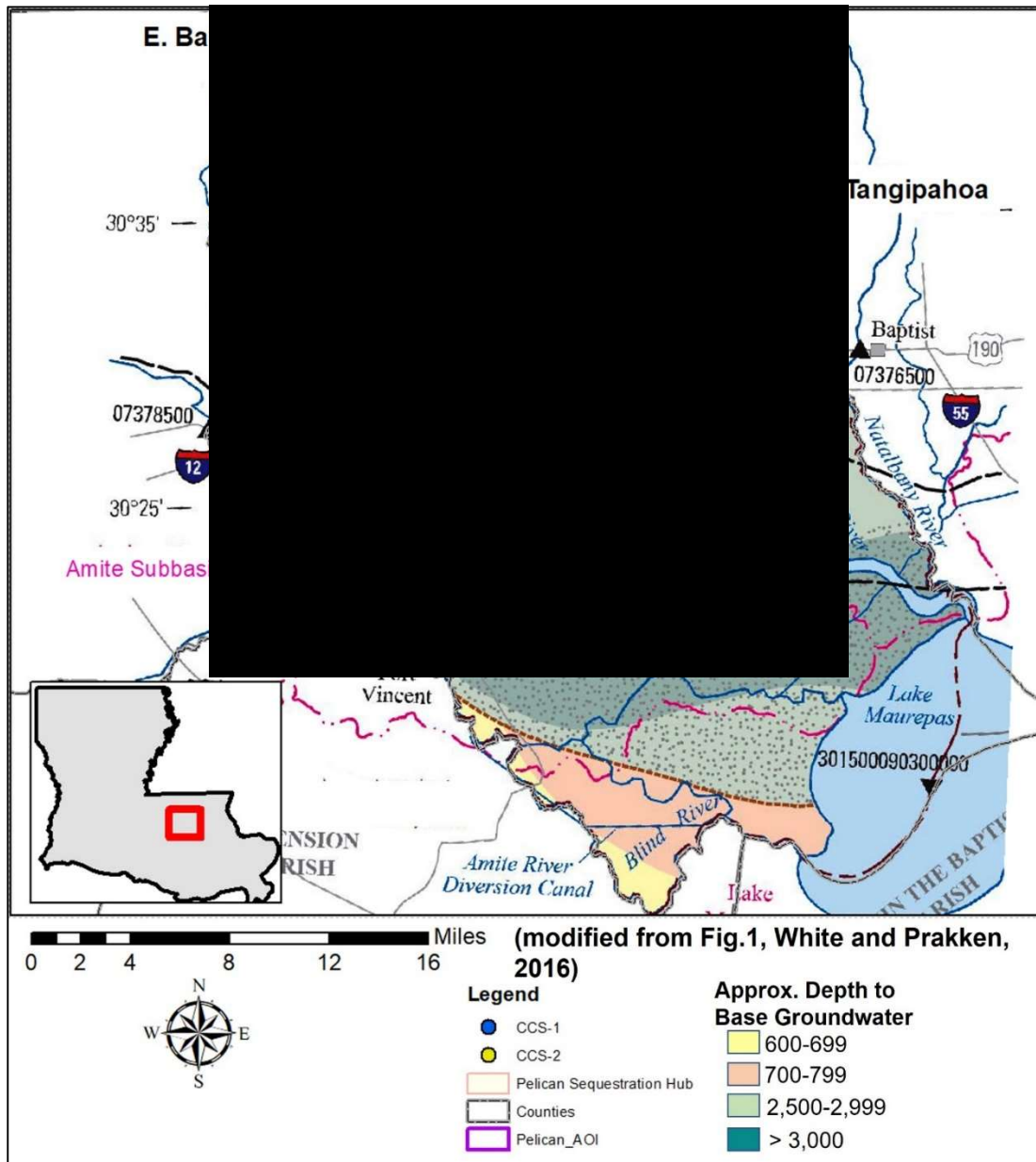


Figure AOR-14—Depth map for the onset of 0.6 psi/ft pressure gradient (Burke, 2013).

2.2.8 Fresh water aquifers

The Pelican Hub is located in the Tickfaw subbasin watershed above the Coastal Lowlands Aquifer System (Figure AOR-15). South of the Pelican AOI, the Denham Springs-Scotlandville fault system, an east-west trending growth fault, does not appear to affect groundwater hydrology (White and Prakken, 2016). There are three major freshwater aquifers that make up this system in southeastern Louisiana: Chicot Equivalent, Evangeline Equivalent, and Jasper Equivalent Aquifers (Figure AOR-16). Depth to the base of the freshwater aquifer systems (defined as 250 mg/L or less chloride concentration, White and Prakken, 2016) is expected to be [REDACTED] ft or shallower.



Time (Ma)	Series	Stage	Clastic Supply	Aquifer System or Confining Unit
0			Low High	
	Pleistocene			Chicot equivalent aquifer system "400-foot" sand and "600-foot" sand
	Pliocene	L		Evangeline equivalent aquifer system "800-foot", "1000-foot", "1,200-foot", "1,500-foot", and "1,700-foot" sands
		E		
5				Unnamed Confining Unit
10	Miocene	L		Jasper equivalent aquifer sands "2,000-foot", "2,400-foot", "2,800-foot"
		M		Unnamed Confining Unit
15				Regional Start of Saline Aquifer
20		E		

Figure AOR-16—Stratigraphic column summarizing the geohydrologic units of southeastern Louisiana

The aquifer systems are all southerly dipping and made up of discontinuous deposits of silt, sand, and gravel separated by layers of clay and sandy clay (Griffith, 2003) (Figure AOR-17).

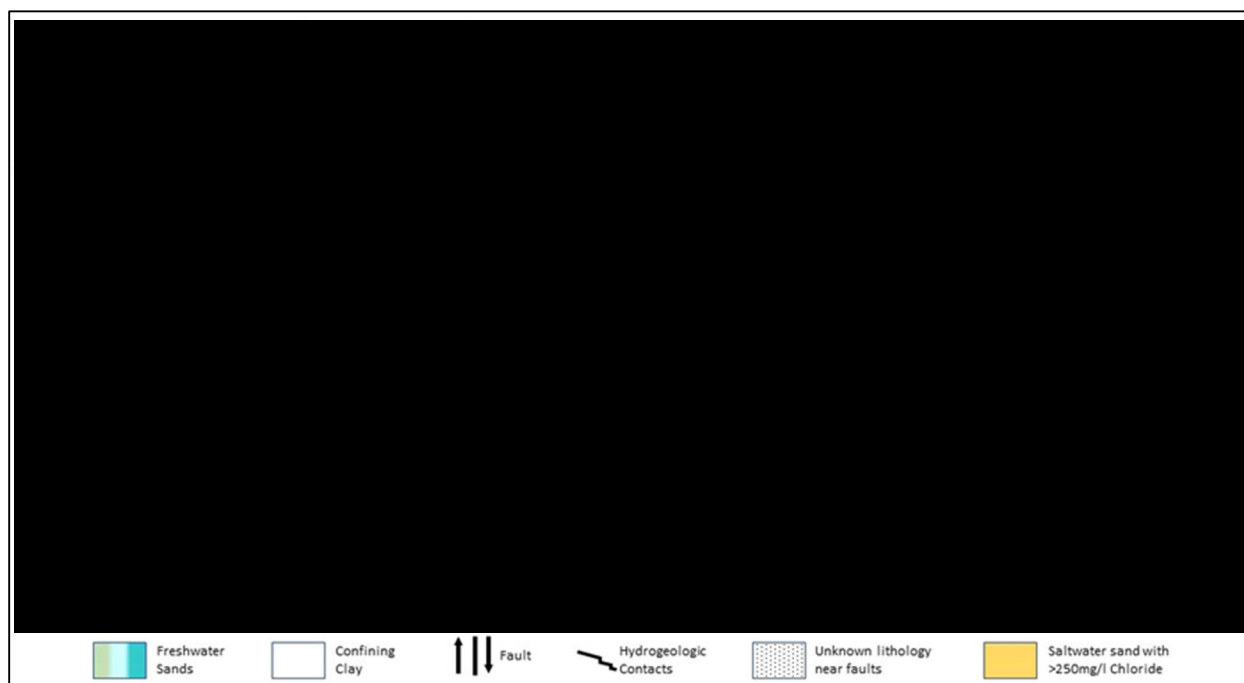


Figure AOR-17—Generalized hydrogeologic cross section C-C'. Location shown on Figure AOR-15. (modified from Griffith, 2003)

The primary aquifer in the area is the Chicot Equivalent Aquifer System. There are more than [REDACTED] wells sourcing this aquifer that range in depth from 10 ft to 550 ft. This is the primary source for domestic water consumption, but it is also used for agriculture, public supply, oil and gas, and industrial usage. The second source of freshwater is the Evangeline Equivalent Aquifer System, which is accessed by [REDACTED] wells drilled at depths of 300 ft to 1,900 ft. The primary uses for these aquifers are domestic and public consumption. The least used aquifer is the Jasper Equivalent Aquifer System at 1,600 to 2,950 ft deep. This aquifer is accessed through [REDACTED] wells and is primarily used for public supply. There are more than [REDACTED] water wells within the AOI, of which nearly [REDACTED] are active wells (Table AOR-1).

Table AOR-1—Summary of Louisiana Well Registration Records for Water Wells Within Pelican Hub AOI

	Chicot Surface Confining	Chicot Equivalent	Evangeline Equivalent	Jasper Equivalent
Depth Range	< 20 ft	10–550 ft	300–1,900 ft	1,600–2,950 ft
Aquifer Use				
Plug & Abandon		[REDACTED]	[REDACTED]	[REDACTED]
Domestic		[REDACTED]	[REDACTED]	[REDACTED]
Public Supply		[REDACTED]	[REDACTED]	[REDACTED]
Agriculture		[REDACTED]	[REDACTED]	
Oil/Gas		[REDACTED]		[REDACTED]
Industrial		[REDACTED]	[REDACTED]	
Test		[REDACTED]	[REDACTED]	
Monitor	[REDACTED]	[REDACTED]		
Well Count	[REDACTED]	[REDACTED]	[REDACTED]	[REDACTED]

Distribution of the deepest wells (blue circles) along with depths of aquifer screens are denoted on Figure AOR-18. Water wells in the Pelican Hub project area are predominantly draining the Chicot Aquifer (<550 ft) with [REDACTED] wells accessing fresh water from the deeper Jasper aquifer. The Li-52, displayed as a red star on Figure AOR-18, is a monitoring well used by the USGS to test, study, and monitor the Evangeline Aquifer system.

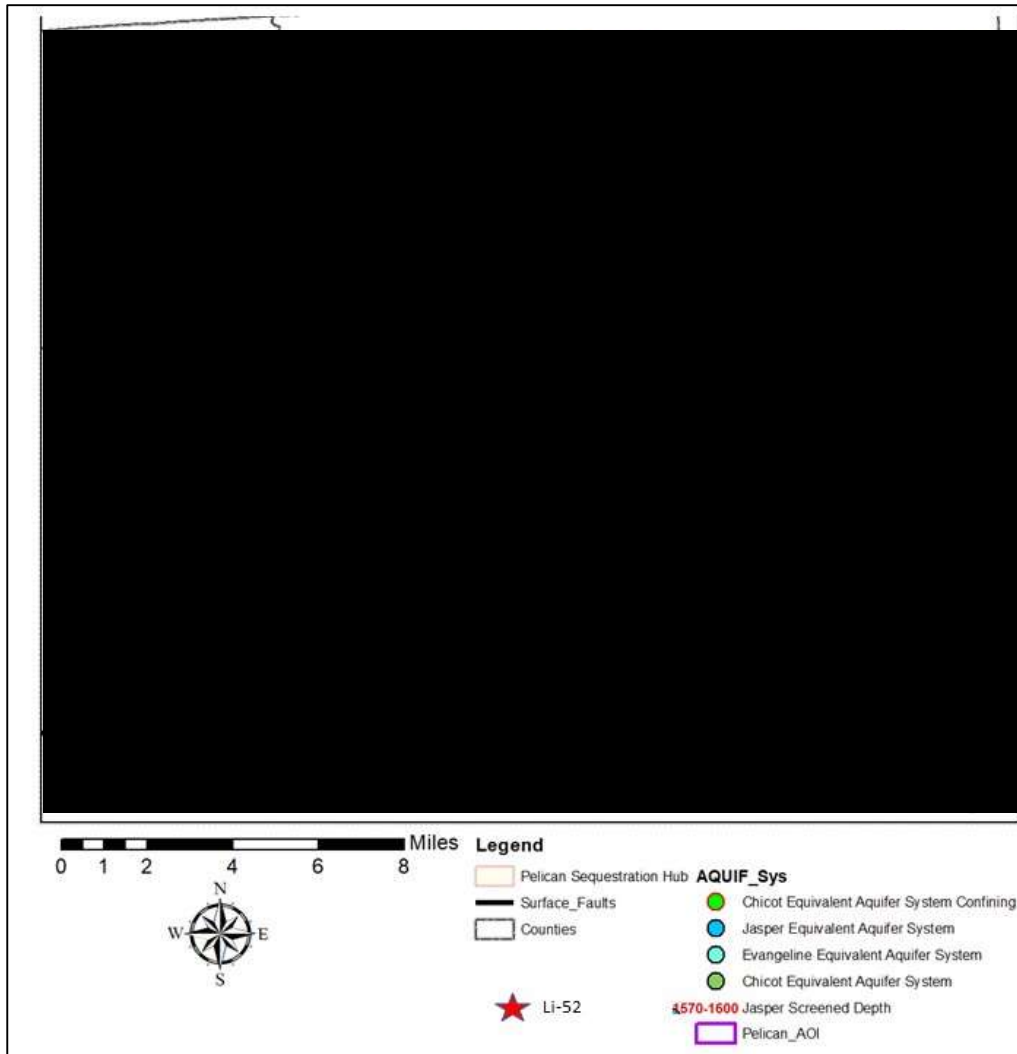


Figure AOR-18—Water wells within the Pelican Hub, as recorded in the Louisiana state well register.

Aquifer recharge is primarily through the percolation of precipitation into the aquifer sands at surface outcrop locations. The recharge area for the Evangeline and Jasper Equivalent Aquifers are [REDACTED], extending into Mississippi (Figure AOR-19). The Chicot Equivalent Aquifer sands are charged locally where the sands reach the surface or where rivers erode into them. Generally, there is a clay layer that is present at or near the surface in Livingston Parish that slows such recharge (Tomaszewski, 1988; Figure AOR-17).

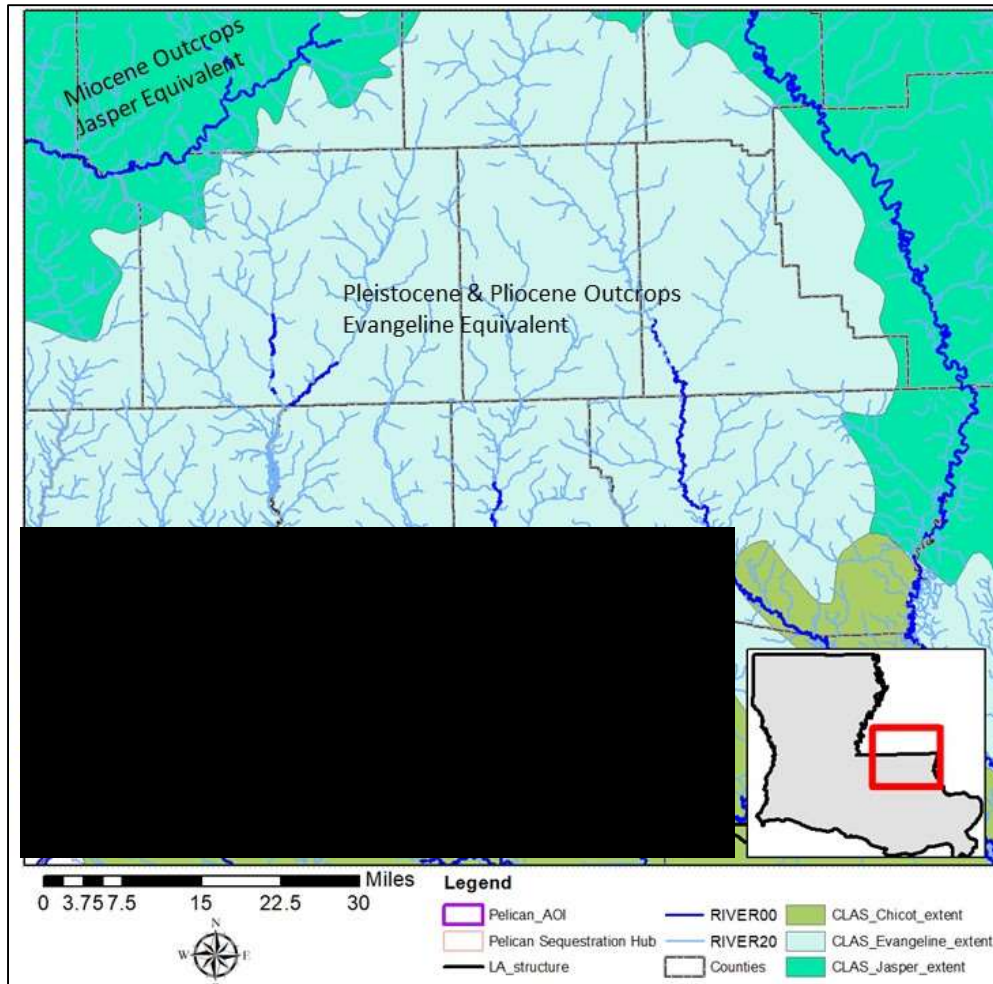


Figure AOR-19—Surface geological map from USGS Aquifer Extent shapefiles. This represents surface exposure, defining updip locations for aquifer recharge.

Study of the Denham Springs-Scotlandville Fault shows little evidence of effects on the aquifers (Tomaszewski, 1988). The Baton Rouge Fault, located south of the Denham fault, does affect the hydrogeology by separating fresh water (north and upthrown) from saline sand strings interbedded with fresh (south and downthrown) (Griffith, 2003, Figure AOR-17).

2.2.9 Defining the base of the underground source of drinking water (USDW)

The Louisiana Department of Natural Resources (LDNR) determines the USDW depth to be at the base of the permeable formation in which the resistivity curve crosses below 2 ohm-m (Figure AOR-20). This depth is 3,355 ft in the Pelican MLR 004 and is consistent with the onset of saline aquifers. This guidance was followed when picking the base of the USDW in ■ wells in the AOI (Figure AOR-21).

Pelican MLR 004

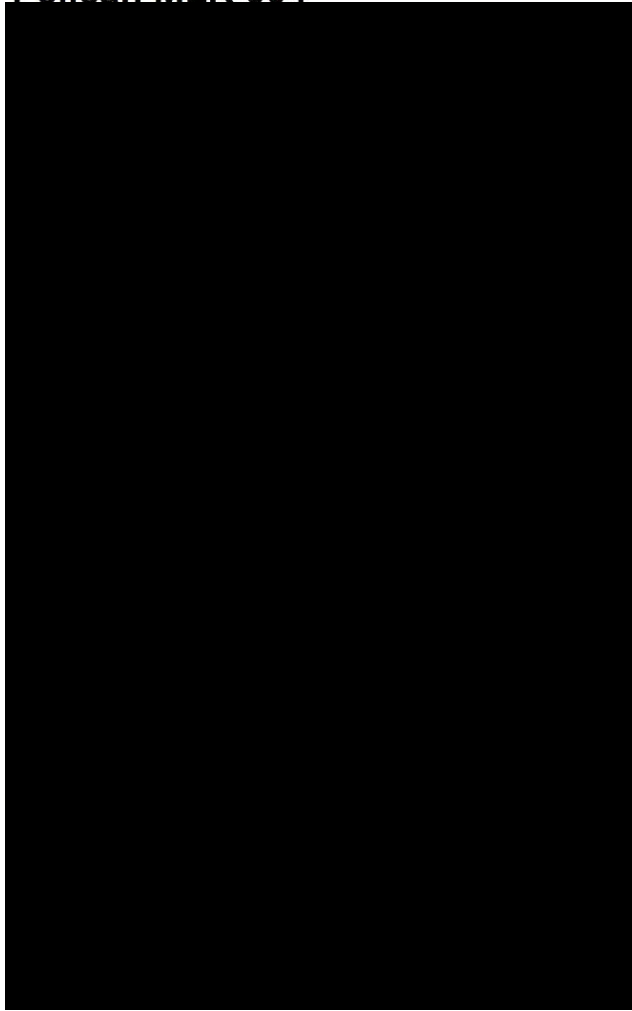


Figure AOR-20—Log plot from Pelican MLR 004 with LDNR base of USDW at 3,355 ft MD.

The depth of the USDW deepens southward in the project acreage, varying from about 2,800 ft subsea in the north to 3,400 ft subsea in the south (Figure AOR-21). The caprock of the targeted storage complex is about [REDACTED] ft subsea, providing about [REDACTED] ft of saline aquifers between the caprock and USDW sands. The structural cross section in Figure AOR-22 shows a deepening of the USDW from north to south.

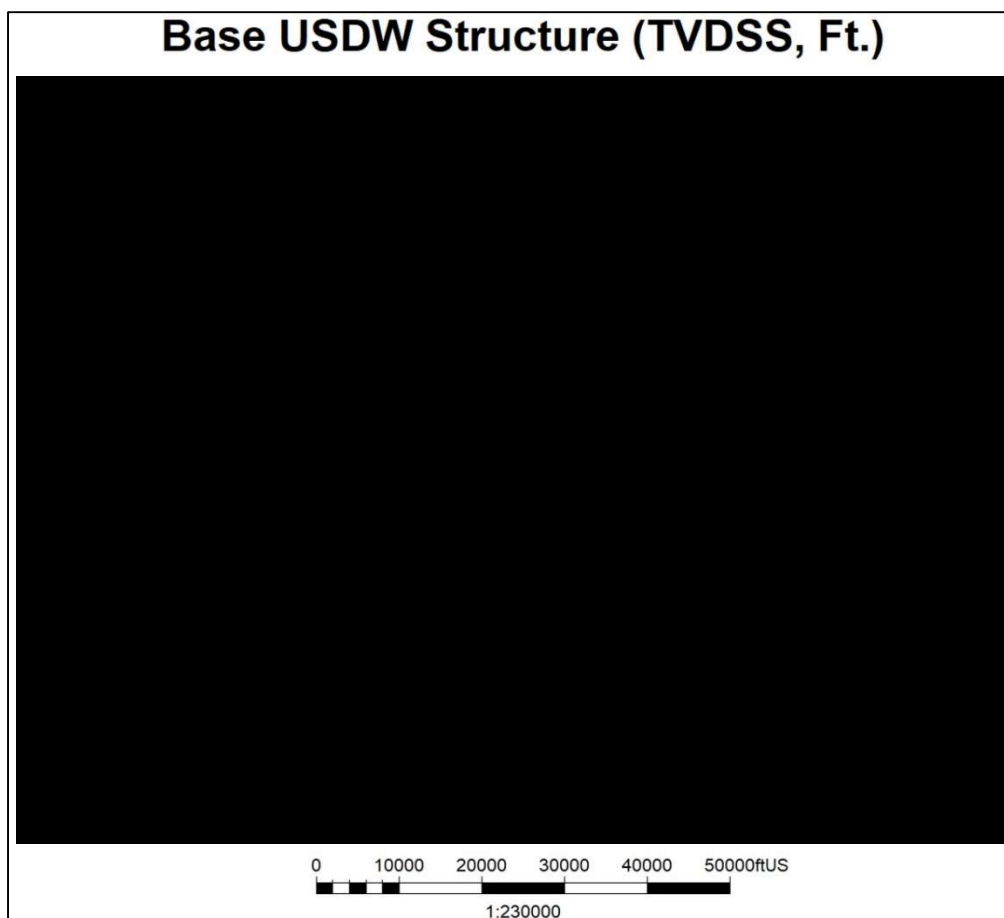


Figure AOR-21—Structure map of the base of the USDW defined using 17 wells. The location of the Pelican MLR 004 (star) is indicated on the map.

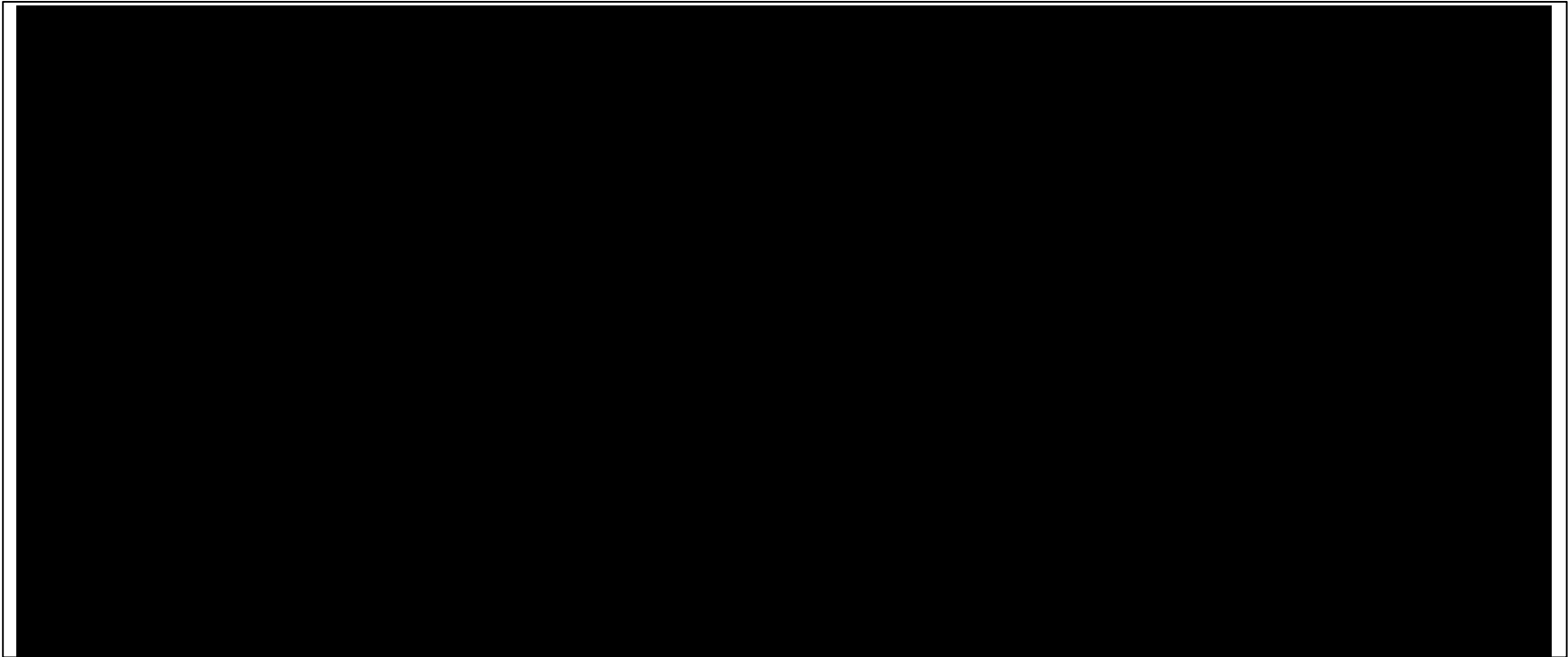


Figure AOR-22—North to south cross section illustrating interpretation of the base USDW and structural dip toward the south.

2.3 Model domain

Figure AOR-23 displays the project acreage in Livingston and St. Helena Parishes (in yellow) and legacy wells in the area for which a geomodel was built to quantify CCS potential and to plan for site development. The active oil fields nearby include Beaver Dam Creek, Lockhart Crossing, and Livingston. All three produce from the deeper Wilcox or Tuscaloosa formations and are outside the project acreage. CO₂ injection has been implemented in the Lockhart Crossing field (Wood, 2011). A CO₂ EOR pilot was planned in the Livingston field, but it was never implemented due to low oil prices (Hite, 2016). Within the [REDACTED]-acre project acreage, there are [REDACTED]. Within the eastern development area, where the proposed CCS 1 well would be located, there is [REDACTED]. Abandoned and legacy wells are discussed further in Section 5.0 Corrective Action.

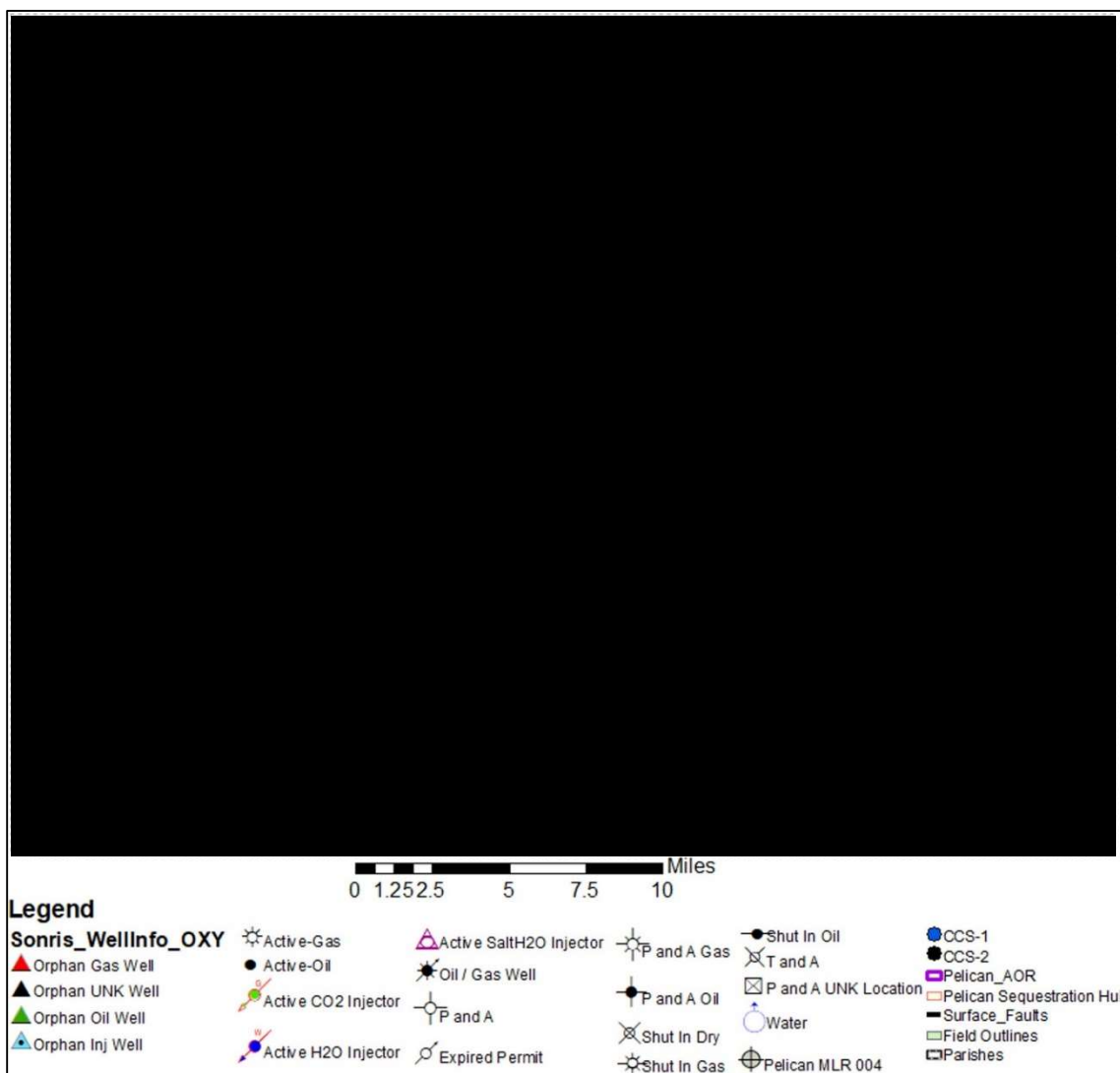


Figure AOR-23: Map of the Pelican CCS geomodel area within the purple polygon, Oxy acreage in the yellow shaded area, and legacy wells in the region. Detailed information about these legacy wells is tabulated in

Appendix B: Table of Wells.

The project technical services team conducted a detailed geologic evaluation and constructed a geologic model using Schlumberger Petrel (v2020) over an approximately ■-square-mile area of investigation (AOI) (purple polygon in Figure AOR-24). This was achieved using a large body of data, including literature, remote sensing data (LIDAR), 2D and 3D seismic surveys, licensed well data, and public well data from SONRIS.com. The well database includes 84 wells with geological tops and petrophysical analyses, eleven wells with core data, one (1) well with paleontological control (Warren, 1957), and 17 wells with shallow Gamma Ray and Resistivity logs to define the base of the USDW. The core database consists of ten (10) historical wells with sidewall core (SWC) data scattered throughout the geological section and one stratigraphic test well, the Pelican MLR 004, drilled by the project team with whole cores and SWCs from key confining and injection intervals. Detailed information collected and analyzed to date from the Pelican MLR 004 is included in Appendix C: Site-Specific Data and Procedures. One (1) 3D seismic cube was used as the basis of the evaluation.

Figure AOR-24 displays the 59 wells with quality logs and reservoir top data that were used, in conjunction with 3D seismic data, to construct the reservoir horizons. These wells also had the appropriate digital logs for petrophysical analysis and for use in building the property models. Detailed information about these wells is tabulated in

Appendix B: Table of Wells.

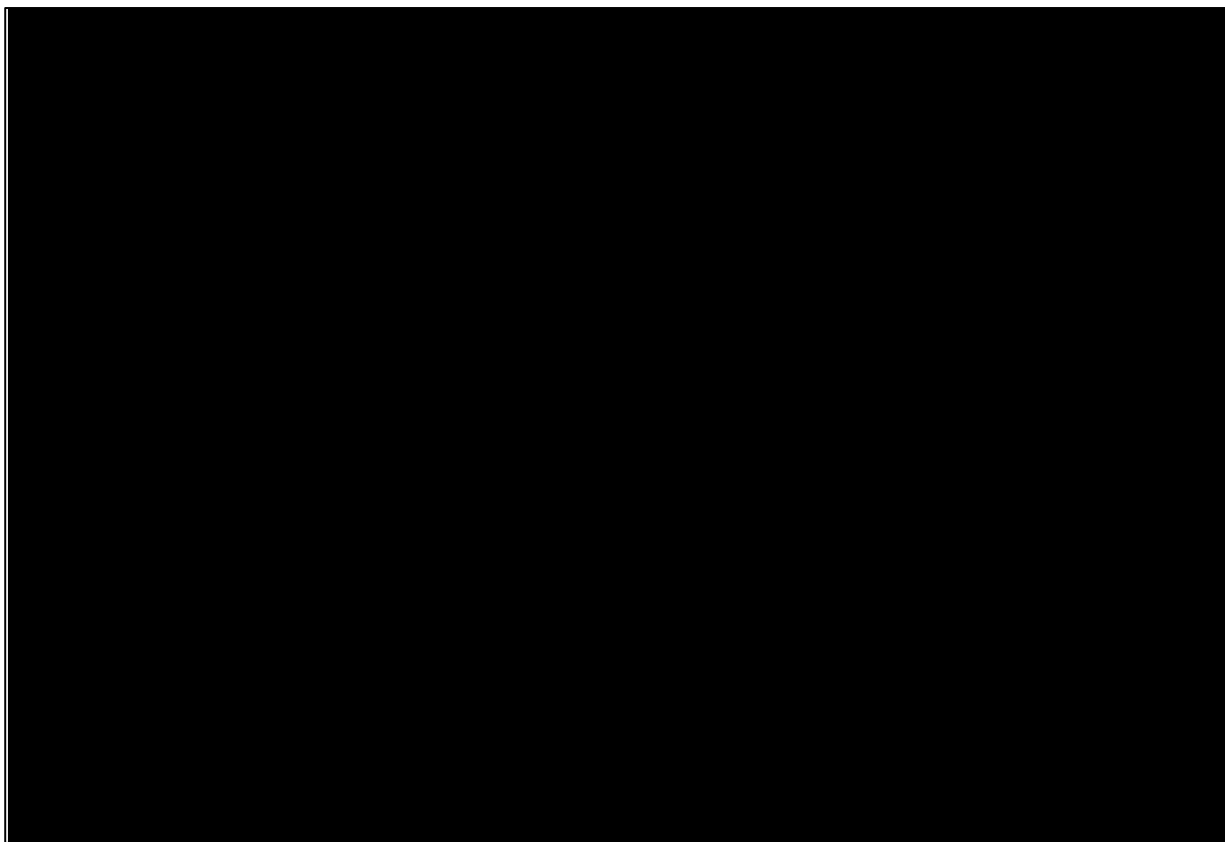


Figure AOR-24—Map of the Pelican CCS geomodel area inside the pink outline. Blue dots are the 59 wells with Vshale and porosity logs that were used to develop reservoir property distributions in the model. The blue outline is the 3D seismic survey coverage.

The methodology for using the static geomodel

[REDACTED]

Figure AOR-1 displays the locations of the Pelican CCS 1 and CCS 2 wells, for which we are applying for Class VI injection permits. Also, shown is the location of the stratigraphic well, Pelican MLR 004, which has been drilled to gather key reservoir and performance data to support this supplication.

The model domain coordinate reference system is summarized in Table AOR-2.

Table AOR-2—Geologic Model Domain Information

Coordinate System	[REDACTED]		
Horizontal Datum	[REDACTED]		
Coordinate System Units	[REDACTED]		
Zone	[REDACTED]		
FIPZONE	[REDACTED]	ADSZONE	[REDACTED]
Coordinate of X min	[REDACTED]	Coordinate of X max	[REDACTED]
Coordinate of Y min	[REDACTED]	Coordinate of Y max	[REDACTED]
Elevation of top of domain	[REDACTED]	Elevation of bottom of domain	[REDACTED]

2.3.1 Model geologic structure

Both 2D and 3D seismic data were available for use in the evaluation of the Pelican site. Initial evaluation of the area was done using a sparse grid of licensed 2D seismic data of various vintages and quality that were acquired during the last 60 years. Upon leasing the pore space, approximately [REDACTED] square miles of 3D seismic data were licensed. As shown in Figure AOR-25, [REDACTED]

Table AOR-3: 3D Seismic Acquisition Parameters

Acquisition Parameter:	
Recording Template	[REDACTED]
Receiver Geometry	[REDACTED]
Source Geometry	[REDACTED]
Trace Density	[REDACTED]
Energy Source Type	[REDACTED]
Energy Source Details	[REDACTED]
Recording Instruments	[REDACTED]
Nominal Far Offset	[REDACTED]
Nominal Fold	[REDACTED]
Acquisition Bin Size	[REDACTED]
Record Length	[REDACTED]
Acquisition Period	[REDACTED]

Initial evaluation of the area was conducted using the available 2D data in time domain. Wells with compressional sonic logs close to 2D lines were used to [REDACTED]

The 3D data set was [REDACTED]

After licensing the 3D seismic data, [REDACTED] wells were identified within the survey that had compressional sonic logs covering all or significant portions of the interval of interest. These [REDACTED] wells were tied to the time seismic data using [REDACTED] (Figure AOR-26). No phase rotation was necessary to get good ties (Figure AOR-27).



Figure AOR-25—Map of wells within the 3D seismic survey area (red boundary) that were used for synthetic well ties. Wells are listed in Appendix B: Table of Wells.

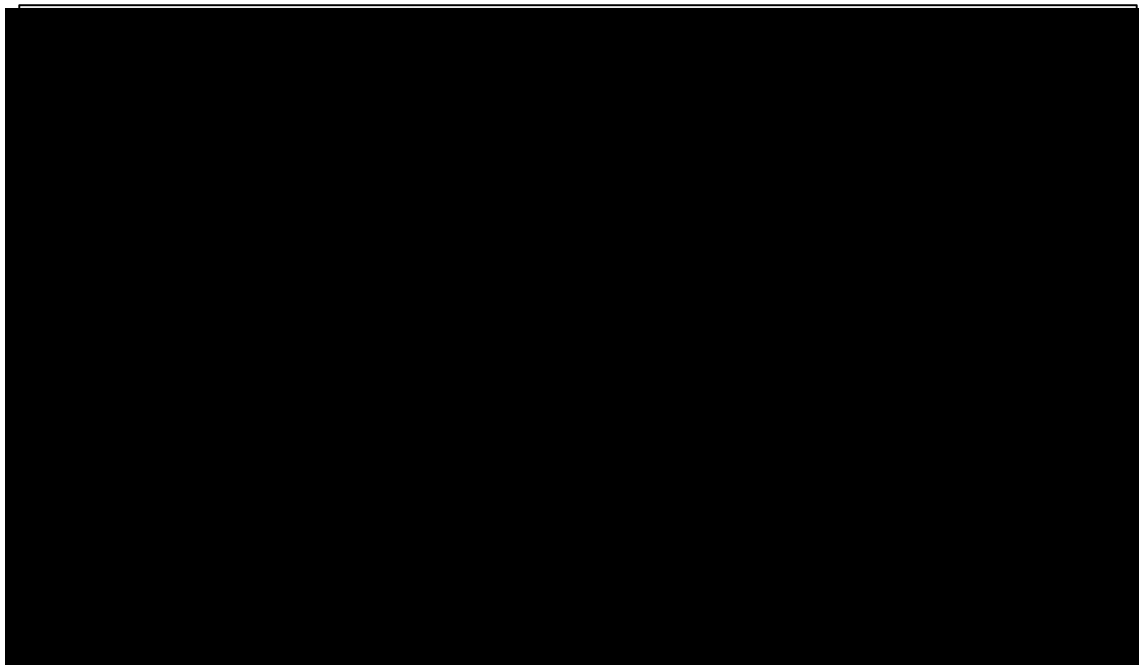
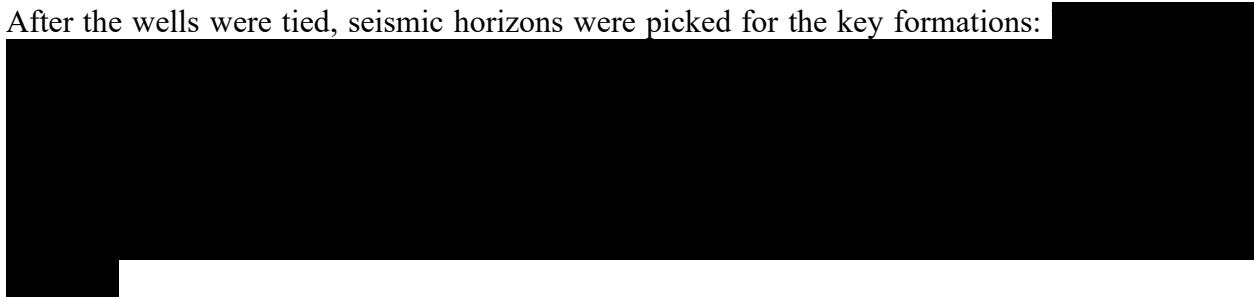


Figure AOR-26—Extracted wavelet used for synthetic well ties.



Figure AOR-27—Example well tie of the Weyerhaeuser 57 well to the seismic data.

After the wells were tied, seismic horizons were picked for the key formations:



Faults were also picked within the seismic cube. The intersection of these faults with the seismic horizons are shown on the maps in Figure AOR-28, Figure AOR-29, and Figure AOR-30 for the [REDACTED] formations, respectively. Very few faults are localized in the southern portion of the survey (Figure AOR-29). Within the leased acreage, seismic images do not show that the faults cut up through the [REDACTED] (Figure AOR-30).

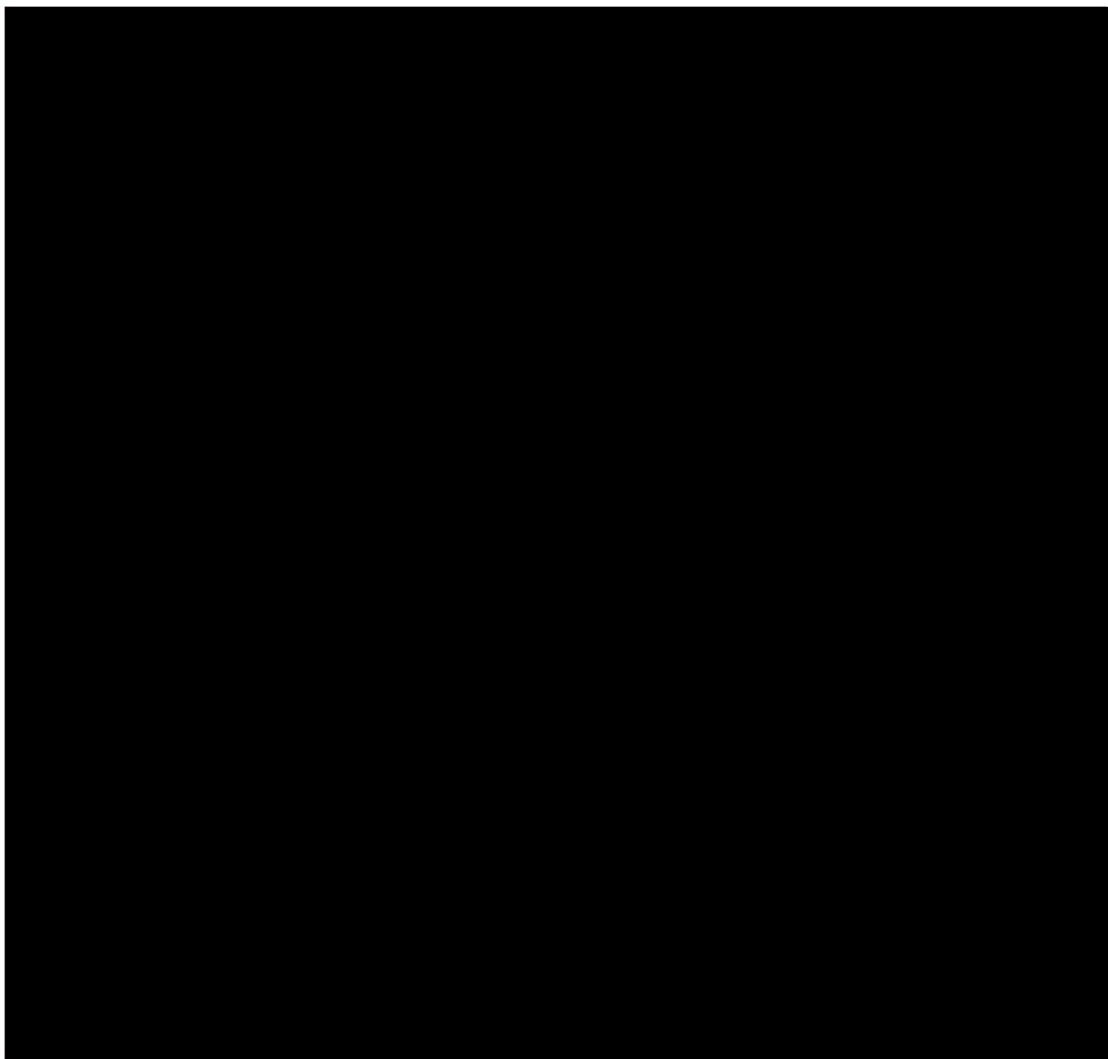


Figure AOR-28—Top surface of the [REDACTED] interpreted from 3D seismic data tied to well logs. Also displayed are faults cutting through the surface.

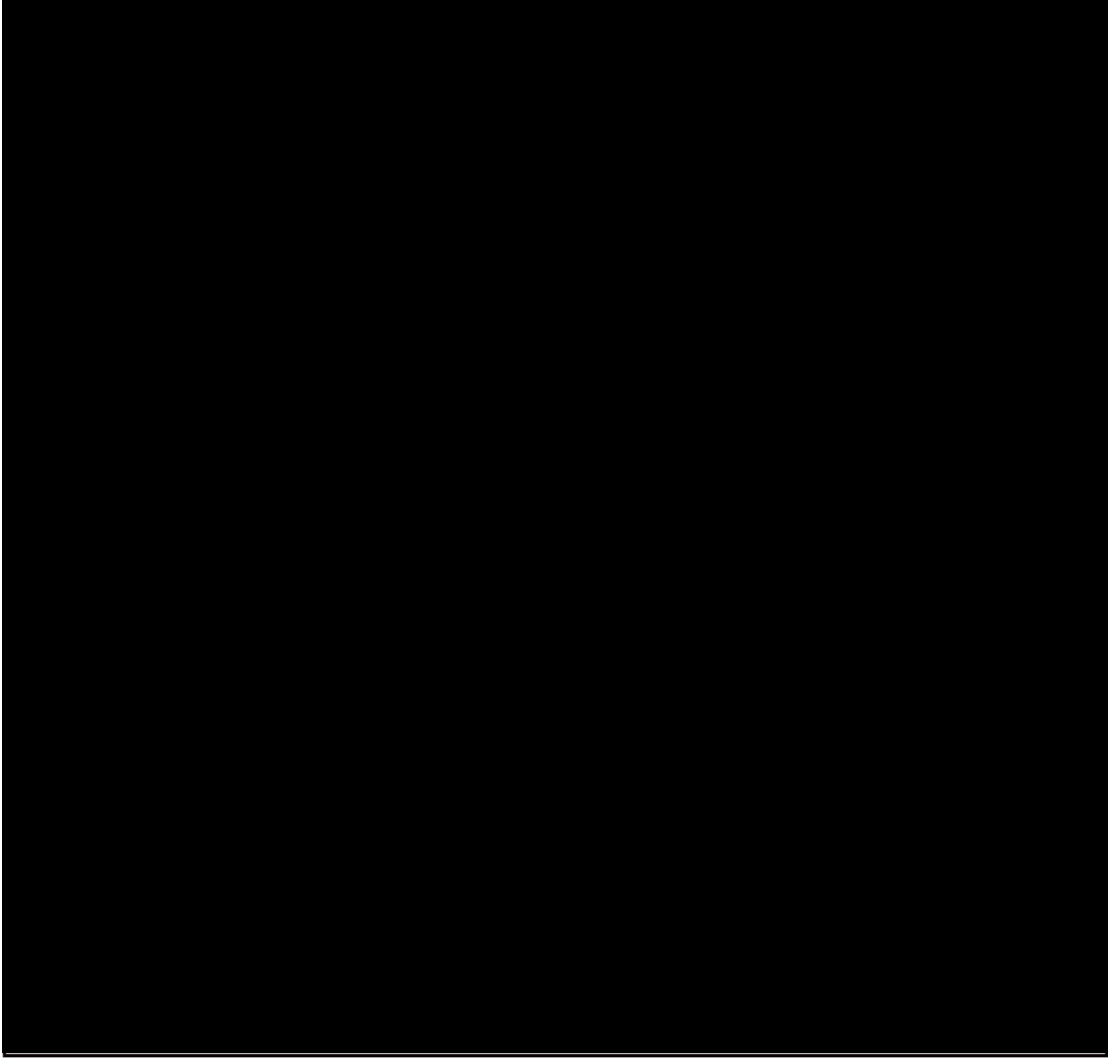


Figure AOR-29—Top surface of the [REDACTED] interpreted from 3D seismic data tied to well controls. Also displayed are faults cutting through the surface.

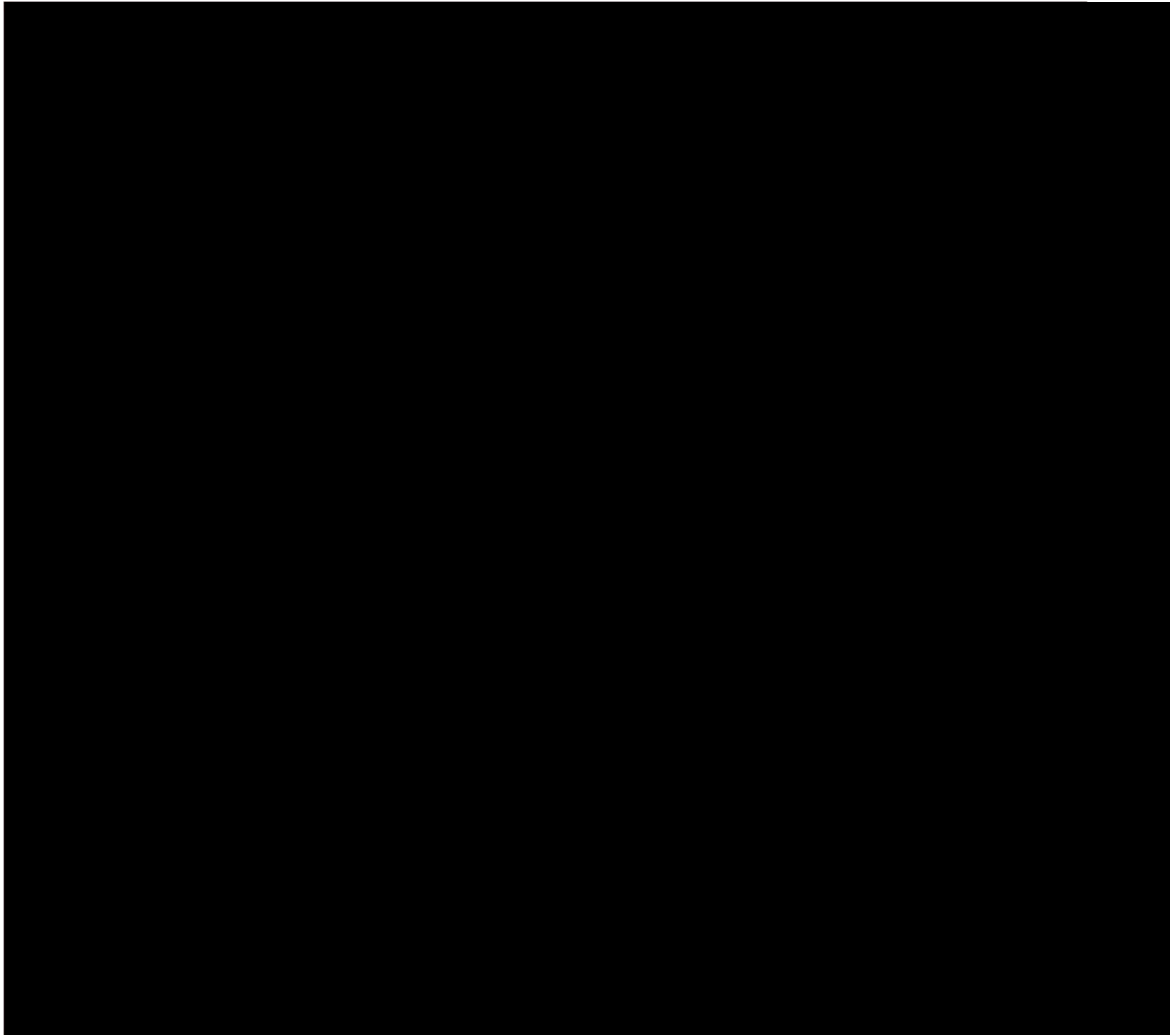


Figure AOR-30—Top surface of the [REDACTED] interpreted from 3D seismic data tied to well controls. Also displayed are faults cutting through the surface. Note that there are no faults cutting through the [REDACTED] seal within the Oxy acreage.

Figure AOR-31 displays the [REDACTED] top surface, which was developed using 3D seismic horizons tied to well tops, displayed as white dots. The surface dips gently toward the SSW at about [REDACTED] ft per mile or about [REDACTED]°. The relatively uniform dip structure supports no faults or salt diapirs within the area of investigation and leased acreage.

Major faults trending in the east-west direction were identified south of the geomodel domain based on a documented regional interpretation of the Gulf Coast (Figure AOR-9 and Figure AOR-29). The orientation of the major faults is in the east-west direction, which is believed to be following the major Gulf Coast regional SHmax orientation. These faults are deep-seated and cut through the CO₂ storage reservoir outside of the geomodel domain (Figure AOR-29), [REDACTED] of the Pelican Hub.



Figure AOR-31—Top surface of the [REDACTED] interpreted from 3D seismic data and geological zone tops. Well data control points are displayed as white dots. Detailed information of the control wells are summarized in

Appendix B: Table of Wells.

2.3.2 Geologic model zones and layering

The model includes three major geological intervals— [REDACTED] [REDACTED] – and spans an area of about [REDACTED]. The two upper geological intervals, [REDACTED], were divided into [REDACTED] zones to capture lithology variations. These zone tops are tied to well tops and are named [REDACTED].

Appended to these names are the main lithology in each zone: SH for shale, SS for sandstone, and LM for limestone. The [REDACTED] was divided into [REDACTED] zones and are named [REDACTED]. These zones do not have a lithology designation because they represent sand-shale sequences deposited in a fluvial-deltaic environment and house excellent quality sands paired with baffling or sealing shales. The [REDACTED] represent storage units. The lower confining unit is the thick [REDACTED], Figure AOR-32 in the model.

Figure AOR-32 depicts the geologic zones on a N-S cross section through the geologic model, which was built with an average grid cell size of [REDACTED]. [REDACTED]



Figure AOR-32—North-south cross section of three main geological intervals, [REDACTED], and their geological zones in the Petrel geological model. Note that [REDACTED] are four confining units above the [REDACTED] injection zone.



Figure AOR-33—A fence diagram displaying the 3D geologic model zones including the [REDACTED] (uppermost confining unit) to [REDACTED] zones (CO₂ injection zone).

2.4 Porosity and permeability

The fluvial-deltaic [REDACTED] formation is subdivided into [REDACTED] and composed of high-porosity, high-permeability sand layers with intermittent limestones and intrashale layers. The [REDACTED] is overlain by a regionally extensive [REDACTED] reservoir and low-permeability [REDACTED] that comprise the upper confining zone (Figure AOR-34). Underlying the [REDACTED] is the [REDACTED] that serves as the lower confining zone.

A total of 59 wells were selected for petrophysical calculation of porosity, permeability, and net reservoir thickness that provided the best data quality and coverage of the [REDACTED] subzones (see Figure AOR-35). Within the geomodel, 59

Plan revision number: 0
Plan revision date: 07/31/23

wells with petrophysical analyses were selected for 3D distribution of petrophysical properties as shown in Figure AOR-34 and listed in

Appendix B: Table of Wells. A summary of the average properties by zone is shown in Figure AOR-36

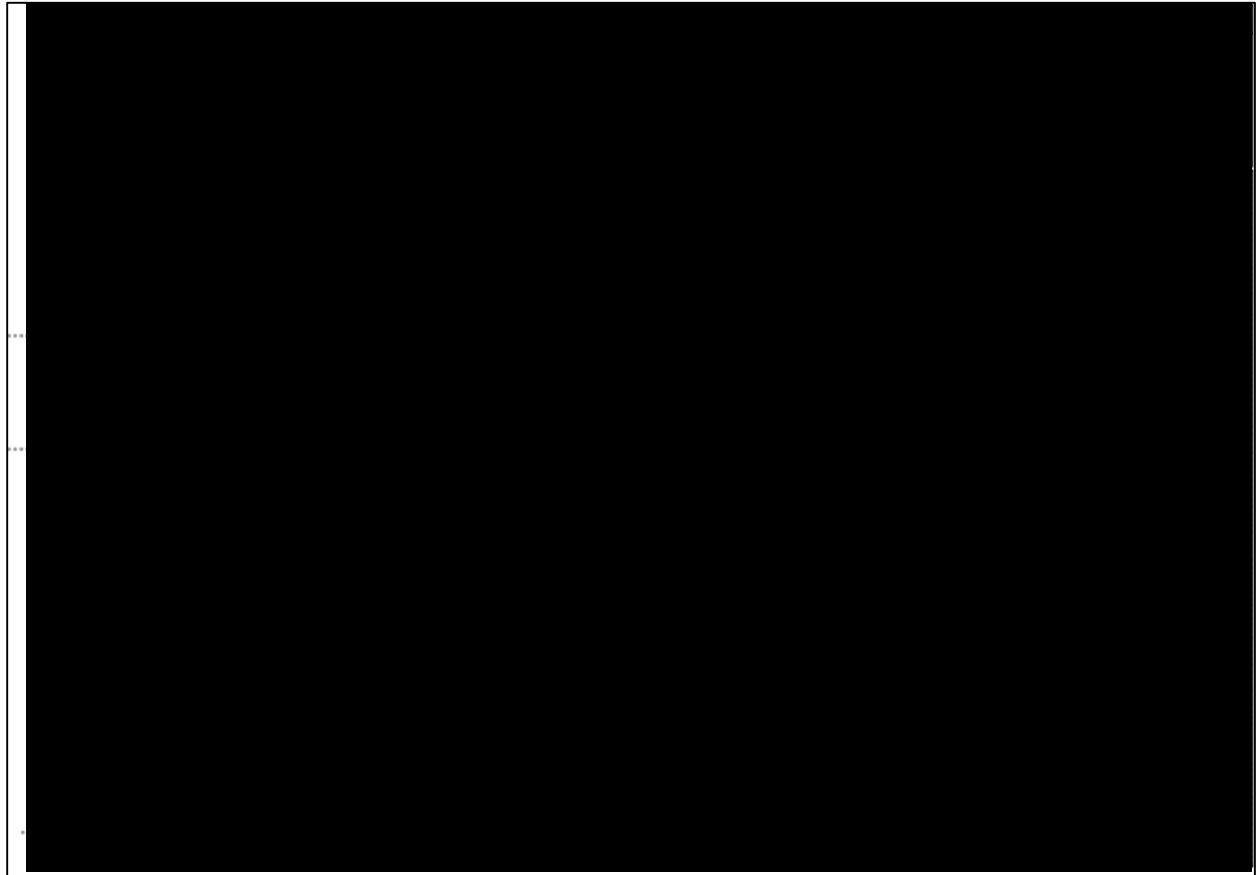


Figure AOR-34—Composite type well log interpretation from Pelican MLR 004 that shows the upper confining, injection, and lower confining zones with their corresponding gamma ray (XGR) readings, porosity (XPORE), and permeability (XPERM) in the subsequent tracks.

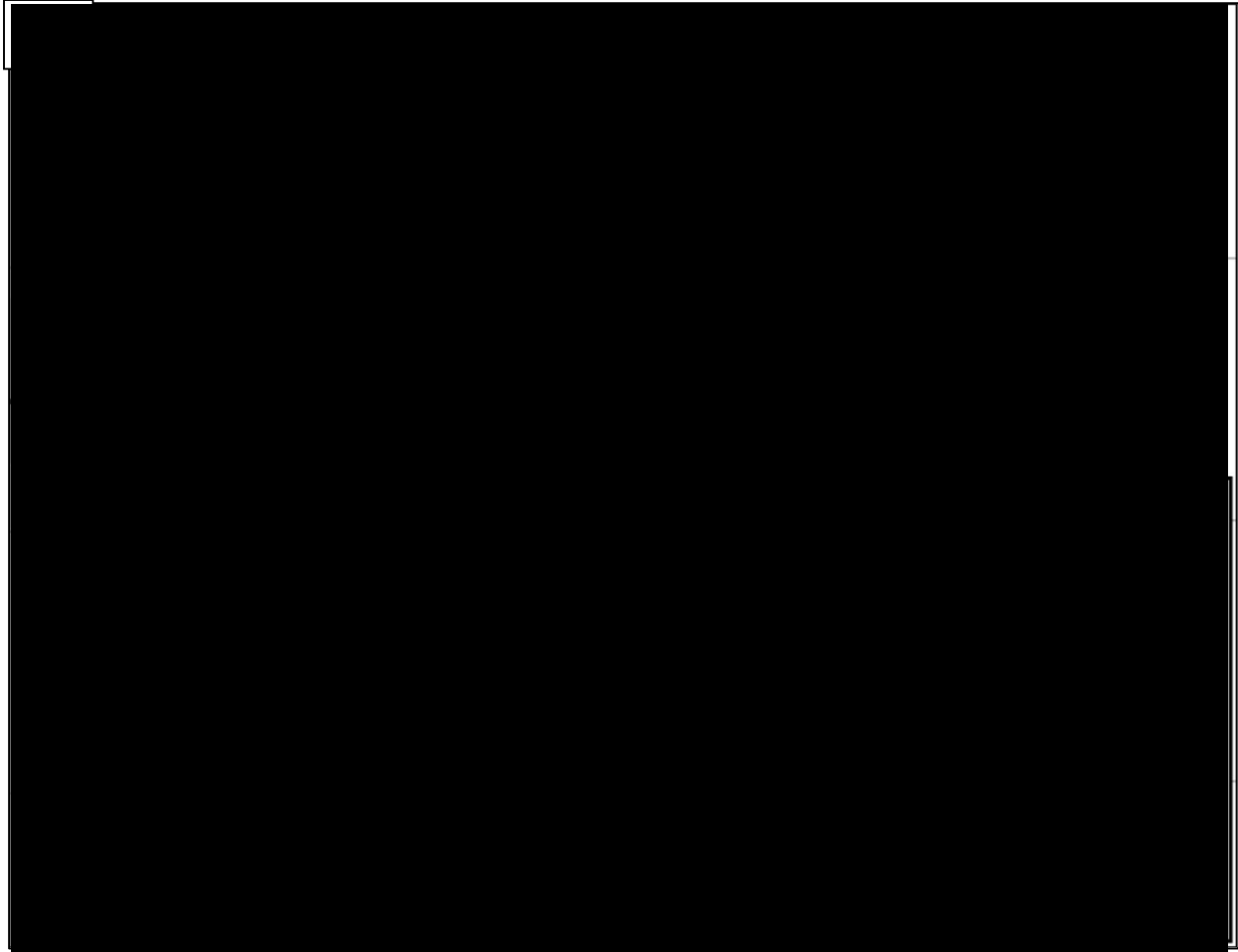


Figure AOR-35—Map representing the 59 control wells within and surrounding the Pelican Sequestration Project area (dotted line) used for petrophysical interpretation of porosity, permeability, and net reservoir thickness of the [REDACTED] subzones. Pie charts outlined in blue represent the nine wells with Neutron and Density well logs. The cored stratigraphic test well is located within the AOI (green star). Detailed information about these wells is found in

Appendix B: Table of Wells.

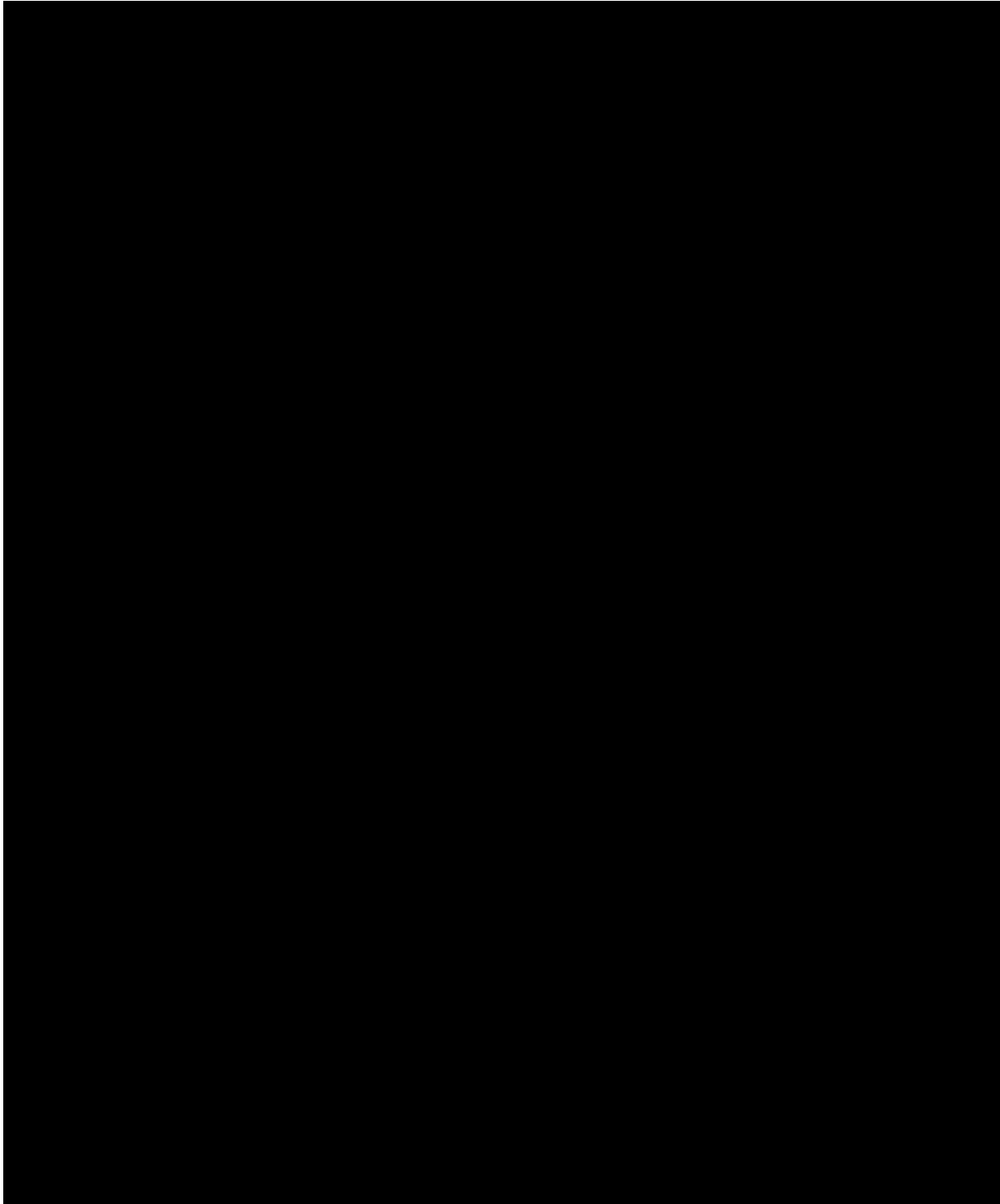


Figure AOR-36—Individual subzones in the geologic model and averages of porosity, permeability, and net reservoir thickness based on petrophysical analysis, along with approximate depth intervals at Pelican MLR 004 (Class V stratigraphic test well). Left column lists the top of model at [REDACTED] ft, the top of injection zone at

Plan revision number: 0
Plan revision date: 07/31/23

ft, and the base of the injection zone (bottom of the model) at ft. (Average reservoir properties used ≤ % shale as a cutoff.)

Net reservoir thickness was calculated

2.4.1 Porosity

The total porosity of the injection zone is based on

Table AOR-4—The Nine Wells Used to Calculate Total Porosity from the Neutron and Density Logs

Well Name	UWI
[REDACTED]	[REDACTED]
[REDACTED]	[REDACTED]
[REDACTED]	[REDACTED]
[REDACTED]	[REDACTED]
[REDACTED]	[REDACTED]
[REDACTED]	[REDACTED]
[REDACTED]	[REDACTED]
[REDACTED]	[REDACTED]
[REDACTED]	[REDACTED]

The [REDACTED] injection zones are at a starting depth from [REDACTED] ft. Their combined average porosity is [REDACTED] % with an average net reservoir thickness of [REDACTED] ft (Figure AOR-36).

[REDACTED]

The total porosity of the upper and lower confining zones is also based [REDACTED]

[REDACTED]

[REDACTED]



Figure AOR-37—The net-to-gross distribution generated from subzone 2D trend maps and hard data at the wells. Yellow regions represent sands and dark green regions are shales.

The porosity distribution in the geologic model was constructed using [REDACTED]

- I. [REDACTED]
 - [REDACTED]
 - [REDACTED]
 - [REDACTED]
- [REDACTED]
 - [REDACTED]
 - [REDACTED]
- [REDACTED]
 - [REDACTED]
 - [REDACTED]

This methodology resulted in



Figure AOR-38—Equivalent porosity relationship to net-to-gross ratio (NTG) for the base case (Phi_Eq_50_vs_NTG) porosity distribution used in the reservoir simulation

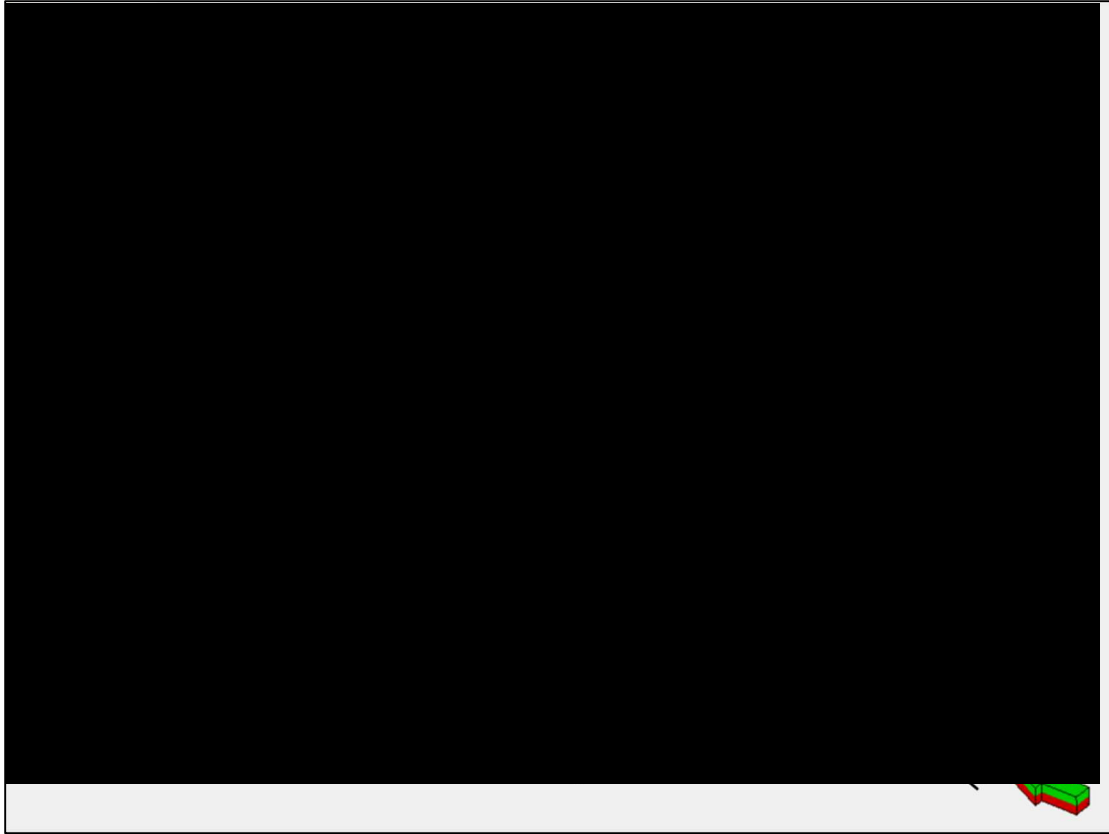


Figure AOR-39—A fence diagram showing 3D porosity distribution in the Pelican geological model

2.4.2 Permeability

For the pre-construction static modeling effort, the horizontal permeability for the injection zones was based on available core analysis data from 10 wells in the project site (Figure AOR-40). A core porosity-permeability transform was developed to estimate permeability over the intervals without core samples. Core permeability distribution suggests a range of [REDACTED] mD, which represents [REDACTED] values. Using this method, an average horizontal permeability of [REDACTED] mD is calculated for the [REDACTED] injection interval.

The upper and lower confining zone permeability was developed from the core porosity-permeability transform mentioned above, with log-derived effective porosity. The average horizontal permeability for the [REDACTED] zone is [REDACTED] mD and for the [REDACTED] zone is [REDACTED] mD. Although no core samples were taken from these zones, the vertical permeability of the actual shale interval is expected to be much lower because the vertical permeability of core plugs is generally lower than horizontal permeability and shale permeability is generally much lower than sandstone, limestone, and siltstone. An average horizontal permeability of [REDACTED] mD was also calculated for the secondary intrashales that divide the [REDACTED]. This indicates that even though the secondary intrashales may not be regionally extensive, they are relatively tight and tend to act as baffles to flow.

A single permeability transform was calculated from core data from 10 wells located inside the geomodel, as shown in Figure AOR-40. The derived transformation was then applied to each grid

[REDACTED] Figure AOR-41 shows the base case permeability distribution depicted as a fence diagram across the Petrel geological model. The other permeability realizations were modeled in the sensitivity analysis, as described in Section 3.2.1 Sensitivity to input parameters.



Figure AOR-40—Permeability-porosity transform fit to core data.



Figure AOR-41—Reservoir permeability distribution in the base case simulation model. Blue represents lower permeability, and red represents the highest permeability in the model.

2.5 Constitutive relationships and other rock properties

The project dynamic reservoir simulation followed a method developed by Ghomian et al. (2008), who had successfully matched the results of a [REDACTED] described in detail by Sakurai et al. (2005). Oxy adopted these established processes in our petrophysical evaluations, geological model construction, Equation-of-State (EOS) modeling for CO₂ properties and solubility, and the gas-water relative permeability model with higher trapped gas saturations during the imbibition process. Further, all simulation runs were executed using the GEM simulator, as used by Ghomian et al. (2008).

[REDACTED]

$$k_v = [(A * k_{sand})^{(NTG)}] * [(k_{shale})^{(1 - NTG)}] \dots\dots\dots \text{Equation 2}$$

A is a constant multiplier for sand permeability. The base case used values of A = [REDACTED] and k_{shale} = [REDACTED].

The water-gas relative permeability curves were constructed using a Corey model, with exponents previously reported by Ghomian (2008). These curves were also used in the simulation of the Frio CO₂ Pilot test. The following endpoint values and Corey exponents were used:

- $S_{wr} =$ [REDACTED]
- $S_{gc} =$ [REDACTED]
- $K_{rw} \text{ (at } [REDACTED] \% S_w) =$ [REDACTED]
- $K_{rg} \text{ (at } S_{wr}) =$ [REDACTED]
- $N_w =$ [REDACTED]
- $N_g =$ [REDACTED]

During the imbibition cycle (water displacing gas), the gas is trapped at S_{gt} or trapped gas saturation. S_{gt} values depend on the maximum gas saturation, S_{gh} , that a grid block has experienced. The base case maximum trapped gas saturation is specified as $S_{gt} =$ [REDACTED]. All dynamic simulation runs included [REDACTED]

2.6 Boundary conditions

No-flow boundary conditions were applied to the upper boundary ([REDACTED]) and lower boundary ([REDACTED]) of the model, with the assumption that the reservoir and caprocks are continuous throughout the region. The aquifer extent at the horizontal boundaries of the GEM simulation was [REDACTED]

Figure AOR-42 shows a high probability of thick [REDACTED] over the entire Gulf Coast region though there is some uncertainty about good hydraulic connectivity over such a large distance. To quantify its impact on AOR predictions, [REDACTED]

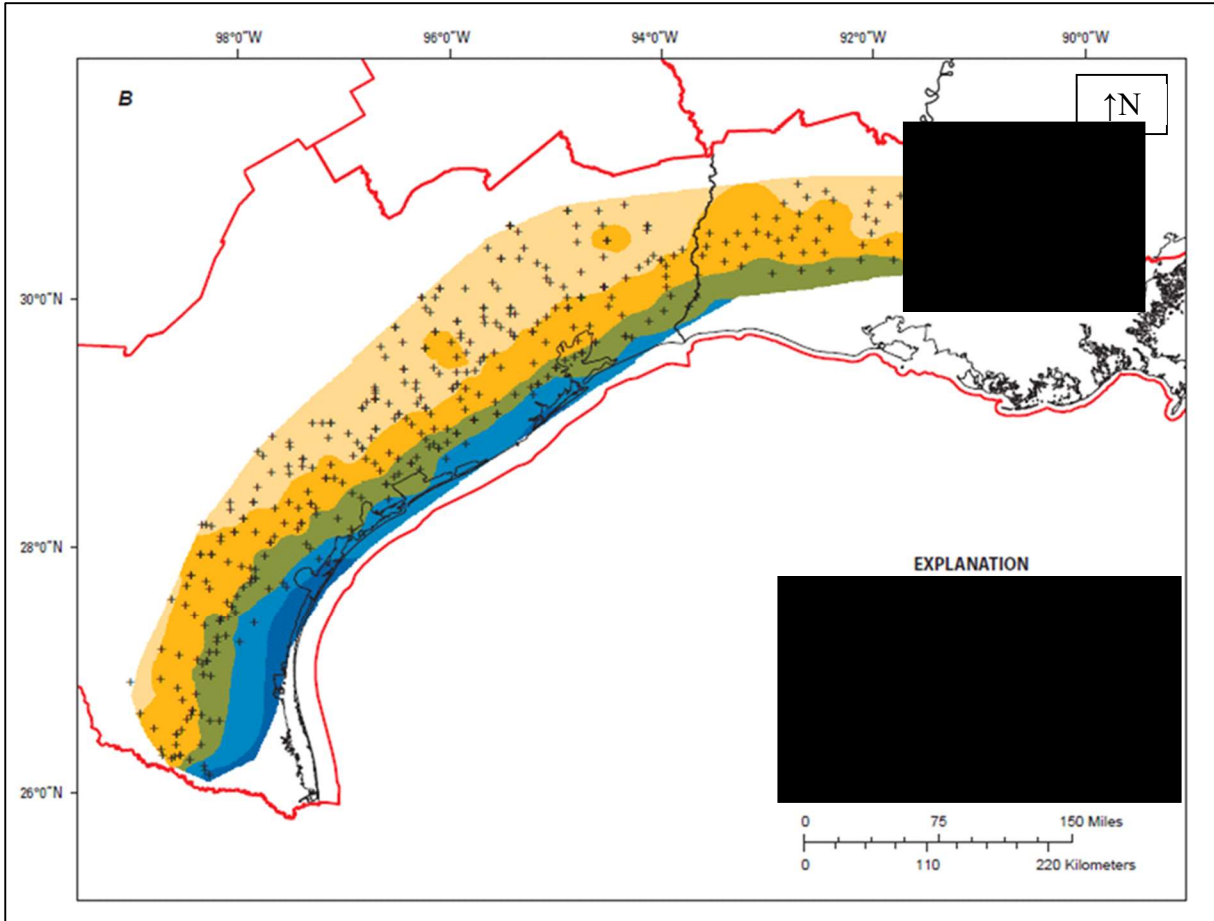


Figure AOR-42—A map showing [REDACTED] thickness in the Gulf Coast area and edge volumes added to the dynamic simulation model (Swanson, 2013)

2.7 Initial conditions

Initial conditions for the model are given in Table AOR-5.

Table AOR-5—Initial Conditions

Parameter	Value or Range	Units	Corresponding Elevation (ft MSL)	Data Source
[REDACTED]	[REDACTED]	[REDACTED]	[REDACTED]	[REDACTED]
[REDACTED]	[REDACTED]	[REDACTED]	[REDACTED]	[REDACTED]
[REDACTED]	[REDACTED]	[REDACTED]	[REDACTED]	[REDACTED]
[REDACTED]	[REDACTED]	[REDACTED]	[REDACTED]	[REDACTED]

In this study, the Frio pressure at [REDACTED] ft was calculated as [REDACTED] psia using a regional hydrostatic pressure gradient of [REDACTED] psi/ft. For the modeled pressure gradient within the injection zone, a water density of [REDACTED] lb/ft³ (for [REDACTED] ppm TDS brine) was specified. The formation salinity

of [REDACTED] ppm TDS was determined from a produced water analysis report from a single well near the project area, the [REDACTED], shown as the Water Chemistry Data Well on the map in Figure AOR-43. A thorough search through all available well data resulted in one reliable data point within a 10-mile radius of well CCS-1 that pertained to the injection interval of interest. Site-specific water samples from the Pelican MLR 004 well were obtained during well completion, but analyses were not received until after all the reservoir simulation modeling was complete. The samples from the Pelican MLR 004 well have an average calculated TDS of [REDACTED] ppm, which is consistent with the salinity used in modeling. Details of the fluid sampling procedures and analysis are included in Appendix C: Site-Specific Data and Procedures.

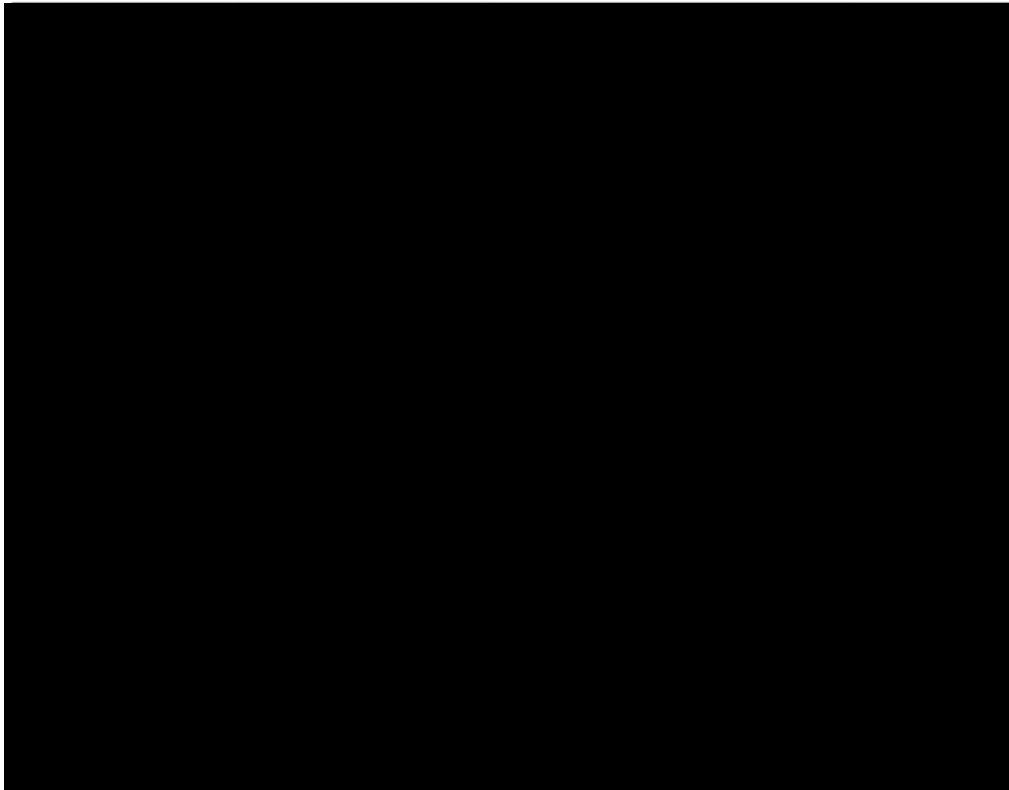


Figure AOR-43—Location of the [REDACTED] in relation to the Pelican project area. This well provided produced water for chemical analysis from a depth interval of [REDACTED] ft.

The reservoir temperature was initialized using a linear temperature gradient of 23°C/km, representative of the regional subsurface, with reference temperatures of 57.8°C/136°F at [REDACTED] ft, and 79°C/174.2°F at [REDACTED] ft (Nicholson, 2012).



[REDACTED]

[REDACTED]

[REDACTED]

[REDACTED]

[REDACTED]

[REDACTED]

[REDACTED]

[REDACTED]

[REDACTED]

Dissolution of carbonate minerals can occur at temperatures above 120°C/248°F and with increasing acidity and salinity/TDS (total dissolved solids), thereby augmenting porosity and permeability. These same minerals can reprecipitate upon a decrease in temperature below 120°C/248°F (Smith and Ehrenberg, 1989). The reservoir temperature is [REDACTED]. In the presence of clay, kaolinites, and smectite can reprecipitate in the pore throats, decreasing porosity and permeability while increasing pressure. Due to the high porosity and permeability of the injection zone, neither mineral dissolution nor precipitation is expected to result in any performance change.

2.8 Operational information

[REDACTED]

[REDACTED]

Details on the injection operation are presented in Table AOR-6.

Table AOR-6—Operating Details

Operating Information	Injection Well CCS 1	Injection Well CCS 2
[REDACTED]	[REDACTED]	[REDACTED]
[REDACTED]	[REDACTED]	[REDACTED]
[REDACTED]	[REDACTED]	[REDACTED]
[REDACTED]	[REDACTED]	[REDACTED]
[REDACTED]	[REDACTED]	[REDACTED]
[REDACTED]	[REDACTED]	[REDACTED]
[REDACTED]	[REDACTED]	[REDACTED]
[REDACTED]	[REDACTED]	[REDACTED]
[REDACTED]	[REDACTED]	[REDACTED]
[REDACTED]	[REDACTED]	[REDACTED]

*Represents Z coordinates and diameter in the model, not the final wellbore design

2.9 Fracture pressure and fracture gradient

Table AOR-7 summarizes data gathered during well completion and testing of the MLR 004 stratigraphic well. Six tests were performed, including two formation integrity tests (FIT), three step-rate-tests (SRT) and one leak-off test (LOT). Details of the testing procedures and results are included in Appendix C. The three SRTs performed in [REDACTED] did not indicate clear changes in pressure versus rate, so the formation was not fractured during the SRT. The values in the table indicate the ratio of maximum BHP reached (at the maximum rate) to the measured depth, so fracture gradients are higher than the tabulated values. During the LOT in the [REDACTED], a fracture was created and the fracture gradient is captured in the table.

Table AOR-7—Results of Step-Rate, Formation Integrity, and Leak-off Tests on Pelican MLR 004 Well

Zone Name	Test Interval (ft MD)	Test Method	Kh (mD-ft)	Skin	Pi (psia)	Fracture Gradient / Max Observed Gradient (psi/ft)	Max Inj. Rate (BWPD)	Comments
[REDACTED]	[REDACTED]	[REDACTED]	[REDACTED]	[REDACTED]	[REDACTED]	[REDACTED]	[REDACTED]	[REDACTED]
[REDACTED]	[REDACTED]	[REDACTED]	[REDACTED]	[REDACTED]	[REDACTED]	[REDACTED]	[REDACTED]	[REDACTED]
[REDACTED]	[REDACTED]	[REDACTED]	[REDACTED]	[REDACTED]	[REDACTED]	[REDACTED]	[REDACTED]	[REDACTED]
[REDACTED]	[REDACTED]	[REDACTED]	[REDACTED]	[REDACTED]	[REDACTED]	[REDACTED]	[REDACTED]	[REDACTED]
[REDACTED]	[REDACTED]	[REDACTED]	[REDACTED]	[REDACTED]	[REDACTED]	[REDACTED]	[REDACTED]	[REDACTED]
[REDACTED]	[REDACTED]	[REDACTED]	[REDACTED]	[REDACTED]	[REDACTED]	[REDACTED]	[REDACTED]	[REDACTED]



$$\mu = \tau / \sigma' n \dots\dots\dots \text{(Equation 3)}$$

Using the Mohr-Coulomb failure criterion, failure is defined as conditions where the ratio of shear stress to effective normal stress acts on an optimally orientated plane and exceeds the failure limit defined by the relationship:

$$\tau = \mu \sigma + S_o \dots\dots\dots \text{(Equation 4)}$$

where S_o is cohesion and is a function of friction and unconfined compressive strength (UCS):

$$UCS = 2S_o(\sqrt{\mu^2 + 1} + \mu) \dots\dots\dots \text{(Equation 5)}$$

Figure AOR-44 shows a graphical representation of the linear Mohr-Coulomb failure criterion. The state of stress is represented by the Mohr circle defined by the maximum (σ'_1) and minimum (σ'_3) effective principal stresses. Any plane orientation is defined along the boundary of the circle by an angle of 2β from σ'_1 to σ'_3 , where β is the angle between the σ'_1 and the normal plane. In Figure AOR-44, the red semicircle represents the original state of effective stress. In the case of CO₂ injection into the reservoir, pore pressure is estimated to increase while decreasing the magnitude of the effective principal stresses and moving the circle to the left on the x-axis. The failure limit shown is the sloped solid black line defined by Equation 4. The dashed line would represent the failure limit of a pre-existing fault with comparatively little friction. While the friction of faults is not zero, it is small compared to the friction required to initiate fracture in the matrix.

As pore pressure increases during injection, the Mohr circle moves to the left along the x-axis and the boundary of the circle eventually intersects the failure envelope. Under those conditions, any plane oriented along the Mohr circle that crosses or intersects the failure envelope will be subject to failure risk. The linear model presented below represents a simplified version of the Mohr-Coulomb failure criterion, as the failure envelope is not often linear and as pore pressure increases, the effective stress decreases, but the horizontal principal stress magnitude increases, making the

circle smaller. The result of the linear model is a conservative interpretation, which is appropriate in a scenario where large uncertainties exist in the stress model.

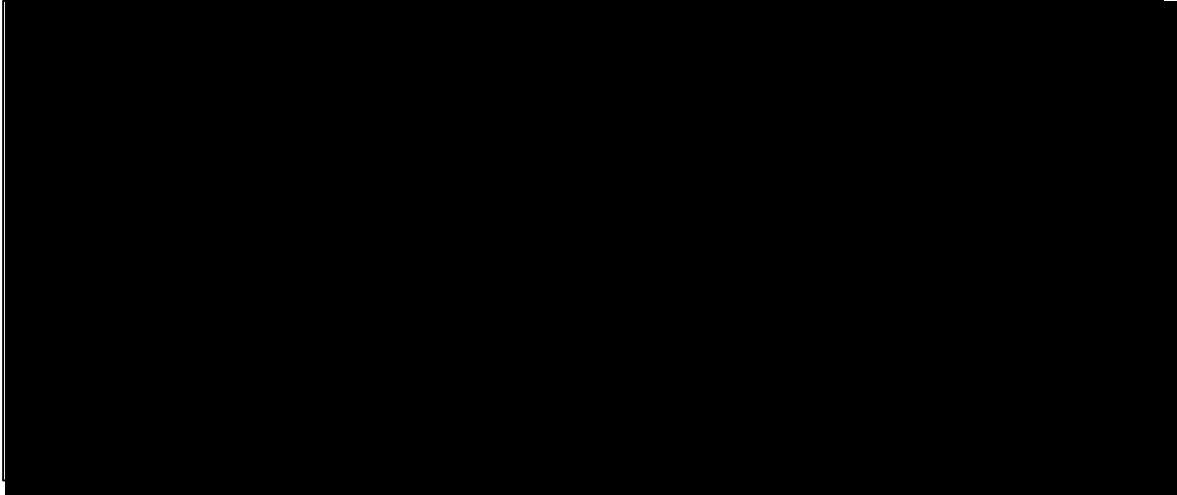


Figure AOR-44—Mohr-Coulomb Failure Criterion



$$P_p = \sigma_v - \sigma'_v \dots\dots\dots \text{(Equation 6)}$$



$$\sigma_3 = \frac{\nu}{1-\nu}(\sigma_v - \alpha P_p) + \alpha P_p \dots\dots\dots \text{(Equation 7)}$$

where:

σ_3 = least horizontal principal stress

ν = Poisson's ratio

σ_v = maximum principal stress

α = Biot's coefficient

P_p = pore pressure



Plan revision number: 0
Plan revision date: 07/31/23



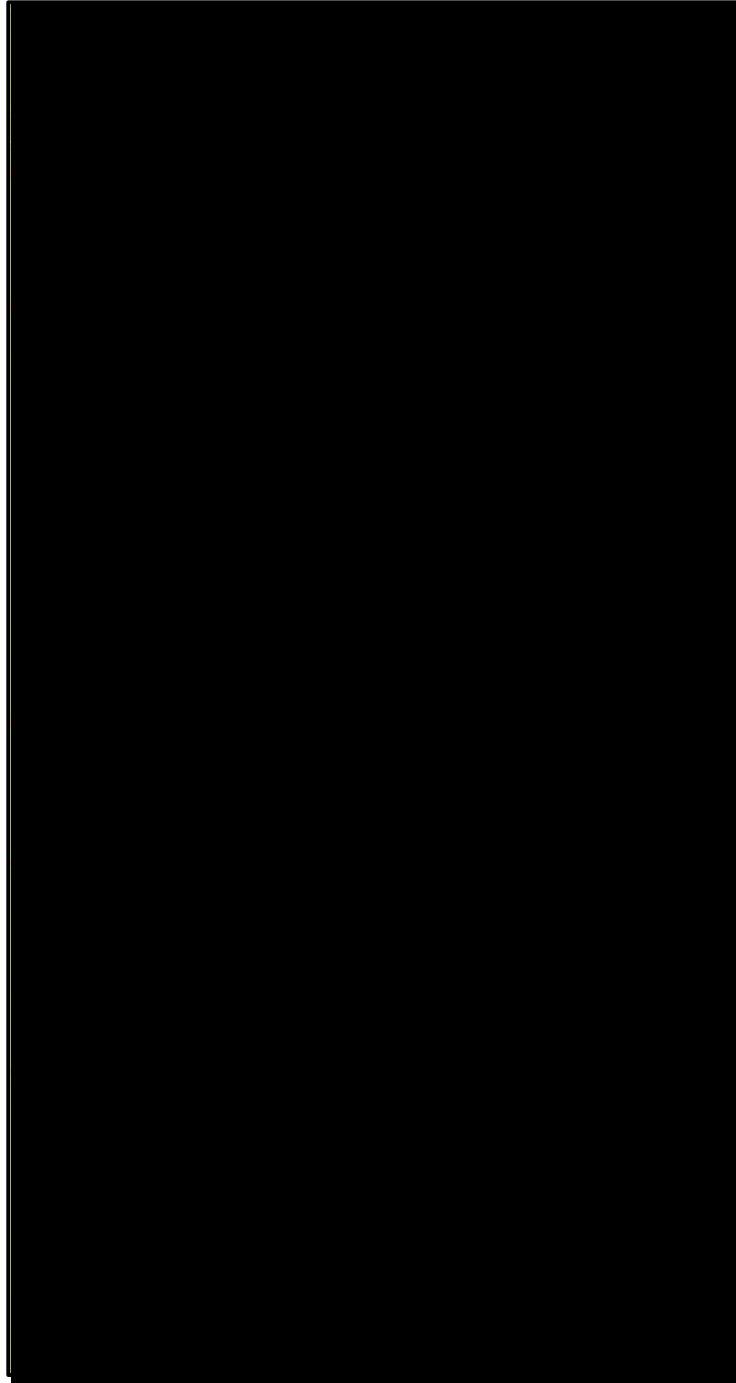


Figure AOR-45—Stress model (middle track) for the Pelican MLR 004 well. The black trend line represents overburden stress, red curve represents S_{hmin} , green curve represents S_{Hmax} , and blue trend line represents hydrostatic pore pressure. The black squares represent the LOT and SRT interpreted closure pressures used to calibrate the minimum principal stress.

Critical stress analysis (CSA) includes the assessment of shear or tensile failure of the formation. Failure is the generalized term used for the generation of induced fractures at the borehole wall or in the formation away from the borehole wall and/or reactivation of existing faults or fractures in the formation. The magnitude of stresses (as described above) is a necessary input as well as the orientation of principal stresses and the orientation existing and potential faults or fractures. In addition to stress characterization, rock and fault/fracture properties are necessary such as compressive and tensile strength of the matrix formation, internal friction coefficients of the matrix and cohesion, and friction of fault and fracture surfaces.

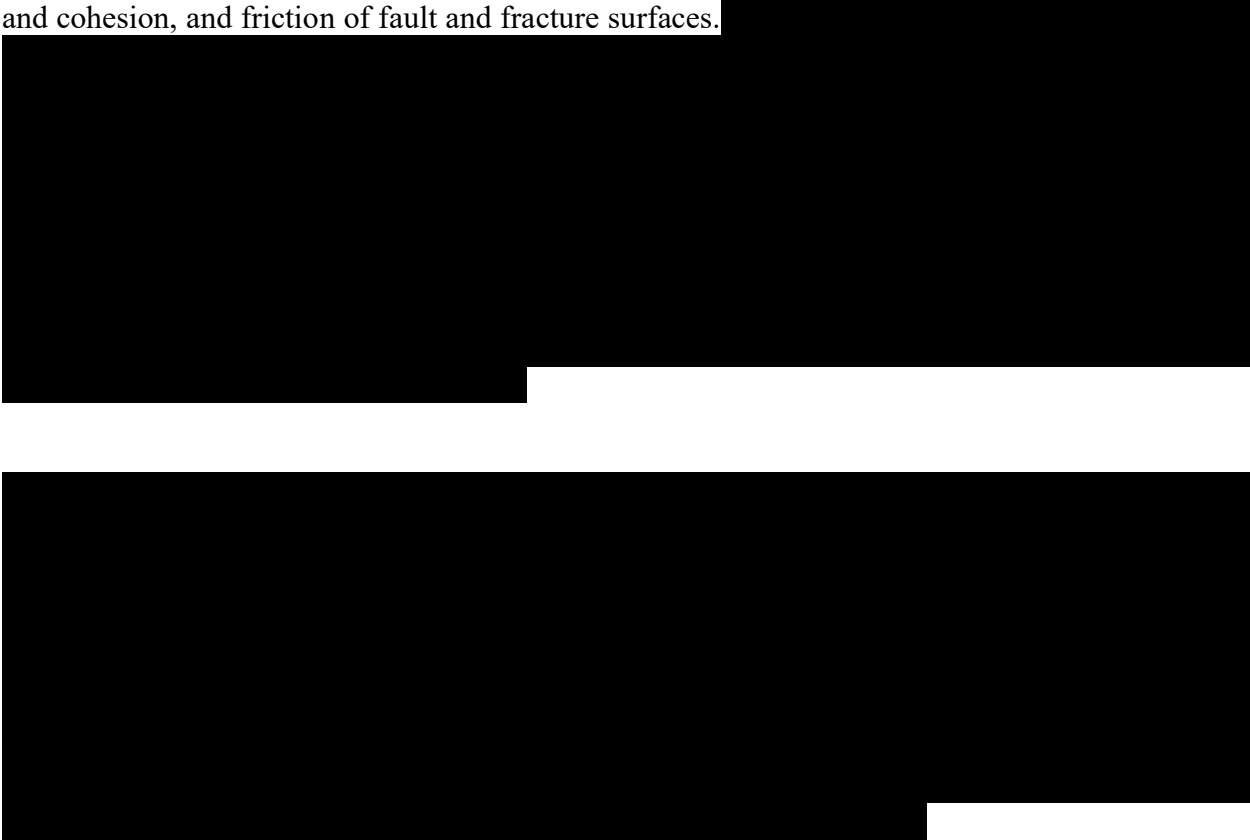




Figure AOR-46—Mohr circle depiction of the stress state with two failure limits shown: a failure limit with 0 psi cohesion (red line), a typical value to represent the strength of existing faults/fractures and a failure limit with a modest estimate of matrix shear strength and tensile strength (blue lines).

Figure AOR-46 shows the stress state in a Mohr circle graphical depiction. Two failure limits are shown in a similar fashion as Figure AOR-44. 1) the red limit represents a material (rock or fault/fracture) with zero cohesive or tensile strength. Typically, the failure limit is used to represent existing faults and fractures. 2) the blue limit represents a material with a modest cohesive strength (■■■ psi) and a reasonable tensile strength (■■■ psi). Since the material properties are unconstrained, we use these scenarios here to represent conservative estimates to show the highest risk conditions for injection.

Utilizing the red failure limit as the conservative case, the analysis indicates that the ■■■■■ is not currently in a critical state of failure. It also shows that a ■■■■ psi increase in pore-pressure

is required to move the Mohr circle into tensile stress (solid black arrow). In the event that optimally oriented unobserved faults or fractures exist, it would require [REDACTED] psi pressure increase to reactivate those structures in shear failure (dashed black arrow). Any consideration of tensile strength or cohesive shear strength of unobserved faults, fractures, or the matrix show that the pressures required to cause tensile or shear failure increase. The highest risk scenario is that unobserved, optimally oriented faults or fractures exist, and those experience a pore pressure increase of [REDACTED] psi from injection and are reactivated in shear failure.

Based on the above analysis and test results, a fracture gradient of [REDACTED] psi/ft is applied to determine the maximum injection pressure, as provided in Table AOR-8. The injection wells in the simulation model are rate limited and operate at a pressure that is equivalent to < [REDACTED] % of the maximum fracture gradient.

Table AOR-8—Fracture and Injection Pressure Details

Injection Pressure Details	Injection Well CCS 1	Injection Well CCS-2
Fracture gradient (psi/ft)	[REDACTED]	[REDACTED]
Maximum injection pressure (90% of the isotropic fracture pressure) (psia)	[REDACTED]	[REDACTED]
Elevation corresponding to maximum injection pressure (ft MSL)	[REDACTED]	[REDACTED]
Elevation at the top of the perforated interval (ft MSL)	[REDACTED]	[REDACTED]
Calculated maximum injection pressure at the top of the perforated interval (psi)	[REDACTED]	[REDACTED]

3.0 Computational Modeling Results

The dynamic simulations were carried out in [REDACTED]

3.1 Predictions of system behavior

The simulated well rates and pressures are shown in Figure AOR-49. Well rate was controlled at a constant value of [REDACTED] for each well. Wellhead pressures were calculated using a PROSPER-generated tubing table for [REDACTED]-in. tubing. The Pelican CCS 1 bottomhole pressure is reported at the reference gauge depth of [REDACTED] ft and reaches a maximum of [REDACTED] psi. The Pelican CCS 2 bottomhole pressure is reported at the reference gauge depth of [REDACTED] ft and

reaches a maximum of [REDACTED] psi. These pressures are more than [REDACTED] psi below the operational constraint of 90% of fracture pressure at the corresponding depth. The wellhead pressure for the Pelican CCS 1 well is predicted to be a maximum of [REDACTED] psi and the wellhead pressure for the Pelican CCS 2 well is predicted to be a maximum of [REDACTED] psi.

The resulting maximum extents of the CO₂ plume and the pressure front are discussed in Section 4.0 Area of Review (AOR). The movement of the CO₂ plume with time are shown in Section 5.3 Corrective action evaluation and in the Post-Injection Site Care and Post-Injection Site Closure Plan of this permit.

The geologic model and corresponding simulation model will be updated with site-specific petrophysical core data (permeability, porosity, and facies distribution) and transport data (relative permeability and capillary pressure) once the laboratory tests on well MLR 004 cores are completed. Injectivity tests performed on the Pelican MLR 004 well (Table AOR-8) confirmed the injectivity rate predicted by the models.



Figure AOR-47-47—Simulated well gas injection rates and corresponding wellhead and bottomhole pressures.

Figure AOR-4848 illustrates the predicted areal coverage of the CO₂ plume after [REDACTED] MT CO₂ injection into the two CCS wells. The blue outline in the figure represents the East area of field development and is used to determine the retention of CO₂ within the leased acreage.



Figure AOR-4848—Map of the extent of the CO₂ plume after [REDACTED] MT CO₂ injection. The blue outline represents the East area of field development.

3.2 Model calibration and validation

3.2.1 Sensitivity to input parameters

To test the sensitivity of the dynamic modeling results, the following subsurface uncertainties were explored: variogram anisotropy ranges, NTG relationship to porosity, sand horizontal permeability, vertical-to-horizontal permeability ratio (K_v/K_h), relative permeability curves, trapped gas saturations (S_{gt}), fault transmissibility, reservoir temperature and initial pressure, and size of the boundary aquifers. In addition, impacts of operational parameters such as injector well location and completion strategy were explored.

Table AOR-9 summarizes the possible ranges of the subsurface uncertainties and operation parameters. The base case inputs are indicated in the left column. Simulations were completed by varying the parameters one at a time, then, the results were analyzed to determine the impact on reservoir pressure change due to injection and CO₂ retention. In order to constrain the evaluation of the results with the development area, a boundary was defined for the East development area of the field (blue polygon in Figure AOR-4848).

Table AOR-9—Sensitivity Cases Simulated

Parameter	Base Value	Sensitivity Values		
[REDACTED]	[REDACTED]	[REDACTED]	[REDACTED]	[REDACTED]
[REDACTED]	[REDACTED]	[REDACTED]	[REDACTED]	[REDACTED]
[REDACTED]	[REDACTED]	[REDACTED]	[REDACTED]	[REDACTED]
[REDACTED]	[REDACTED]	[REDACTED]	[REDACTED]	[REDACTED]
[REDACTED]	[REDACTED]	[REDACTED]	[REDACTED]	[REDACTED]
[REDACTED]	[REDACTED]	[REDACTED]	[REDACTED]	[REDACTED]
[REDACTED]	[REDACTED]	[REDACTED]	[REDACTED]	[REDACTED]
[REDACTED]	[REDACTED]	[REDACTED]	[REDACTED]	[REDACTED]
[REDACTED]	[REDACTED]	[REDACTED]	[REDACTED]	[REDACTED]
[REDACTED]	[REDACTED]	[REDACTED]	[REDACTED]	[REDACTED]
[REDACTED]	[REDACTED]	[REDACTED]	[REDACTED]	[REDACTED]
[REDACTED]	[REDACTED]	[REDACTED]	[REDACTED]	[REDACTED]
[REDACTED]	[REDACTED]	[REDACTED]	[REDACTED]	[REDACTED]
[REDACTED]	[REDACTED]	[REDACTED]	[REDACTED]	[REDACTED]

Figure AOR-49 and Figure AOR-49 show the sensitivity of forecasted reservoir pressure to the various reservoir parameters. The pore-volume weighted average reservoir pressure within the East area polygon as a function of time. The maximum pressure occurs at the end of [REDACTED] MT of CO₂ injected. The highest change in the average reservoir pressure occurs in cases of low horizontal permeability and low edge pore volume, but the maximum increase in these cases is only about [REDACTED] psia. At the local level, the highest pore pressure increase occurs near the injection wells, but it is less than [REDACTED] psia. A tornado chart of the maximum average reservoir pressure in comparison to base case is shown in Figure AOR-49. The reservoir pressure is most sensitive to the horizontal sand permeability and the size of the boundary aquifer. The pressure increase is moderately sensitive to K_v/K_h , reservoir temperature, and relative permeability. The pressure increase is not sensitive to the fault's transmissibility multiplier, injection period of Stage 1, Stage 2 completion interval, injector well location, or the trapped gas saturation S_{gt} .

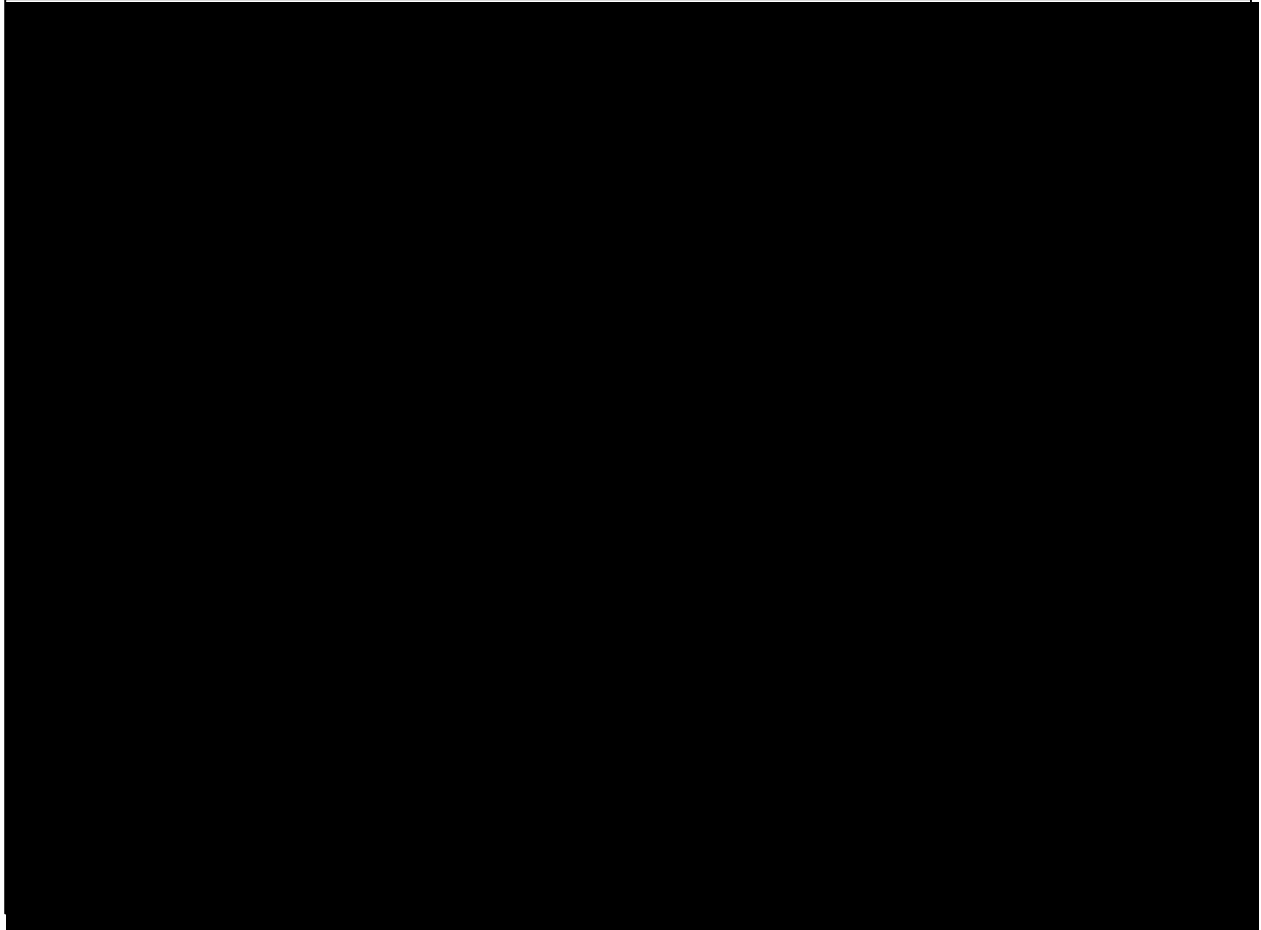


Figure AOR-49—Forecasted pore-volume weighted average reservoir pressure increase within the East area for all sensitivity simulations. The thick green line indicates the base case. Injection begins at time = 0.

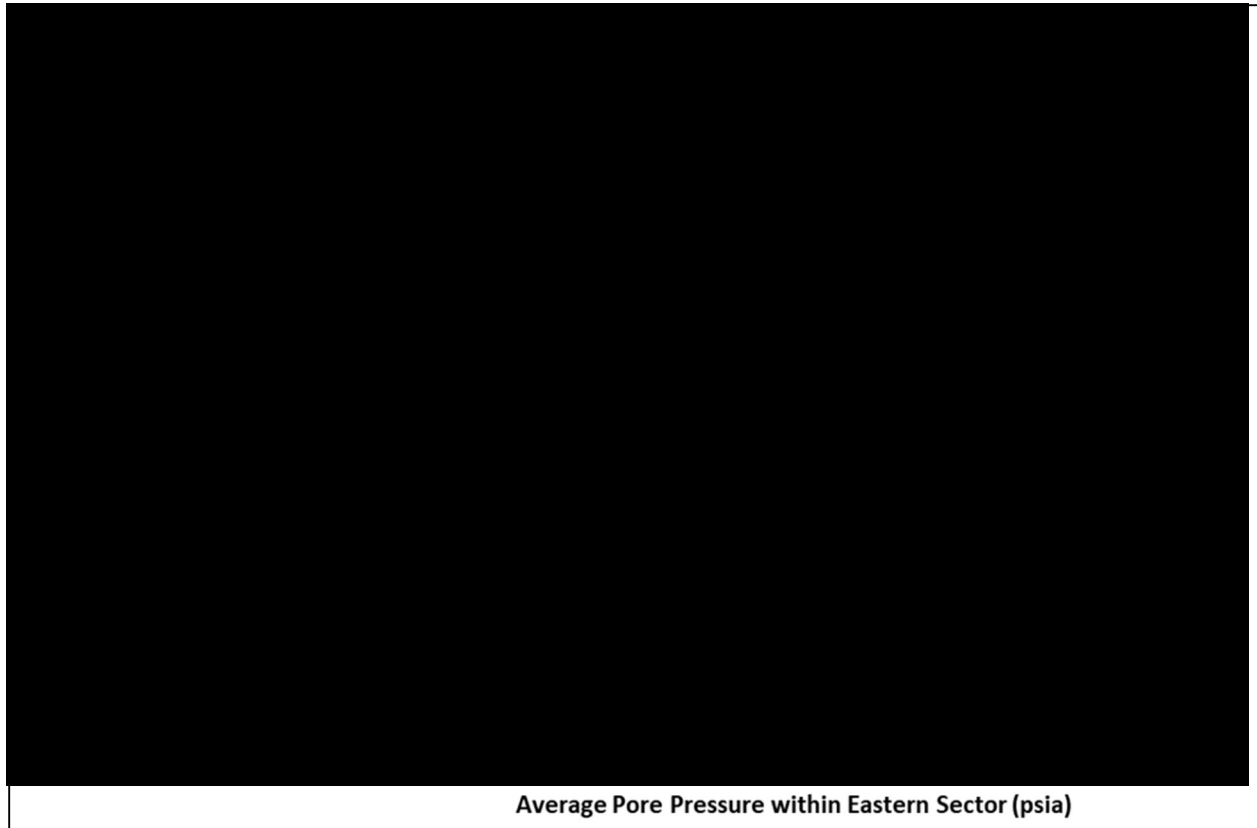


Figure AOR-49—Sensitivities of pore-volume averaged reservoir pressure in the East area to various subsurface and operation input parameters after [REDACTED] MT CO₂ injection.

Figure AOR-50 shows the sensitivities of the CO₂ retention within the storage reservoir to various reservoir and operation input parameters. The storage reservoir for CO₂ retention is defined areally as within the East area boundary and vertically as below the [REDACTED]. The red dashed line in Figure AOR-50 represents the total CO₂ injected volume. The other lines represent the fraction of CO₂ retained versus time. In all cases, any loss of CO₂ outside of the defined area occurs laterally and not through the seal. After the injectors are shut in, the CO₂ may continue to migrate updip and some will travel outside the project area, thus decreasing the CO₂ retention. CO₂ retention is shown to be most sensitive to well location. The proposed CCS 1 location appears to be most attractive, supported by all four geological realizations. For most cases, the forecasted CO₂ retention after the 100-year shut-in period exceeds 99%. A tornado diagram summarizing the sensitivities of CO₂ retention at a time 100-years post injection to various parameters is shown in Figure AOR-51.

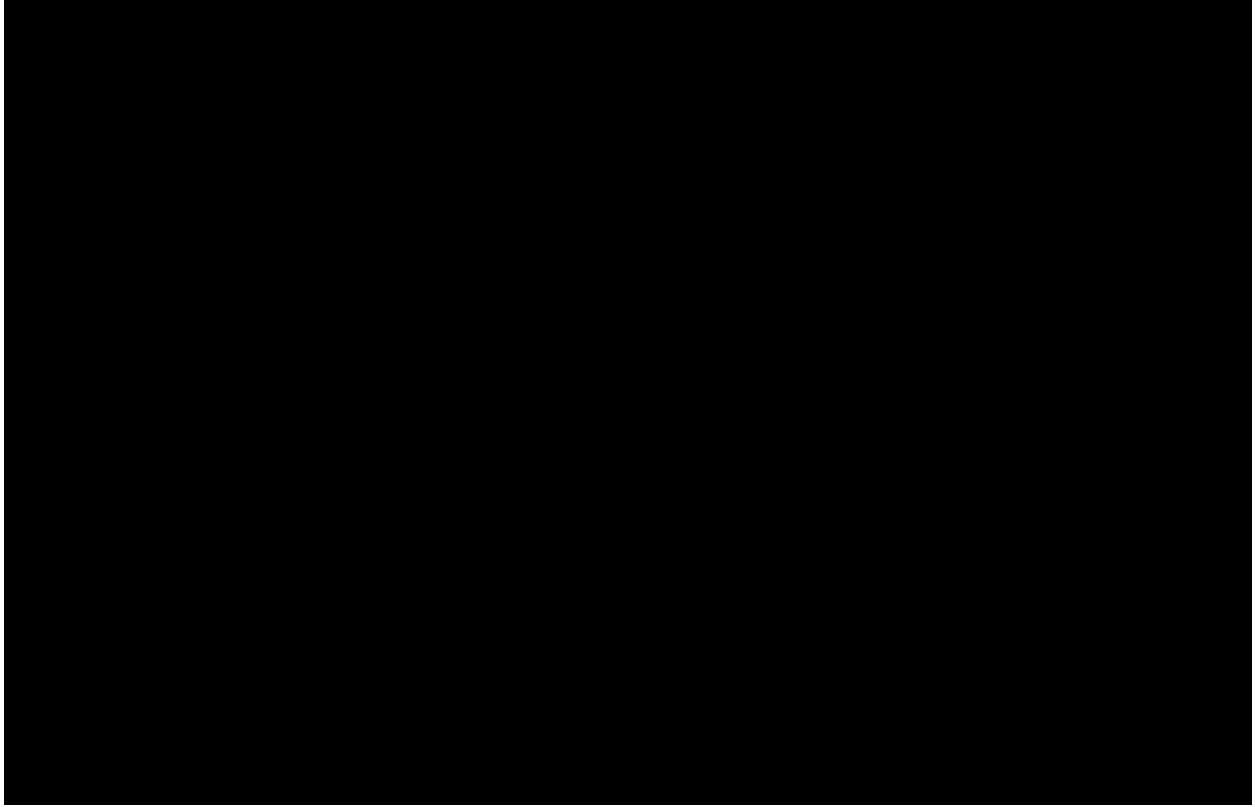


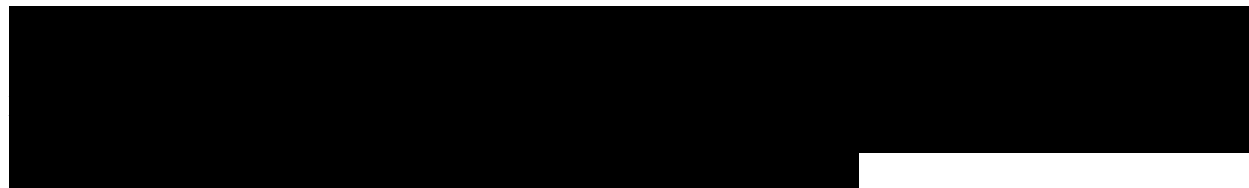
Figure AOR-50—Forecasted CO₂ injection and retention within the East area for all sensitivity simulations.
The black line indicates the base case. The red dashed line indicates the total CO₂ injection volume.



Figure AOR-51—Sensitivities of CO₂ retention in the East area to various subsurface and operation input parameters after the 100-year shut-in period. The total CO₂ injection volume prior to shut-in is [REDACTED] MT via two CCS injectors.

3.2.2 Simulation of reactive transport

Results showing the forecasted storage mechanisms of injection CO₂ in the reservoir are shown in Figure AOR-52. The results indicate that a negligible fraction of CO₂ injected into the Frio formation is stored in the carbonate minerals, whereas the majority of injected CO₂ is stored as tiny bubbles of supercritical CO₂ trapped in the pores and by dissolution into the saline brine. After ceasing injection, a large fraction of CO₂ continues to be trapped in pores as supercritical CO₂ by encroaching brine from edge aquifers.



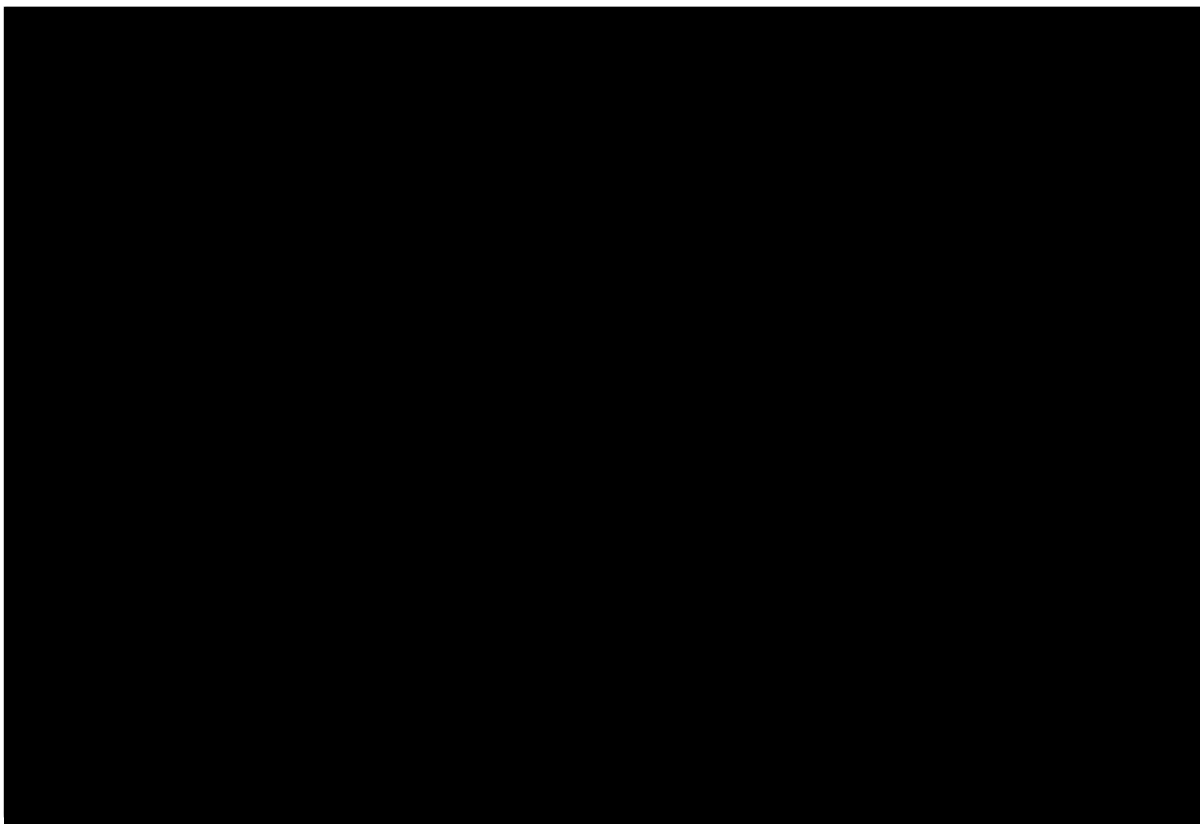


Figure AOR-52—Forecasted CO₂ storage mechanisms within the subsurface as a function of time

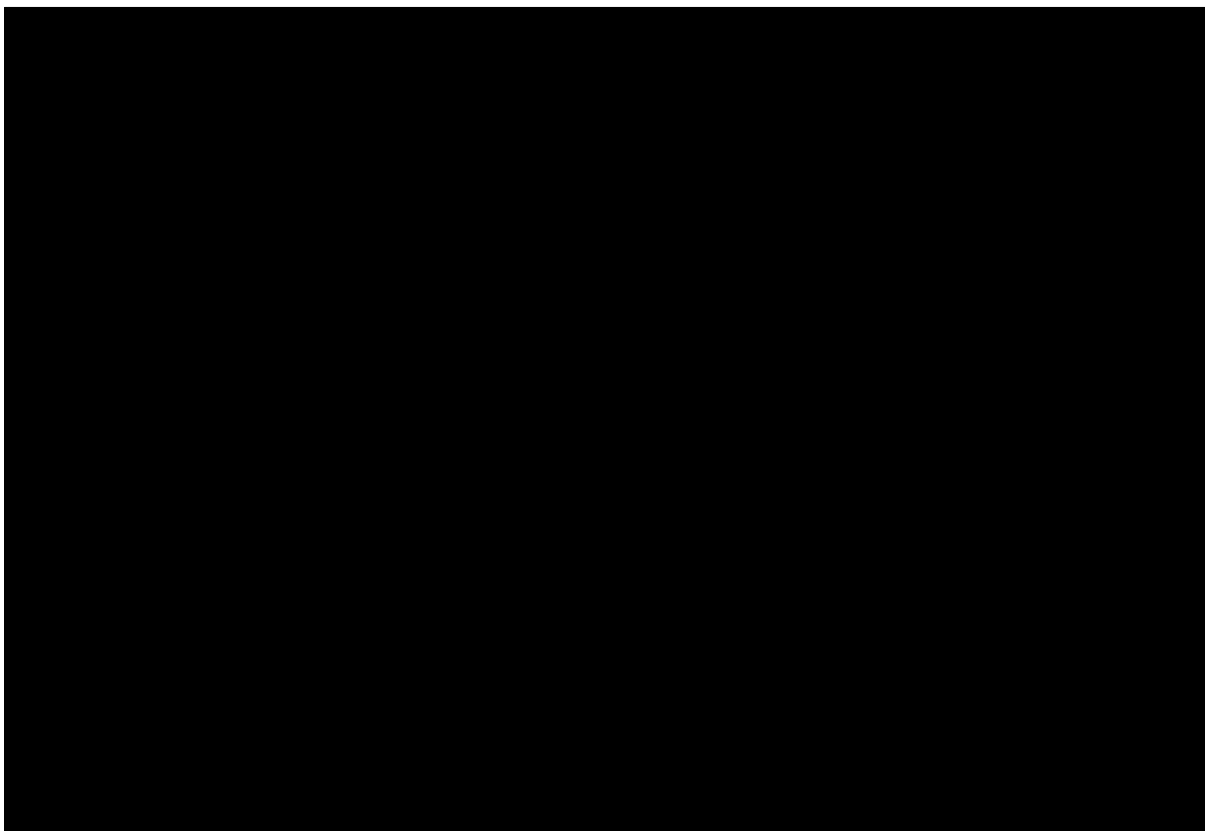


Figure AOR-53—Forecasted CO₂ reactive transport modeling results indicate mineral dissolution (-) and precipitation (+) over 400 years. Mineral reactions had little impact on predicted CO₂ injectivity.

4.0 Area of Review (AOR)

4.1 Critical pressure calculations

To delineate the critical pressure front, it is necessary to calculate the minimum pressure differential that can reverse flow direction between the deepest USDW and the injection zone, thereby causing fluid flow from the injection zone into the USDW formation matrix. To cause reverse flow to the USDW, the pore pressure increase would need to be high enough to overcome the hydraulic head of the fluid in a hypothetical wellbore and enter the USDW.

The technical team calculated the critical pressure threshold, ΔP_c , using Method 2 provided in the EPA May 2013 Program Class VI Well Area of Review and Corrective Action Evaluation Guidance (EPA, 2013). This method estimates a pressure differential that would displace fluid initially present in a hypothetical borehole into the deepest USDW and is based on two assumptions: 1) hydrostatic conditions, and 2) initially linearly varying densities in the borehole and constant density once the injection zone fluid is lifted to the top of the borehole. Method 2 applies only to hydrostatic cases, which is the assumed initial pressure regime at the Pelican CCS 1 well. The hydrostatic assumption and the critical pressure calculation will be re-evaluated once well test data from Pelican MLR 004 have been interpreted.

Using Method 2 developed and published by Nicot et al. (2008), the critical pressure threshold (ΔP_c) in the injection zone is given by Equation 9:

$$\Delta P_c = \frac{1}{2} * g * \xi * (z_u - z_i)^2 \dots\dots\dots \text{(Equation 9)}$$

where:

$$\xi = \frac{\rho_i - \rho_u}{z_u - z_i} \dots\dots\dots \text{(Equation 10)}$$

The critical pressure differential based on an average injection zone depth of [REDACTED] ft TVD, the lowest USDW depth of [REDACTED] ft TVD, injection zone brine density of [REDACTED] lb/ft³, and the USDW freshwater density of [REDACTED] lb/ft³ was calculated to be [REDACTED] psi.

4.2 AOR delineation

4.2.1 Critical pressure front

The maximum differential pressure occurs at the maximum cumulative volume of CO₂ injection, as the wells are operating at a constant injection rate. In the model, this occurs 15 years after injection commences. The movement of the pressure front was evaluated at 5, 10, and 15 years after injection begins in order to find optimal locations for the in-zone monitoring wells. The forecasted pressure increase after [REDACTED] MT injected CO₂ is given in Figure AOR-54. As shown, a critical pressure front of [REDACTED] psi projected onto the 2D areal map results in an AOR that includes the entire model domain.

The magnitude of the area encompassing the pressure plume defined by the critical pressure method, combined with the existing number of wellbores and oil and gas fields along the Gulf Coast, results in an impractical number of wellbores to be evaluated and remediated.

An improved method to estimate the acceptable pressure increase within the injection zone that will not endanger USDWs is to use multiphase numerical modeling to quantify the brine leakage through a wellbore in the formation. This method, called risk-based AOR, has been implemented for the Pelican hub to define the area in which the pressure increase in the subsurface may damage the USDWs. Risk-based AOR methods have been recognized in the literature as being a feasible alternative to the more conservative critical pressure calculation of the AOR (White et al., 2020; Burton-Kelly et al., 2021; Bacon et al., 2020; Oshini et al., 2020). A regulatory precedent has been established in that risk-based AOR methods have been utilized and approved in two Class VI permits approved by the state of North Dakota for Minnkota Power Cooperative, Inc.

<https://www.dmr.nd.gov/oilgas/GeoStorageofCO2.asp>

Appendix D: Risk-Based AOR presents the details of a risk-based AOR methodology applied to existing wellbores outside the CO₂ plume that may see a pressure increase above the critical pressure in the injection interval. The method employs a detailed simulation model to quantify brine leakage to the USDW through legacy wellbores for a wide range of injection-zone pore pressure increases, artificial-penetration eroded cement permeabilities, and reservoir parameters. Results indicate that any brine pushed out of the injection interval through legacy wellbores by the elevated pore pressure will backflow into the high-permeability sandstone reservoirs in the Lower Miocene instead of leaking, resulting in zero brine leakages into the USDW. As such, we propose that AOR delineation for this specific site may be based on the CO₂ plume extent only.

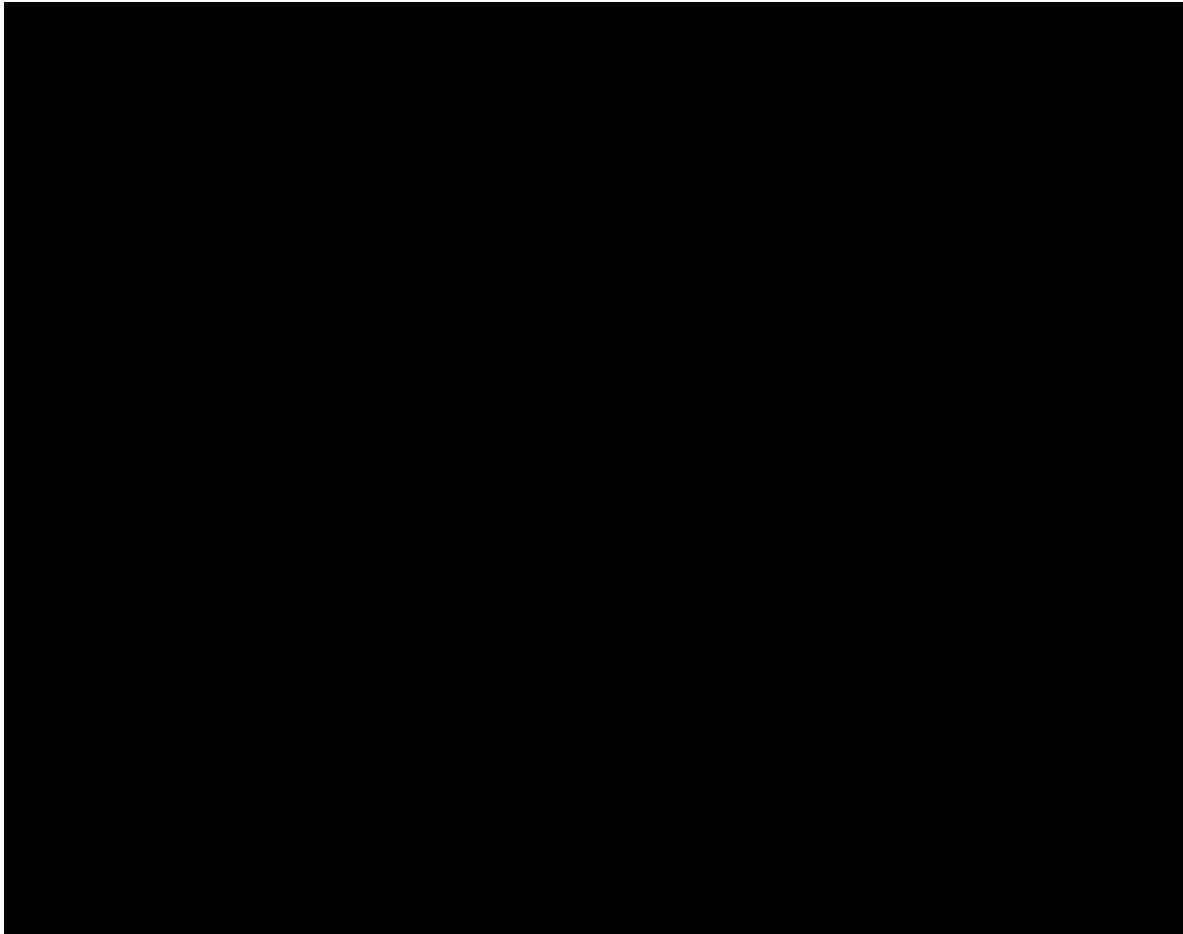


Figure AOR-54—Areal view of pore-pressure increase after a total of [REDACTED] MT of CO₂ injection for 15 years. Values displayed are pore-volume-weighted averages across the injection interval.

4.2.2 CO₂ plume extent

There is no specification in the Class VI rule as to what criteria should be used to define the CO₂ plume extent, other than it must be delineated using computational modeling. Most of the CO₂ is concentrated near the injection wellbore and the concentration declines with distance away from the wellbore. A seismic survey can resolve CO₂ saturation > [REDACTED]% in a geological subzone. Therefore, a pore-volume weighted geologic subzone saturation of [REDACTED]% has been applied as the cutoff value to define the CO₂ plume. This helps eliminate some of the uncertainty ([REDACTED] ft) introduced by the grid cell size and numerical dispersion on the CO₂ plume edges. We have found that the plume extent delineated by this method was in good agreement with method described by Zhang et al. (2015).

Figure AOR-55 displays the top view of the CO₂ plume extent at 5, 10, 15 years (during injection) and 50 and 100 years after injector shut-in. This plume extent is the result of superimposes of the maximum extent of the plume in each geologic subzone. Results suggested that CO₂ plume extents can be retained within the East area and the migration of CO₂ plume from 50 to 100 years is predicted to be minimal.



Figure AOR-55—CO₂ plume extents predicted by the simulation model: 5 years in very light blue, 10 years in dotted light blue, 15 years in heavy blue, 50 years after shut-in in dotted magenta, and 100 years after shut-in in heavy magenta.

Figure AOR-56 shows the simulated CO₂ saturations along a north-south cross-section through Pelican CCS 1 and CCS 2 wells 100 years after CO₂ injection had ceased. The figure displays a desirable uniform CO₂ profile within the injection zone, effectively utilizing all intervals in the leased pore space.

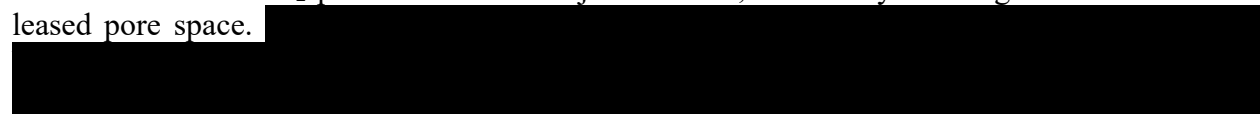




Figure AOR-56—South-north cross-section through the Pelican CCS 1 and CCS 2 wells showing simulated CO₂ saturation 100 years after ceasing CO₂ injection.

4.2.3 Combined area of review

As presented in Section 4.2.1 Critical pressure front, the final AOR is delineated based solely on the maximum CO₂ plume extent, as shown in Figure AOR-55. [REDACTED]

The predicted evolution of the CO₂ plume and pressure front relative to the monitoring locations are shown in the Testing and Monitoring Plan document and the Post-Injection Site Care (PISC) and Site Closure Plan document of this permit.

4.3 Fault leakage assessment

Figure AOR-55 shows the forecasted CO₂ plume extents at various times and the location of the closest mapped faults to the south, which are in an area greater than [REDACTED] away from the edge of the plume. Since the faults are in the down-dip direction, CO₂ migration through faults is extremely unlikely. However, the faults may see a slight increase in pressure due to the CO₂ injection.

Figure AOR-54 shows the pore pressure increase at the end of injection and the increase near the southern faults is approximately [REDACTED] psi. Near the end of Stage 1 injection, however, forecasted pore-pressure increases near the closest southern faults reaches [REDACTED] psia for a very brief period (see Figure AOR-57), but then quickly dropped to less than [REDACTED] psia after the well is re-completed uphole. The reactivation risks of faults in this CCS project are extremely low because: 1) the maximum [REDACTED] psi is still much less than the [REDACTED] psi pressure-increase limit calculated from geomechanical analyses, assuming zero cohesion (see Figure AOR-46) and 2) SRT results of Pelican MLR 004 suggested permeabilities in the [REDACTED] zones may be higher than modeled, which would reduce the pressure increase at the fault.

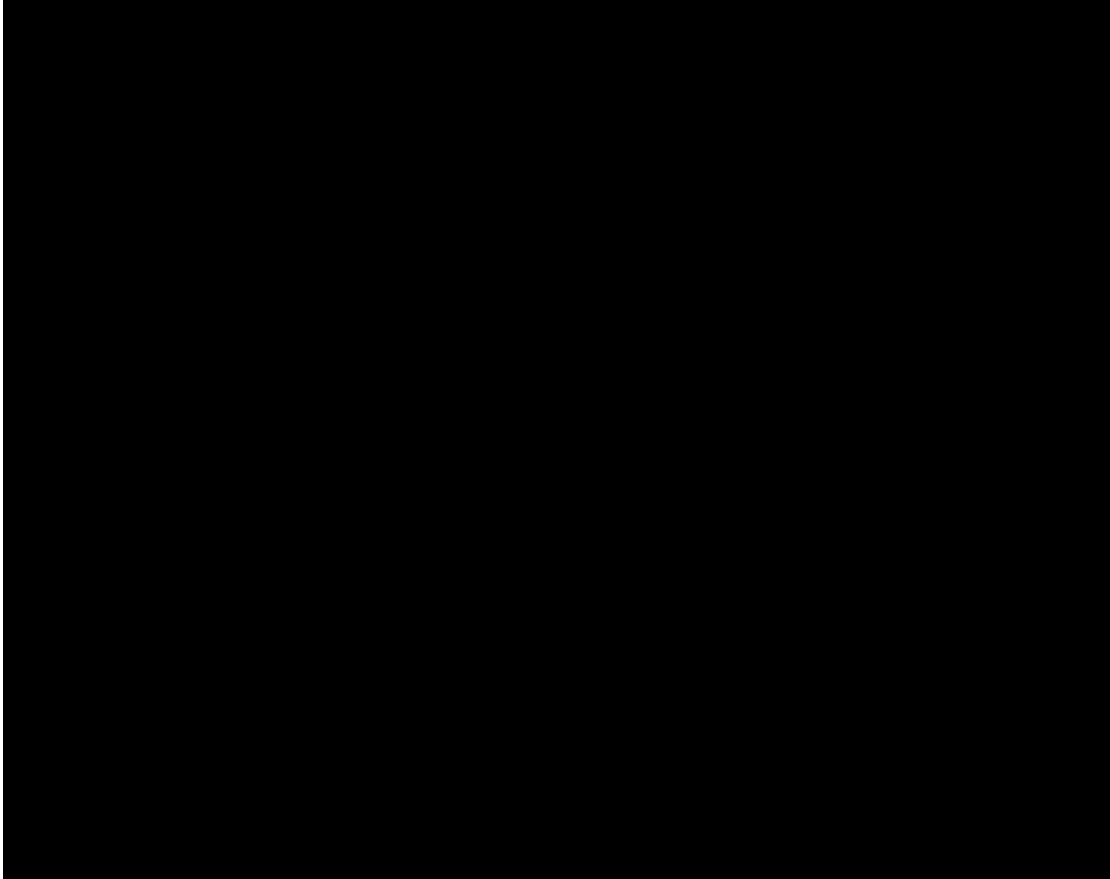


Figure AOR-578—Forecasted pore-pressure increase at the end of Stage 1 injection period. Values displayed are the maximum over the entire injection interval.

5.0 Corrective Action

5.1 Tabulation of wells within the AOR

The proposed AOR represents approximately [REDACTED] square miles of extension and includes [REDACTED] [REDACTED], according to the records obtained from LDNR. The locations of these wells are shown in Figure AOR-58. The area is dedicated mostly to the lumber industry and recreational activities. Oil and gas development is present in areas outside of the AOR; however, exploration activities in the proposed AOR have not proved to be economical.

[REDACTED]

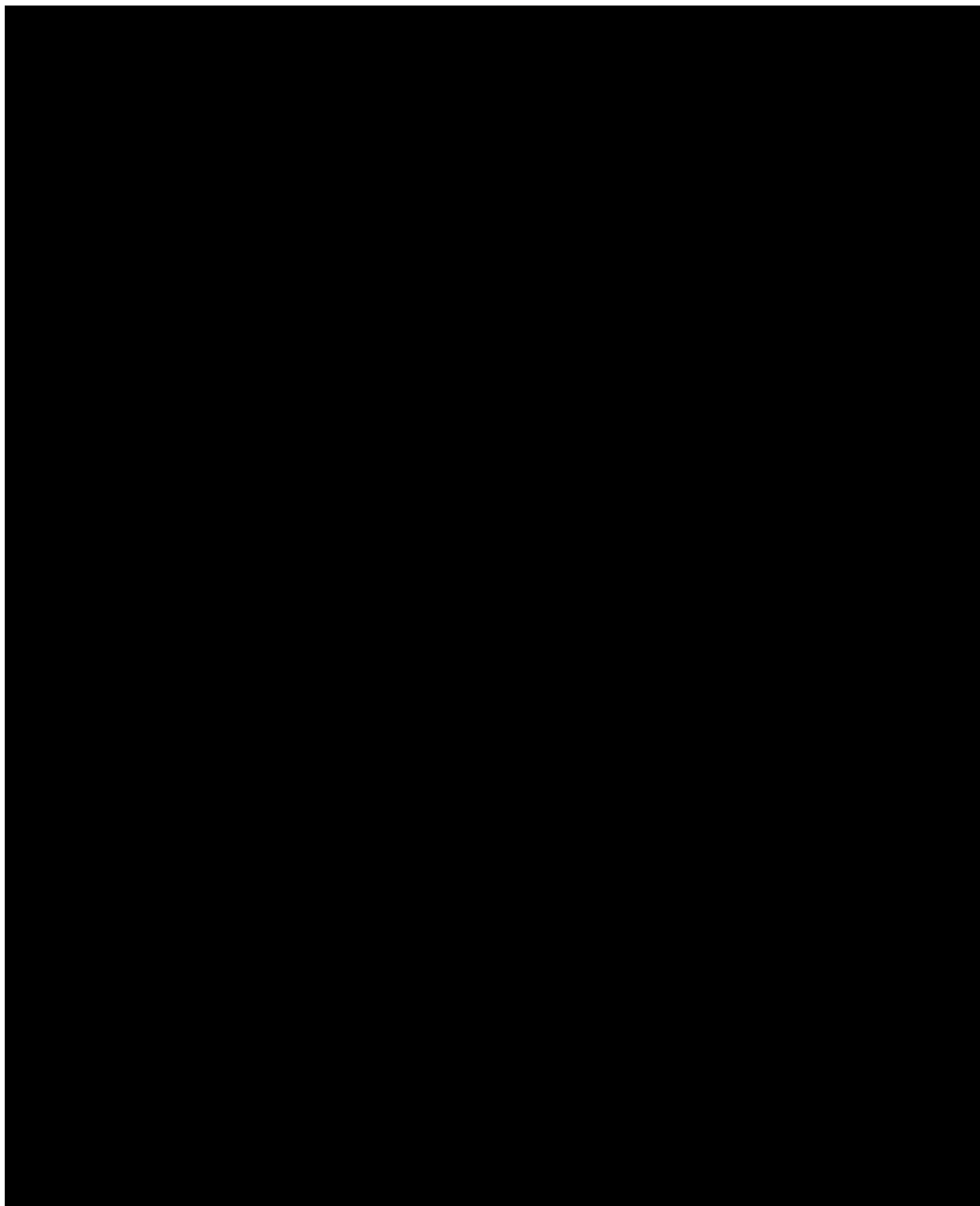


Figure AOR-58—Evaluation of legacy wells or existing penetrations in the AOR to identify corrective action plans needed.

5.1.1 Water wells within the AOR

The [REDACTED] water wells inside the AOR target the Chicot aquifer and are listed in Table AOR-10. These wells are mostly dedicated to domestic activities, as well as supply for the exploratory efforts of oil and gas companies. The measured depths range from [REDACTED]. Two of these wells are still active, according to the LDNR database. None of these three wells penetrate the confining or injection zone or require any corrective action.

Table AOR-10—Water Wells Within the Area of Review

Water Well Number	Well Depth, ft	Use Description	Well Status	Longitude	Latitude
[REDACTED]	[REDACTED]	[REDACTED]	[REDACTED]	[REDACTED]	[REDACTED]
[REDACTED]	[REDACTED]	[REDACTED]	[REDACTED]	[REDACTED]	[REDACTED]
[REDACTED]	[REDACTED]	[REDACTED]	[REDACTED]	[REDACTED]	[REDACTED]

5.1.2 Wells penetrating the confining zone within the AOR

The only oil and gas well identified within the Area of Review is the [REDACTED] well (Table AOR-11). [REDACTED]

Table AOR-11—Oil and Gas Wells Inside Area of Review

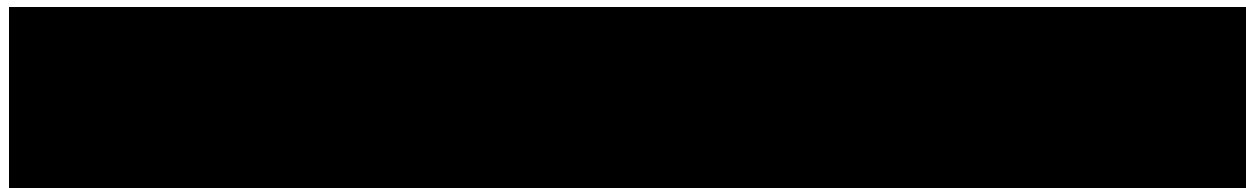
API Number	Status	Well Name	MD (ft)	Field Name	Spud Date	P&A Date	Latitude	Longitude
[REDACTED]	[REDACTED]	[REDACTED]	[REDACTED]	[REDACTED]	[REDACTED]	[REDACTED]	[REDACTED]	[REDACTED]

5.2 Plan for site access

The project wells and wells in the remediation plan are located inside the area negotiated for injection and a perpetual servitude was granted for the project Area of Review to allow for all project activities during pre-construction, construction, injection and operations, post-injection site care, and site closure. There are existing roads within the property and some improvements to the roads are required for drilling and maintenance equipment to access the wells.

5.3 Corrective action evaluation

Based on the delineated AOR, the only well that penetrates the confining and injection zone is the [REDACTED]. This well was evaluated in detail to identify potential leak paths and the corresponding remedial actions. Figure AOR-59 shows actual schematic of the well based on the LDNR database.



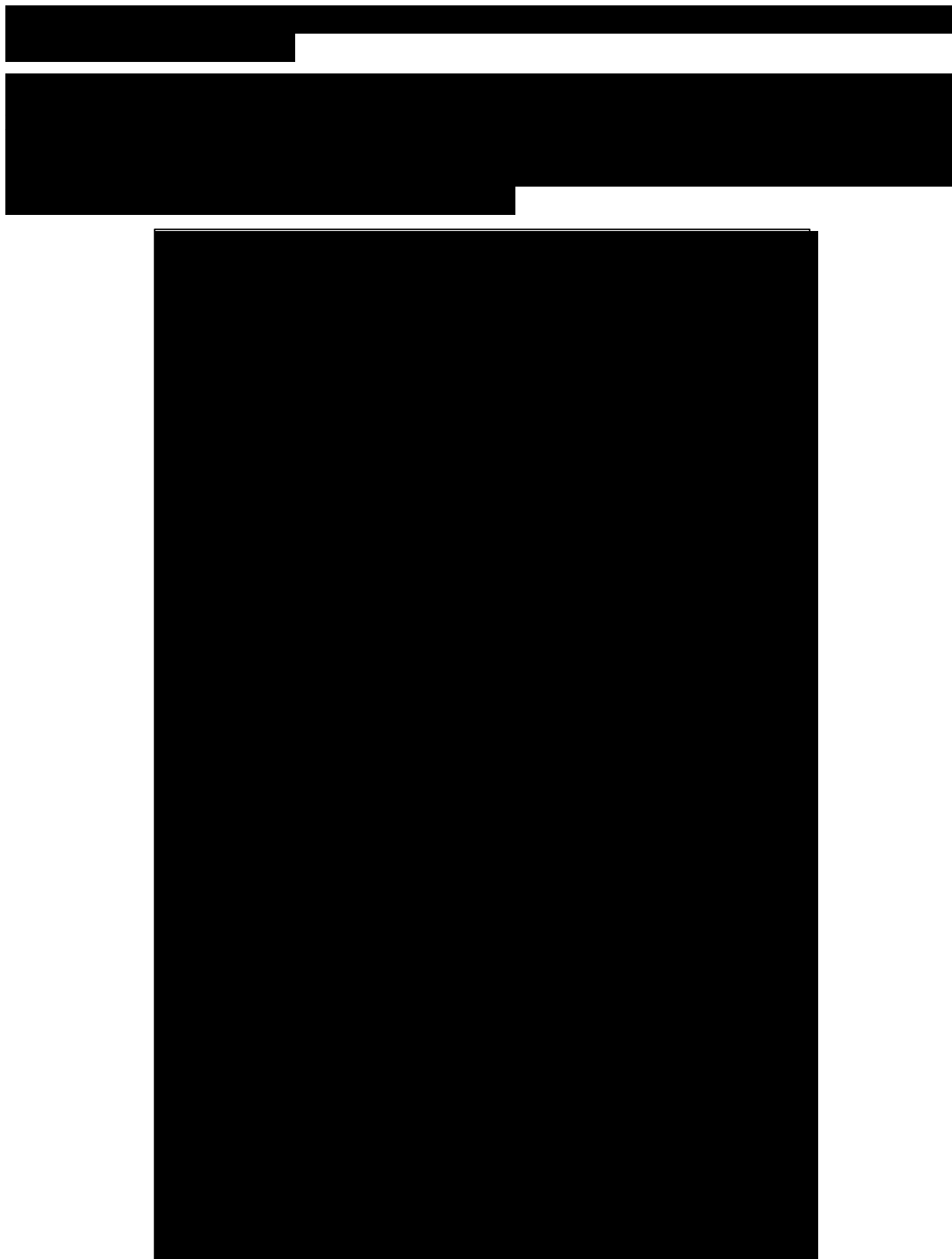


Figure AOR-59—Actual well schematic of



Figure AOR-601—Proposed remedial action for the [REDACTED]

5.4 Corrective action procedure

[REDACTED]

[REDACTED]

[REDACTED]

Plan revision date: 07/31/23

[illegible]

The procedures described above are subject to modification during execution as necessary to ensure a successful plugging operation. Any significant modifications due to unforeseen circumstances will be described in the plugging report.

6.0 Re-Evaluation Schedule and Criteria

6.1 AOR re-evaluation cycle

The permittee will re-evaluate the AOR every 5 years during the injection and post-injection phases. In addition, monitoring and operational data will be reviewed periodically by the permittee during the injection and post-injection phases.

Activities to be performed during re-evaluation include:

- Reviewing and analyzing available monitoring and operational data and comparing it to the dynamic simulation forecast to assess whether the predicted CO₂ plume migration is consistent with the actual data. This includes data from the Pelican CCS 1 injection well, monitoring and geophysical wells, other surrounding wells, and other sources. The monitoring activities to be conducted are described in the Testing and Monitoring Plan of this permit and in the PISC and Closure Plan.
- Specific steps of this review and analysis include:
 - Reviewing collected data on the position of the CO₂ plume and pressure changes in the reservoir as well as above the confining zones. These data will be collected from the in-zone monitoring wells and above confining zone monitoring wells as well as geophysical surveys, as described in the testing and monitoring plan.
 - Reviewing water chemistry of samples taken from the above confining zone (ACZ) monitoring wells and verifying there is no evidence of carbon dioxide or brines that represent an endangerment to any USDWs.
 - Reviewing operating data (e.g., injection rates and pressures) and verifying they are consistent with the inputs used in the most recent modeling effort.
 - Reviewing any geologic data acquired since the last modeling effort, e.g., additional site characterization performed and updates of petrophysical properties from core analysis, to identify whether any new data are materially different from the modeling inputs and assumptions.
- Comparing the results of computational modeling used for AOR delineation to the monitoring data collected. Monitoring data will be used to show that the computational model accurately represents the storage site and can be used as a proxy to determine the plume's properties and size. The degree of accuracy is demonstrated by comparing monitoring data with the model's predicted properties (i.e., plume location, rate of movement, and pressure decay). Statistical methods will be employed to correlate the data and confirm the model's ability to represent the storage site accurately.
- If the information reviewed is consistent with or unchanged from the most recent modeling assumptions or confirms the forecast of maximum extent of the CO₂ plume and pressure front, a report will be prepared to demonstrate that, based on the monitoring and operating

data, no re-evaluation of the AOR is needed. This report will include the data and results demonstrating that no changes are necessary.

- If material changes have occurred (e.g., behavior of the CO₂ plume and pressure front, operations, or site conditions) such that the actual plume or pressure front may extend beyond the modeled plume and pressure front, the AOR will be re-delineated. Steps to re-delineate the AOR include:
 - Revising the site conceptual model based on the new site characterization, operational, or monitoring data.
 - Calibrating and history-matching the model in order to minimize the differences between monitoring data and model simulations.
 - Performing the AOR delineation method as described in Section 4.2 AOR delineation of this AOR and Corrective Action Plan.
- Reviewing wells in any newly identified areas of the AOR and applying corrective action to deficient wells. Specific steps include:
 - Identifying any new wells within the AOR that penetrate the confining zone and provide a description of each well's type, construction, date drilled, location, depth, and record of plugging and/or completion.
 - Determining which abandoned wells in the newly delineated AOR are plugged in a manner that prevents movement of carbon dioxide or other fluids that may endanger USDWs.
 - Performing corrective action on all deficient wells in the AOR using methods designed to prevent the movement of fluid into or between USDWs, including the use of materials compatible with carbon dioxide.
- Preparing a report documenting the AOR re-evaluation process, data evaluated, any corrective actions deemed necessary, and status of corrective action or a schedule for any corrective actions to be performed. This report will be submitted to the EPA within one (1) year of the re-evaluation and will include maps that highlight similarities and differences with previous AOR delineations.
- Updating the AOR and Corrective Action Plan to reflect the revised AOR along with other related project plans, as needed.

6.2 Triggers for AOR re-evaluations prior to the next scheduled re-evaluation

Unscheduled re-evaluation of the AOR will be based on quantitative changes of the monitoring and operative parameters in injectors, monitoring wells, seismometer networks, and geophysical surveys that could indicate that the actual plume may extend beyond the area modeled. These changes might include:

- **Pressure:** Changes in pressure that are unexpected in timing or magnitude from those predicted by the model might trigger a review of the model and potentially new evaluation of the AOR.

- **RST Saturation:** Increases in CO₂ saturation in monitoring wells that indicate a breakthrough of CO₂ will trigger a new evaluation of the AOR.
- **Deep Groundwater Constituent Concentrations:** Unexpected changes in fluid constituent concentrations that indicate movement of CO₂ or brine into or above the confining zone might trigger a new evaluation of the AOR.
- **Exceeding Fracture Pressure Conditions:** Pressure in injection wells exceeding 90% of the geologic formation fracture pressure at the point of measurement.
- **Compromise in Injection Well Mechanical Integrity:** A significant change in annular pressure for the injection well or abnormal temperature readings in the fiber optic cable that indicates a loss of mechanical integrity or a failed mechanical integrity test (MIT) in an injector or monitoring wells.
- **Induced Seismicity Monitoring:** Seismic monitoring data that indicates reactivation of a fault or structures due to pressurization of the reservoir as a consequence of the CO₂ injection. The project will review the monitoring data to discard naturally occurring events not related to injection.

The permittee will discuss any such events with the UIC Program Director to determine if an AOR re-evaluation is required. If an unscheduled re-evaluation is triggered, the permittee will perform the steps described in Section 6.1 AOR re-evaluation cycle.

7.0 References

- Appriou, D., Huerta, N.J., Zhang, Z. et al. 2020. Evaluation of Containment and Geomechanical Risks at Integrated Mid-Content Stacked Carbon Storage Hub Sites: Pacific Northwest National Lab., Richland, WA, Report No. PLLN-30047.
- Bacon, D.H., Demirkanli, D I., and White, S.K. 2020. Probabilistic Risk-Based Area of Review (AOR) Determination for a Deep-Saline Carbon Storage Site. *International Journal of Greenhouse Gas Control*, **102**: 103153.
- Bebout, D.G., and Gutierrez, D.R. 1982. Regional Cross Sections Louisiana Gulf Coast: Western Part, Folio Series No. 5, 1-11.
- Blondes, M.S., Gans, K.D., Engle, M.A., et al. 2018. U.S. Geological Survey National Produced Waters Geochemical Database (ver. 2.3, January 2018): U.S. Geological Survey data release, <https://doi.org/10.5066/F7J964W8>.
- Burke, L.A., Kinney, S.A., Dubiel, R.F. and Pitman, J.K. 2013. Series of Five Maps Characterizing Geopressure Gradients Based on Mud Weight Measurements of Part of Southern Louisiana, State and Federal Waters: Map 1 – Depth of the 0.60 psi/ft Isopressure-Gradient Surface: America Association of Petroleum Geologists, Spatial Library GIS Open File, 5 pp., 5 maps.
- Burton-Kelly, M.E., Azzolina, N.A., Connorset, K.C. et al. 2021. Risk-Based Area of Review Estimation in Overpressured Reservoirs to Support Injection Well Storage Facility Permit

- Requirements for CO₂ Storage Projects. *Greenhouse Gases Science and Technology* **11**: (5) 887-906.
- Collins, D.A., Nghiem, L.X., Li, Y.-K. and Grabenstetter, J.E. 1992. An Efficient Approach to Adaptive-Implicit Compositional Simulation with an Equation of State. SPE-15133-PA. *SPE Res. Eng.*, **7**(2): 259-264.
- EPA. 2013. Geologic Sequestration of Carbon Dioxide – Underground Injection Control (UIC) Program Class VI Well Area of Review Evaluation and Corrective Action Guidance. U.S. Environmental Protection Agency 816-R-13-005. May 2013.
- Ewing, T.E. 1991. Structural Framework. In Salvador, A., ed., *The Geology of North America, The Gulf of Mexico Basin*. Geological Society of America, **J**: 31-52.
- Ewing, T.E. and Lopez, R.F. 1991. Principal Structural Features, Gulf of Mexico Basin. In Salvador, A., ed., *The Geology of North America, The Gulf of Mexico Basin*. Geological Society of America, **J**, plate 2, 1 sheet.
- Freifeld, B.M., and Trautz, R.C. 2006. Real-Time Quadrupole Mass Spectrometer Analysis of Gas in Borehole Fluid Samples Acquired Using the U-tube Sampling Methodology. *Geofluids*, **6**: 217-224.
- Galloway, W.E., Ganey-Curry, P.E., Li X., and Buffler, R.T. 2000. Cenozoic Depositional History of the Gulf of Mexico Basin. *AAPG Bull.* **84** (11): 1743-1774.
- Ghomian, Y. May 2008. Reservoir Simulation Studies for Coupled CO₂ Sequestration and Enhanced Oil Recovery. Doctoral Dissertation, University of Texas at Austin.
- Ghomian, Y., Pope, G.A., and Sepehrnoori, K. 2008. Reservoir Simulation of CO₂ Sequestration Pilot in Frio Brine Formation, USA Gulf Coast. *Energy*, **33** (7): 1055-1067.
- Gunter, W.D., Wiwehar, B., and Perkins, E.H. 1997. Aquifer Disposal of CO₂-Rich Greenhouse Gases: Extension of the Time Scale of Experiment for CO₂-Sequestering Reactions by Geochemical Modelling. *Mineralogy and Petrology*, **59** (1-2): 121-140.
- Harvey, A.H. 1996. Semiempirical Correlation for Henry's Constants over Large Temperature Ranges. *AIChE Journal*, **42** (5): 1491-1494.
- Hite, R.J. 2016. South Louisiana Enhanced Oil Recovery / Sequestration R&D Project Small Scale Field Tests of Geologic Reservoir Classes for Geological Storage. Final Scientific / Technical Report, DE-FE0006823, October 2016.
- Hovorka, S., Benson, S.M., Doughty, C. et al. 2006. Measuring Permanence of CO₂ Storage in Saline Formations: The Frio Experiment. *Environmental Geosciences*, **13** (2).
- Kestin, J., Khalifa, H.E., and Correia, R.J. 1981. Tables of the Dynamic and Kinematic Viscosity of Aqueous NaCl Solutions in the Temperature Range 20-150°C and the Pressure Range 0.1-35 MPa, *J. Phys. Chem. Ref. Data*, **10** (1) 71.
- Knauss, K.G., Johnson, J.W., Kharaka, Y.K. 2005. Preliminary Reactive Transport Modeling and Laboratory Experiments Conducted in Support of the Frio Pilot Test. Presented at the Fourth Annual Conference on Carbon Capture and Sequestration, Univ. of Texas. *CCCC Digital Publication Series #05-04m*.

- Lopez, J.A. 1995. Salt Tectonism of the United States Gulf Coast Basin: New Orleans Geological Society, map (2nd ed.), produced by AMOCO Production Company.
- Louisiana Geological Survey, U.S. Geological Survey, Department of the Interior, 2002, Ville Platte 30 x 60 Minute Geologic Quadrangle, <https://www.lsu.edu/lgs/maps/100k-Geology/Ville-Platte.pdf>
- Mason, S. 2010-2012 Jasper Equivalent Aquifer Summary Report, Louisiana Department of Environmental Quality, 29 pp.
- Martin, R.G. 1980. Distribution of Salt Structures, Gulf of Mexico: U.S. Geological Survey Miscellaneous Field Studies Map MF-1213, 2 sheets.
- MCCulloh, Richard P., Paul V. Henrich. 2012. Surface faults of the south Louisiana growth-fault province. The Geological Society of America Special Paper 493.
- Nghiem, L.X., and Li, Y.-K. 1989. Phase-Equilibrium Calculations for Reservoir Engineering and Compositional Simulation. Presented at the Second International Forum on Reservoir Simulation, Alpbach, Austria, September 4-8, 1989.
- Nghiem, L., Sammon, P.H., Grabenstetter, J., and Ohkuma, H. 2004. Modeling CO₂ Storage in Aquifers with a Fully-Coupled Geochemical EOS Compositional Simulator. Paper SPE-89474 presented at the SPE/DOE 14th Symposium on Improved Oil Recovery, Tulsa, OK, April 17-21, 2004.
- Nicholson, A.J. 2012. Empirical Analysis of Fault Seal Capacity for CO₂ Sequestration, Lower Miocene, Texas Gulf Coast. MS Thesis, University of Texas at Austin, 88 pp.
- Nicot, J.P., Oldenburg, C.M., Bryant, S.L., Hovorka, S.D. 2008. Pressure Perturbation from Geologic Carbon Sequestration: Area-of-Review Boundaries and Borehole Leakage Driving Forces. *Energy Procedia*, **1**: 47–54.
- Onishi, T., Nguyen, M.C., Carey, J.W. et al. 2019. Potential CO₂ and Brine Leakage Through Wellbore Pathways for Geologic CO₂ Sequestration Using the National Risk Assessment Partnership Tools: Application to the Big Sky Regional Partnership. *International Journal of Greenhouse Gas Control*, **81**: 44-65.
- Pedersen, K.S., Fredenslund, A., Christensen, P.L., and Thomassen, P. 1984. Viscosity of Crude Oils. *Chem. Eng. Sci.*, **39** (6) 1011-1016.
- Peng, D.-Y., and Robinson, D.B. 1976. A New Two-Constant Equation of State. *Ind. Eng. Chem. Fundamentals*, **15**: 59-64.
- Prakken, L.B., Griffith, J.M., and Fendick, R.B. Jr. 2012. Water Resources of Allen Parish, U.S. Geological Survey Fact Sheet 2012-3064.
- Reid, R.C., Prausnitz, J.M., and Sherwood, T.K. 1977. *The Properties of Gases and Liquids*, 3rd Edition, McGraw-Hill, New York.
- Renken, R.A. 1998. Ground Water Atlas of the United States: Segment 5 Arkansas, Louisiana, and Mississippi, Hydrologic Investigations Atlas 730-F, U.S. Geological Survey, Reston, Virginia.

- Sakurai, S., Ramakrishnan, T.S., Boyd, A., Mueller, N., and Hovorka, S. 2006. Monitoring Saturation Changes for CO₂ Sequestration; Petrophysical Support for the Frio Brine Pilot Experiment. *Petrophysics*, **47** (6).
- Smoot, C.W. 1988. Louisiana Hydrologic Atlas Map No. 3—Altitude of the Base of Freshwater in Louisiana: U.S. Geological Survey Water-Resources Investigations Report 86-4314, 1 sheet, accessed November 2, 2011, at <http://pubs.usgs.gov/wri/1986/4314/plate-1.pdf>.
- Stevenson, D.A., and McCulloh, R.P. 2001. *Earthquakes in Louisiana*. Louisiana Geological Survey Public Information Series, No. 7.
- Swanson, S.M., Karlsen, A.W., and Valentine, B.J. 2013. Geologic Assessment of Undiscovered Oil and Gas Resources—Oligocene Frio and Anahuac Formations, United States Gulf of Mexico Coastal Plain and State Waters. *USGS Open-File Report 2013-1257*, U.S. Department of the Interior, U.S. Geological Survey, Reston, Virginia.
- Thibeau, S., Nghiem, L., and Ohkuma, H. 2007. A Modeling Study of the Role of Selected Minerals in Enhancing CO₂ Mineralization During CO₂ Aquifer Storage. Paper SPE-109739 presented at the SPE Annual Technical Conference and Exhibition held in Anaheim, CA, November 11-14, 2007.
- Thomas, G.W., and Thurnau, D.H. 1983. Reservoir Simulation Using an Adaptive-Implicit Method. *SPE Journal*, **23** (10): 759-768.
- United States Department of the Interior, U.S. Geological Survey, URL:
<https://groundwaterwatch.usgs.gov/AWLSites.asp>, accessed 2021-3-8.
- United States Geological Survey Advanced National Seismic System Earthquake Catalog Events from Jan 1, 1800, to Jan 14, 2021.
<https://earthquake.usgs.gov/earthquakes/map/?extent=28.62793,-94.79553&extent=33.2295,-88.19824&range=search&search=%7B%22name%22:%22Search%20Results%22,%22params%22:%7B%22starttime%22:%221800-01-01%2000:00:00%22,%22endtime%22:%222021-01-14%2023:59:59%22,%22maxlatitude%22:33.027,%22minlatitude%22:28.837,%22maxlongitude%22:-88.934,%22minlongitude%22:-94.065,%22minmagnitude%22:-10,%22orderby%22:%22time%22%7D%7D>, accessed 2021-01-14.
- United States Geological Survey. 2018. 2018 Long-Term National Seismic Hazard Map, <https://www.usgs.gov/media/images/2018-long-term-national-seismic-hazard-map>, accessed 2021-01-11.
- Warren, A. D. 1957. The Anahuac and Frio Sediments in Louisiana. *Transactions – Gulf Coast Association of Geological Societies Volume VII*. 221-237.
- White, S., Carroll, S., Chu, S., et al. 2020. A Risk-Based Approach to Evaluating the Area of Review and Leakage Risks at CO₂ Storage Sites. *International Journal of Greenhouse Gas Control*, **93**: 102884.

- Whitfield, M.S. Jr. 1975. Geohydrology of the Evangeline and Jasper Aquifers of Southwestern Louisiana: Department of Conservation, Louisiana Geological Survey, and Louisiana Department of Public Works. *Water Resources Bulletin No. 20*, 72 pp.
- Wood, N. 2011. Lockhart Crossing Economically Efficient Reservoir Operations, Denbury Resources Inc. Presented at the 5th Annual Wyoming CO₂ Conference, July 13, 2011.
- Zhang, W., Li, Y., Xu, T., et al. 2009. Long-Term Variations of CO₂ Trapped in Different Mechanisms in Deep Saline Formations: A Case Study of the Songliao Basin, China. *International Journal of Greenhouse Gas Control*, **3** (2) 161-180.
- Zhang, Z.F., White, S.K., and White, M.D. 2015. Delineating the Horizontal Plume Extent and CO₂ Distribution at Geologic Sequestration Sites. *International Journal of Greenhouse Gas Control*, **43**: 141-148.
- Zhu, H., Xu, T., Tian, H., et al. 2019. Understanding of Long-Term CO₂-Brine-Rock Geochemical Reactions Using Numerical Modeling and Natural Analogue Study. *Geofluids*, **2019**, Article ID 1426061.

Appendix A: Near Wells Near the Project Area

Table AOR-12 and Table AOR-13 summarize the legacy wellbores near the project area, as displayed in Figure AOR-23.

Table AOR-12—Legacy Wells Near the Project Area

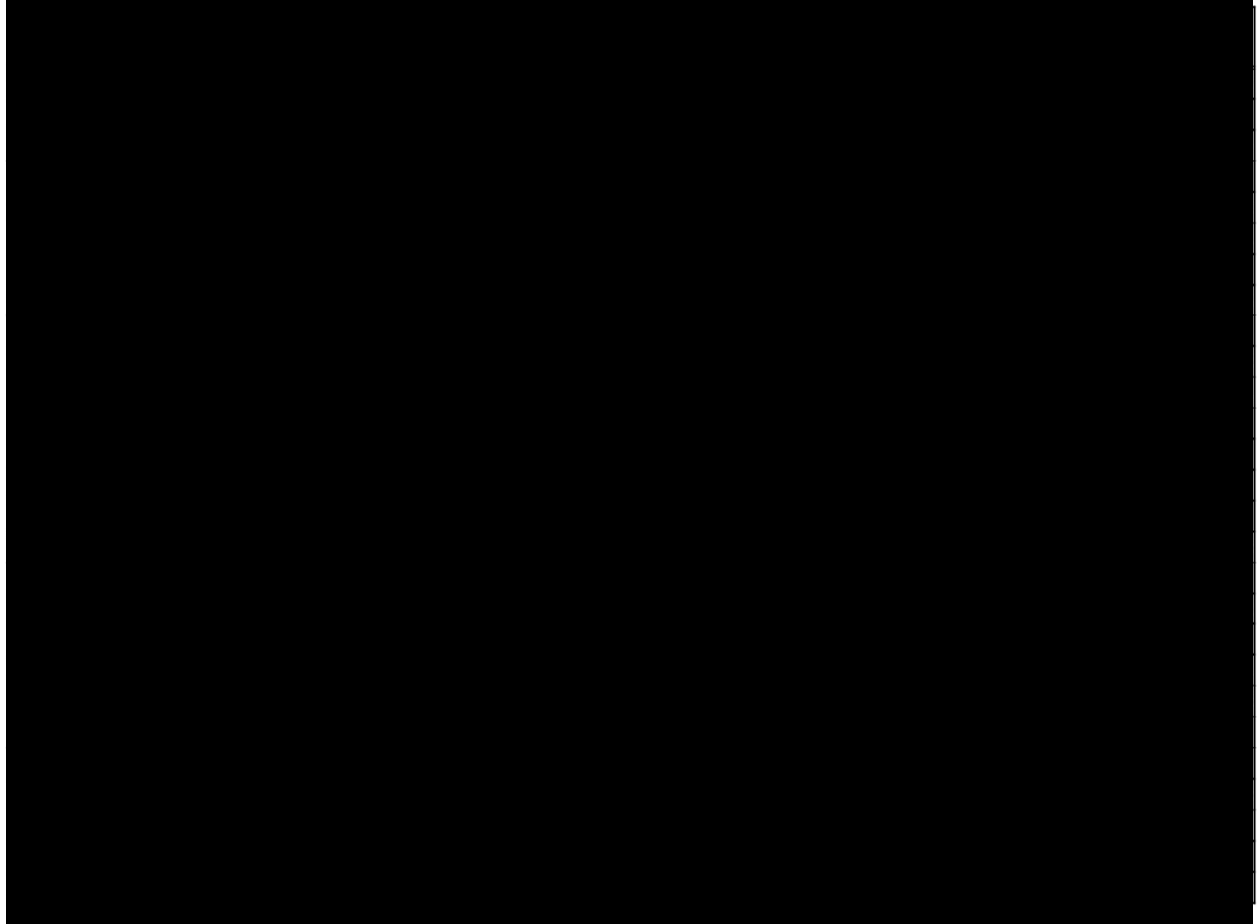
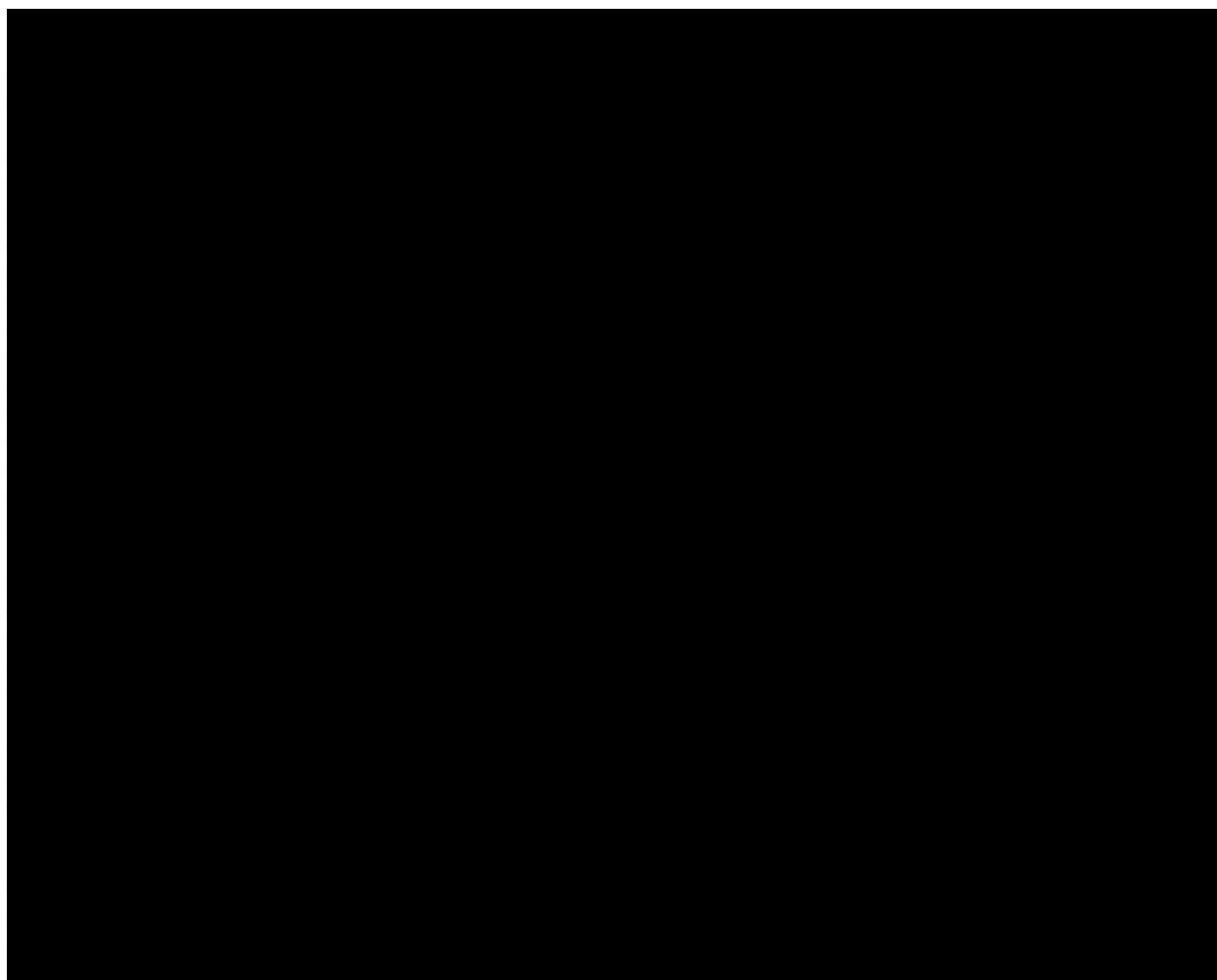


Table AOR-13—Legacy Wells Near the Project Area



Appendix B: Table of Wells

Table AOR-14 summarizes the 59 wells with X-curves used to generate reservoir tops and properties. Well locations are displayed in Figure AOR-24 and Figure AOR-35.

Table AOR-14—List of the 59 Wells with X-Curves

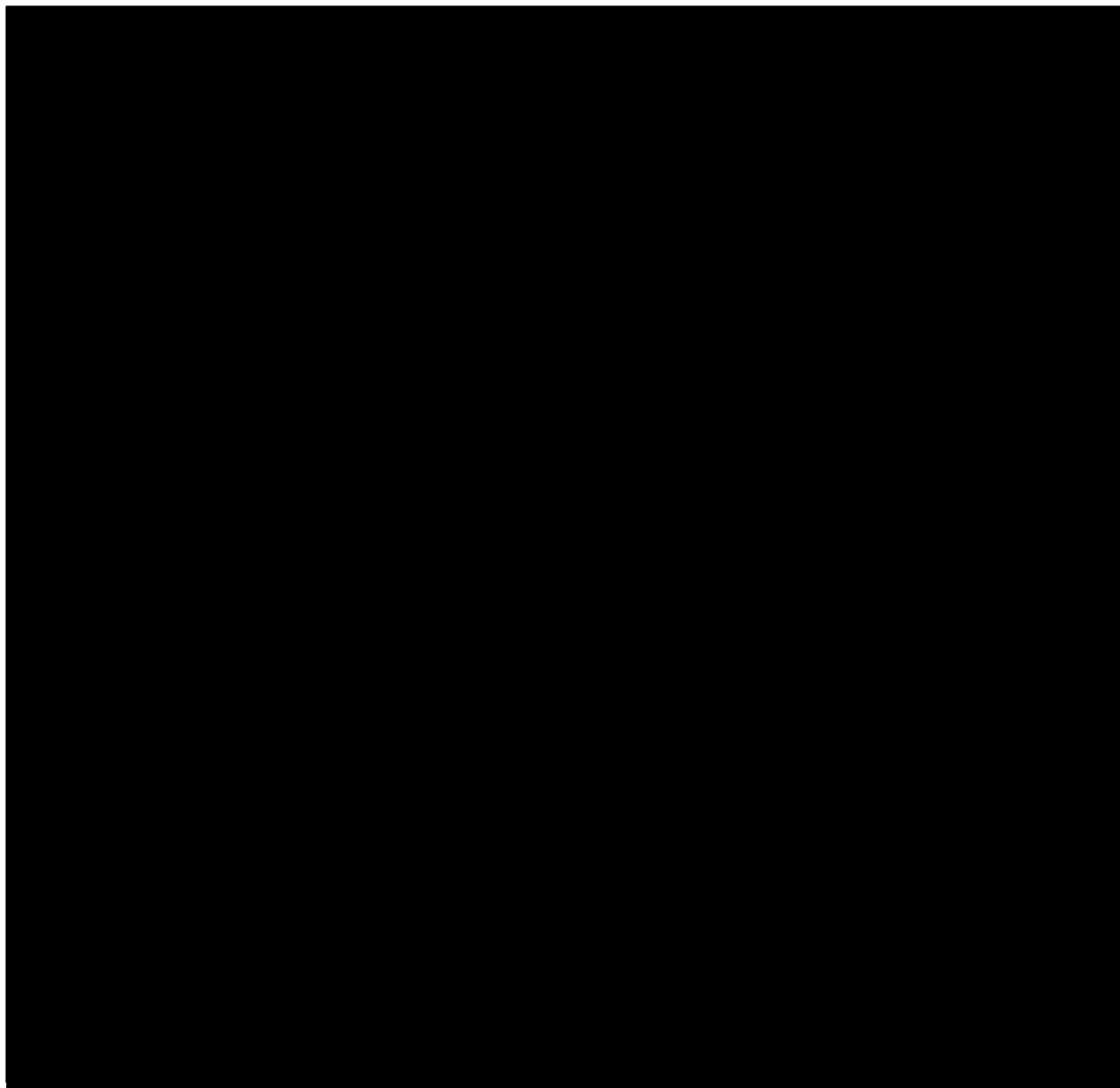


Table AOR-15 lists the [REDACTED] wells used in for seismic well ties as shown in Figure AOR-25.

Table AOR-15—Wells Used for Seismic-Well Ties

Well Name	Well API #
[REDACTED]	[REDACTED]
[REDACTED]	[REDACTED]
[REDACTED]	[REDACTED]
[REDACTED]	[REDACTED]
[REDACTED]	[REDACTED]
[REDACTED]	[REDACTED]
[REDACTED]	[REDACTED]
[REDACTED]	[REDACTED]
[REDACTED]	[REDACTED]
[REDACTED]	[REDACTED]
[REDACTED]	[REDACTED]
[REDACTED]	[REDACTED]
[REDACTED]	[REDACTED]
[REDACTED]	[REDACTED]
[REDACTED]	[REDACTED]
[REDACTED]	[REDACTED]
[REDACTED]	[REDACTED]
[REDACTED]	[REDACTED]
[REDACTED]	[REDACTED]

Appendix C: Site-Specific Data and Procedures

Site-specific data have been collected from the Pelican MLR 004 well. See Figure AOR-1 for its location in the project area.

C.1 Sidewall core sampling and analysis

Sidewall core XRD analysis from the Pelican MLR 004 well was performed by [REDACTED] and is included in the attached report.

C.2 Formation fluid sampling and analysis

Fluid sampling was performed on the Pelican MLR 004 well by [REDACTED] in the cased and perforated hole. [REDACTED]

[REDACTED]

[REDACTED]

[REDACTED]

Table AOR-16—Sampler Run Timing and Conditions for Pelican MLR 004

Run#	Sampler	Sample Cylinder	Sampling Point (ft) MDRT	Start Date @ time (h)	Fire Date @ time (h)	Well Condition	Sample Nature	Sample Volume (cc)
1								
2								
3								
4								
5								
6								

Samples were sent to [REDACTED], where the samples conditions were brought to reservoir temperature and pressure. A sub-sample was flashed to conditions of 60°F and 14.7 psia for analysis of the liquid and gas composition. Methods and results of the analysis are included in the attached reports.

C.3 Well testing and analysis

The Pelican MLR 004 well was perforated and tested in multiple zones for a series of formation integrity tests (FIT) and step-rate tests (SRT), followed by pressure fall-off and leak-off tests (LOT).

The tests were completed starting with the deepest zone.

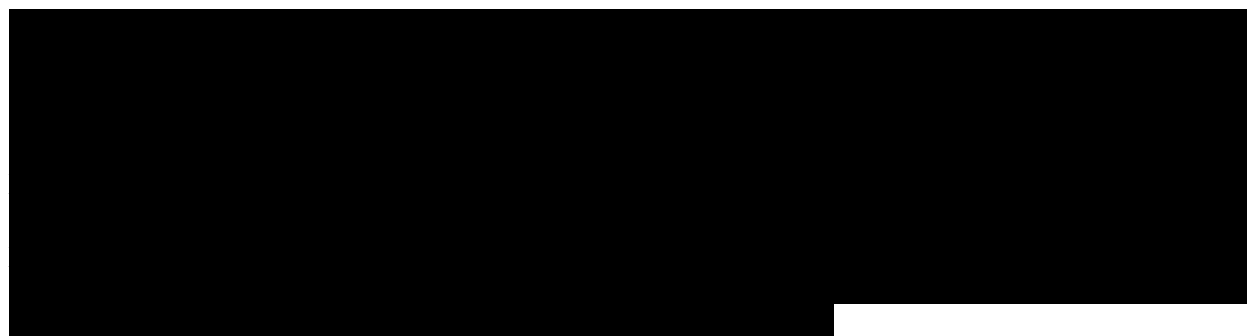


Table AOR-17: Test 1—FIT for Perforated Interval [REDACTED] ft in the [REDACTED] Shale

Time	Pressure (psi)	Gradient (psi/ft)
[REDACTED]	[REDACTED]	[REDACTED]
[REDACTED]	[REDACTED]	[REDACTED]
[REDACTED]	[REDACTED]	[REDACTED]
[REDACTED]	[REDACTED]	[REDACTED]
[REDACTED]	[REDACTED]	[REDACTED]
[REDACTED]	[REDACTED]	[REDACTED]
[REDACTED]	[REDACTED]	[REDACTED]

Note: No fracture was observed in this FIT with a maximum pressure gradient of [REDACTED] psi/ft.

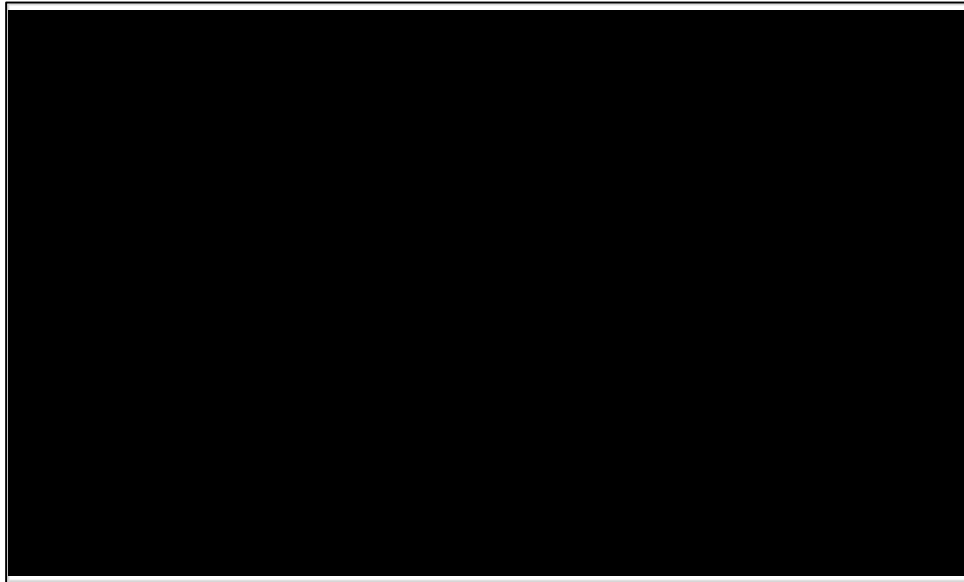


Figure AOR-612—Test 1: FIT for Perforated Interval [REDACTED] ft in the [REDACTED] Shale

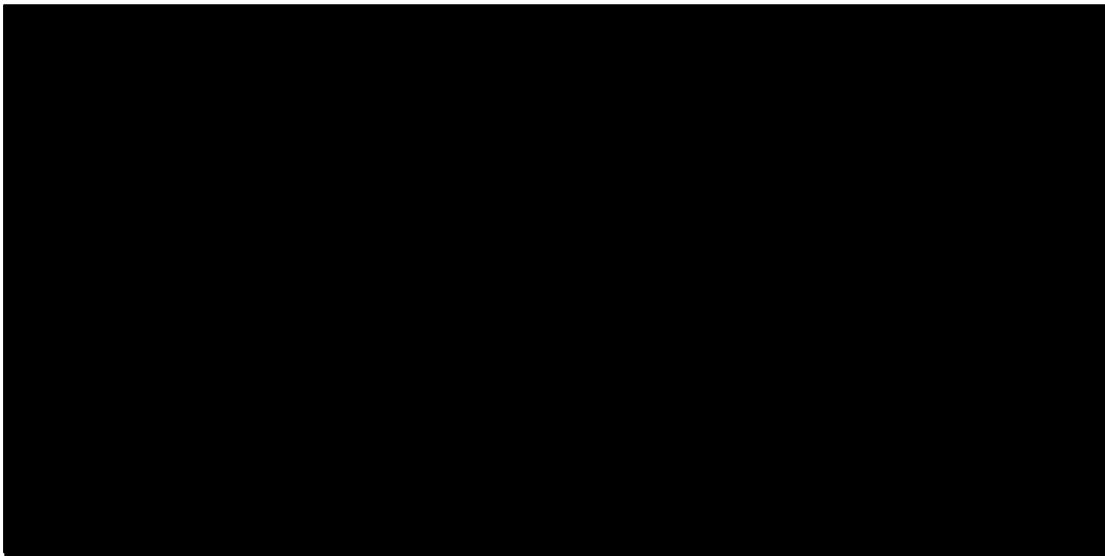


Figure AOR-623—Test 2: Step-rate test at perforations from [REDACTED] ft in the [REDACTED] sand

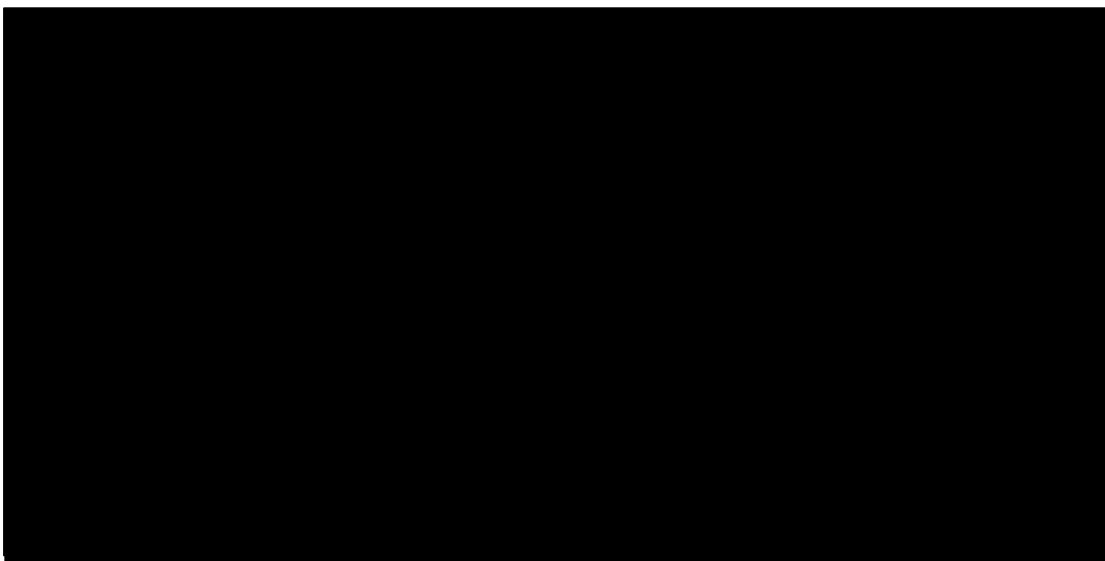


Figure AOR-634—Test 3: Step-rate test at perforations from [REDACTED] ft in the [REDACTED] sand

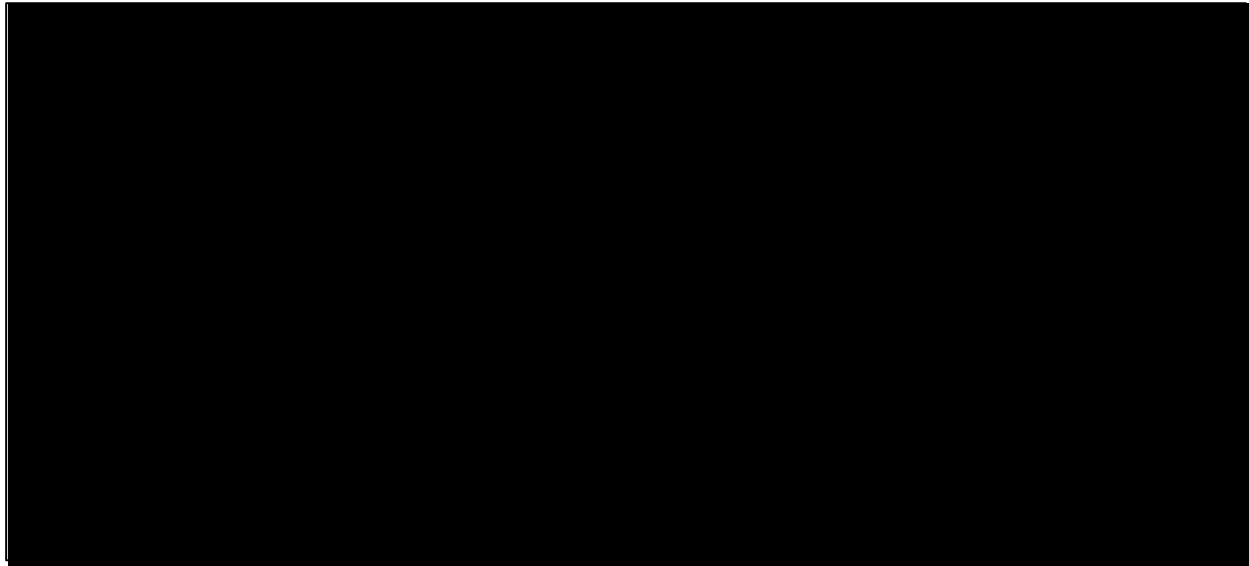


Figure AOR-645—Test 4: Step-rate test at perforations from [REDACTED] ft in the [REDACTED]

Table AOR-18—Test 5: FIT at Perforations from [REDACTED] ft in the Anahuac Shale

bbl	Pressure (psi)	Gradient (psi/ft)
[REDACTED]	[REDACTED]	[REDACTED]
[REDACTED]	[REDACTED]	[REDACTED]
[REDACTED]	[REDACTED]	[REDACTED]
[REDACTED]	[REDACTED]	[REDACTED]
[REDACTED]	[REDACTED]	[REDACTED]

Note: No fracture was observed in this FIT with a maximum pressure gradient of [REDACTED] psi/ft.

Table AOR-19—Test #6: LOT at Perforations from [REDACTED] ft in the [REDACTED] Shale

bbl	Pressure (psi)	Gradient (psi/ft)
[REDACTED]	[REDACTED]	
[REDACTED]	[REDACTED]	[REDACTED]
[REDACTED]	[REDACTED]	
[REDACTED]	[REDACTED]	
[REDACTED]	[REDACTED]	
[REDACTED]	[REDACTED]	

Note: A fracture was created at a gradient of [REDACTED] psi/ft.

Appendix D: Risk-Based AOR

D1. Introduction

[REDACTED]

[REDACTED]

[REDACTED]

[REDACTED]

[REDACTED]

[REDACTED]

[REDACTED]

[REDACTED]

D2. Simulation results

[REDACTED]

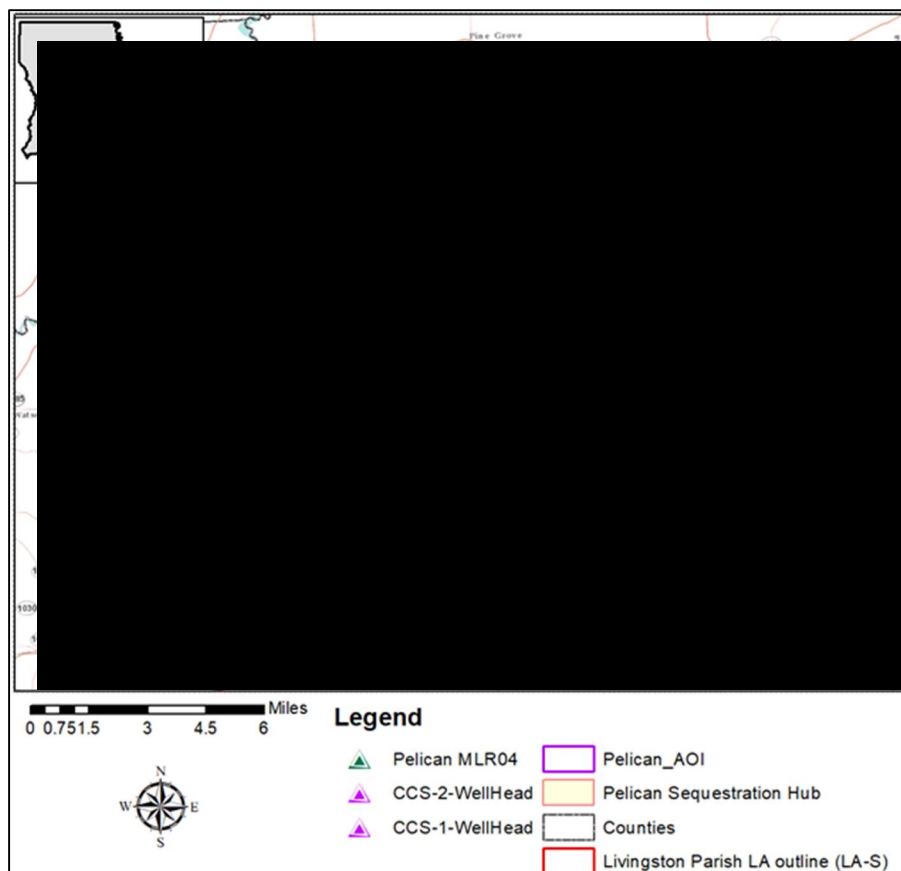


Figure AOR-656—Locations of [REDACTED]

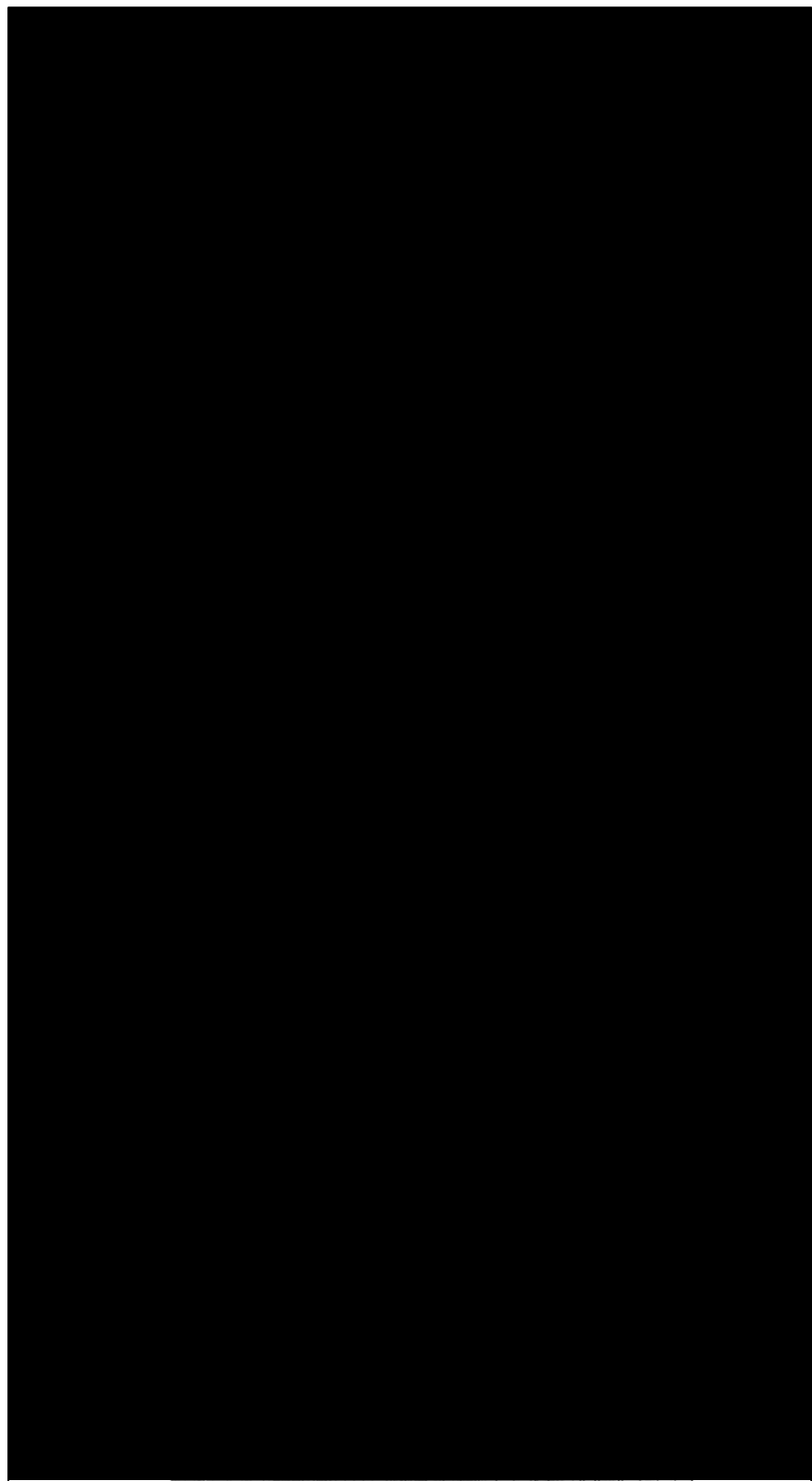


Figure AOR-667—[REDACTED] **wellbore diagram**

Figure AOR-67 shows the model representation of the [REDACTED] well. Radial grids accurately describe the wellbore geometry. The surrounding formation strata were taken from the diagram and from the project geological model. Table AOR-20 lists reservoir properties taken from the project geological model and ranges of sensitivity parameters explored in this study.



Figure AOR-678—Model representation of [REDACTED] well

Table AOR-20—Parameter Ranges Explored in the Sensitivity Study

[REDACTED]	
------------	--

In this case, it is assumed that the casing is completely eroded so that casing horizontal permeability is the same as the outside cement. Shown in the table above are the three parameters in sensitivity study: cement, [REDACTED] permeabilities. One additional parameter is the pore-pressure increase in the [REDACTED]. It is assumed that the [REDACTED] pore-pressure increases linearly from 0 psi at year 0 to DP psi at 15 years. This DP parameter was varied from 0 psi to 500 psi in the various simulation runs.

The model performed sensitivity analyses to develop response surfaces of objective functions, among which were brine flows into [REDACTED]

[REDACTED]

[REDACTED]

[REDACTED]

[REDACTED]

Figure AOR-689—Brine leakage sensitivity study of [REDACTED] well

Plan revision number: 0
Plan revision date: 07/31/23



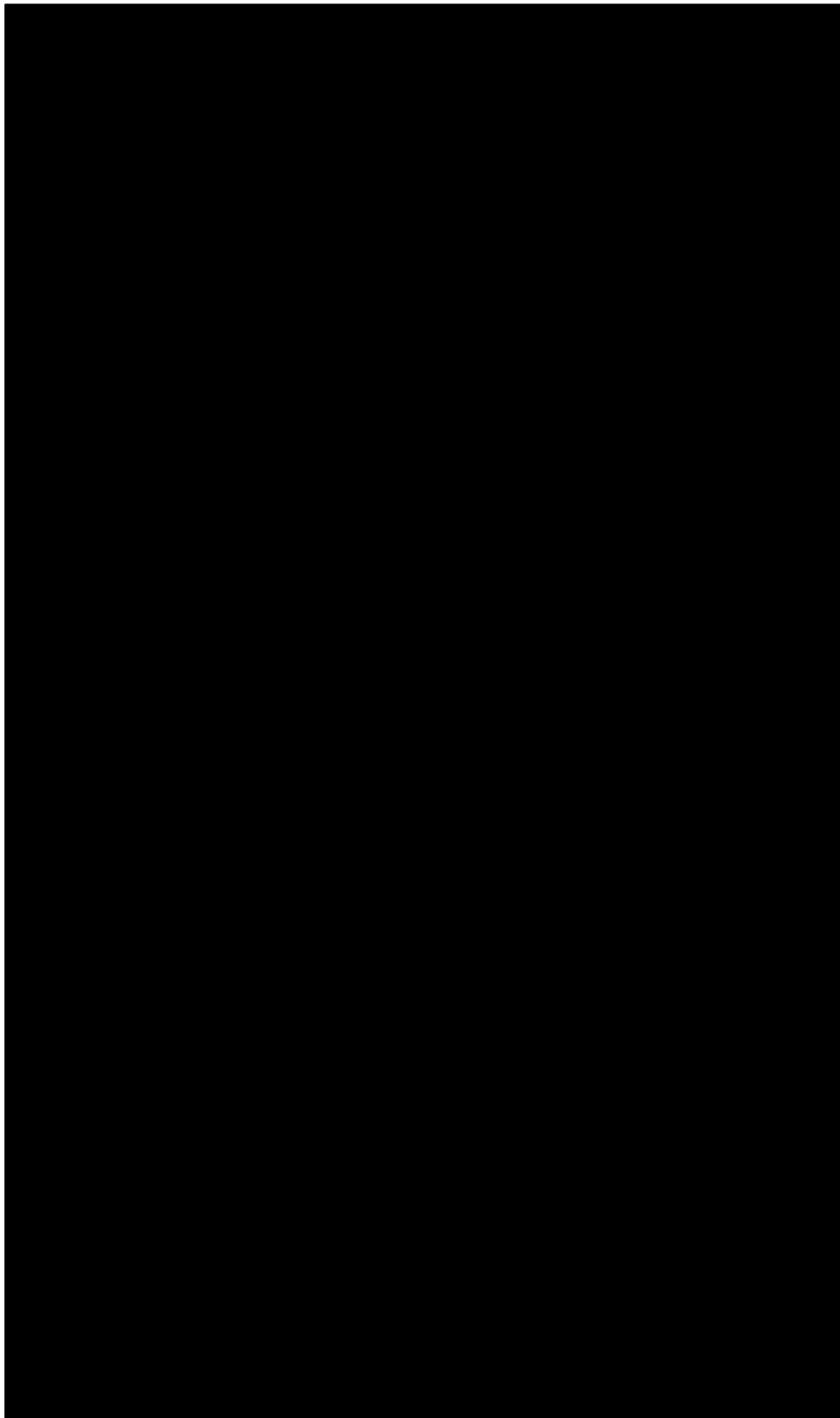


Figure AOR-690—[REDACTED] **wellbore diagram**

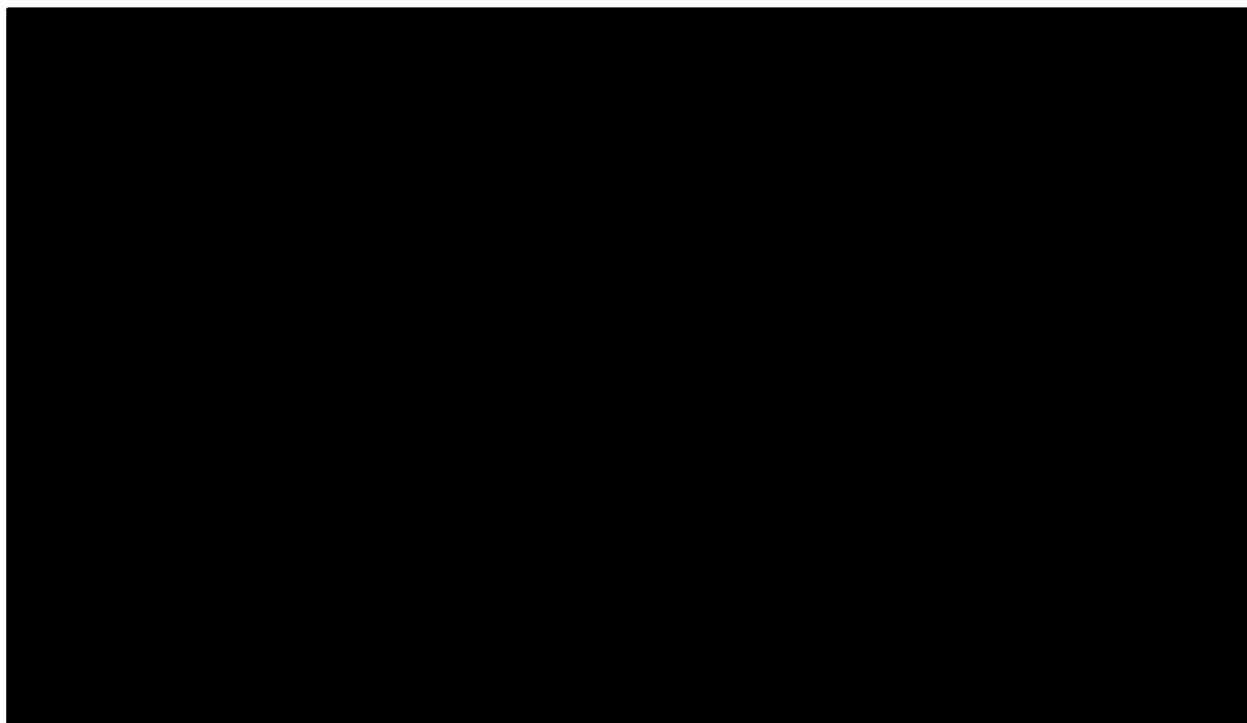


Figure AOR-70—Model representation of the [REDACTED]

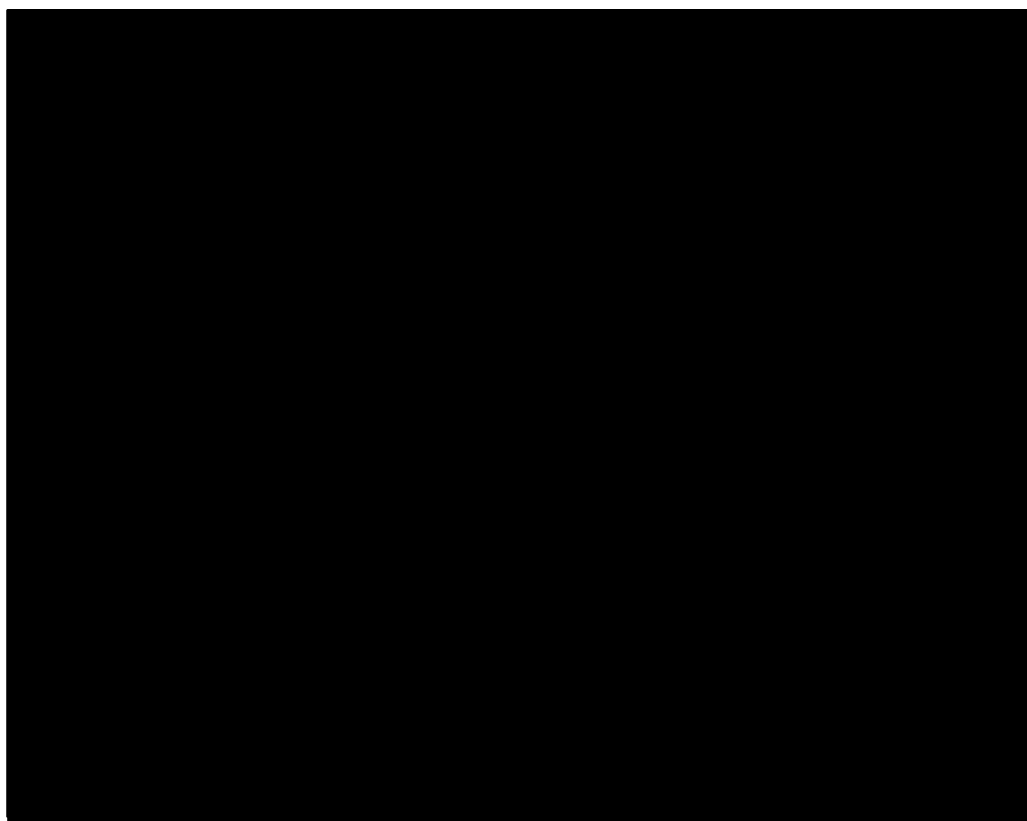


Figure AOR-71—Brine leakage sensitivity study of the [REDACTED]

D3. References

- Appriou, D., Huerta, N.J., Zhang, Z. et al. 2020. Evaluation of Containment and Geomechanical Risks at Integrated Mid-Content Stacked Carbon Storage Hub Sites: Pacific Northwest National Lab., Richland, WA, Report No. PLLN-30047.
- Bacon, D.H., Demirkanli, D I., and White, S.K. 2020. Probabilistic Risk-Based Area of Review (AOR) Determination for a Deep-Saline Carbon Storage Site. *International Journal of Greenhouse Gas Control*, **102**: 103153.
- Burton-Kelly, M.E., Azzolina, N.A., Connorset, K.C. et al. 2021. Risk-Based Area of Review Estimation in Overpressured Reservoirs to Support Injection Well Storage Facility Permit Requirements for CO₂ Storage Projects. *Greenhouse Gases Science and Technology* **11**: (5) 887-906.
- Carey, J.W. 2017. Probability Distributions for Effective Permeability of Potentially Leaking Wells at CO₂ Sequestration Sites. NRAP-TRS-III-021-2017, NRAP Technical Report Series. U.S. Department of Energy, National Energy Technology Laboratory: Morgantown, WV. 28 pp.
- Celia, M.A., Nordbotten, J.M., Court, B. et al. 2011. Field-Scale Application of a Semi-Analytical Model for Estimation of CO₂ and Brine Leakage Along Old Wells. *International Journal of Greenhouse Gas Control*. **5** (2): 257-69.
- Duer, J. "Modeling of CO₂ Leakage from CCS Into Overlying Formations – Quest CCS Monitoring Evaluation," SPE-187100-MS.
- Harp, D.R., Pawar, R., Carey, J.W., and Gable, C.W. 2016. Reduced Order Models of Transient CO₂ and Brine Leakage Along Abandoned Wellbores from Geologic Carbon Sequestration Reservoirs. *International Journal of Greenhouse Gas Control*, **45**: 150-162.
- Hovorka, S., Benson, S.M., Doughty, C. et al. 2006. Measuring Permanence of CO₂ Storage in Saline Formations: The Frio Experiment. *Environmental Geosciences*, **13** (2).
- Juhasz, I. 1986. Assessment of the Distribution of Shale, Porosity and Hydrocarbon Saturation in Shaly Sands. Presented at the 10th European Formation Evaluation Symposium.
- Nordbotten, J.M., Celia, M.A., and Bachu, S. 2004. Analytical Solutions for Leakage Rates Through Abandoned Wells. *Water Resources Research*, **140** (4).
- Oldenburg, C.M., Cihan, A., and Zhou, Q. 2014. Delineating Area of Review in a System With Pre-Injection Relative Overpressure. *Energy Procedia*, **63**: 3715-3722.
- Onishi, T., Nguyen, M.C., Carey, J.W. et al. 2019. Potential CO₂ and Brine Leakage Through Wellbore Pathways for Geologic CO₂ Sequestration Using the National Risk Assessment Partnership Tools: Application to the Big Sky Regional Partnership. *International Journal of Greenhouse Gas Control*, **81**: 44-65.
- Thomas, E.C., and Stieber, S.J. 1975. The Distribution of Shale in Sandstones and its Effect upon Porosity, Paper SPWLA-1975-T presented at the SPWLA 16th Annual Logging Symposium, New Orleans, Louisiana, June 4-7, 1975.

Plan revision number: 0
Plan revision date: 07/31/23

- White, S., Carroll, S., Chu, S., et al. 2020. A Risk-Based Approach to Evaluating the Area of Review and Leakage Risks at CO₂ Storage Sites. *International Journal of Greenhouse Gas Control*, **93**: 102884.
- Yonkofski, C., Tartakovsky, G., Huerta, N., and Wentworth, A. 2019. Risk-Based Monitoring Designs for Detecting CO₂ Leakage Through Abandoned Wellbores: An Application of NRAP's WLAT and DREAM tools. *International Journal of Greenhouse Gas Control*, **91**: 102807.

Appendix E: Historical Seismicity Data

Table AOR-21: Historical Seismicity Data

[illegible]